THE INFLUENCE OF PROCESS PARAMETERS ON THE HOT DEFORMATION BEHAVIOUR OF 2304 LD STAINLESS STEEL

By

OLEARY M. BILL

Supervisor: Prof CW Siyasiya

A dissertation submitted in partial fulfilment of the requirements for the degree of

PhD (METALLURGY)

Department of Materials Science and Metallurgical Engineering

FACULTY OF ENGINEERING, BUILT ENVIRONMENT AND INFORMATION TECHNOLOGY, UNIVERSITY OF PRETORIA, SOUTH AFRICA

June 2018

TITLE	:	THE INFLUENCE OF PROCESS PARAMETERS ON THE HOT DEFORMATION BEHAVIOUR OF 2304 LD STAINLESS STEEL
STUDENT	:	Oleary M. Bill
STUDENT NUMBER:		13416139
DEGREE	:	PhD (METALLURGY)
DEPARTMENT	:	DEPARTMENT OF MATERIALS SCIENCE AND METALLURGICAL ENGINEERING
FACULTY	:	FACULTY OF ENGINEERING, BUILT ENVIRONMENT AND INFORMATION TECHNOLOGY
UNIVERSITY	:	UNIVERSITY OF PRETORIA, SOUTH AFRICA
SUPERVISOR	:	Prof CW Siyasiya

Acknowledgement

Fore mostly, all glory be to the living God for his mercy and the opportunity given to me to complete my studies.

I would like also to express my deepest thanks to my supervisor Prof CW Siyasiya for his genuine, generous, invaluable advice, guidance, assistance, patience and kindness throughout my studies.

I acknowledge with thanks the financial support of Columbus Stainless Steel, AMI through DST and the Department of Materials Science and Metallurgical Engineering of the University of Pretoria. I would like to express my gratitude to my friends within the department Henda, Lwazi, Kweto, Clovis and Steven for their support and valuable encouragement.

Last but not least, I am very thankful to my parents, my wife, Charmaine and my siblings especially Dr Malick Bill.

Contents

List of Figures

ABSTRACT

A series of single compression tests were performed in order to improve the understanding of the influence of processing parameters (temperature, strain and strain rate) on the hot deformation behaviour of 2304 LDSS. The hot compression tests were carried out in the temperature range of 850 – 1050 ^{o}C with strain rates of 0.1, 1, 5, 10 and 15 s^{-1}, and true strain of 0.6. The strain rates were also extended to 30 and 50 s^{-1} and true strain to 0.8 in order to broaden the knowledge base, and to observe if effects such as flow stress steady state can be achieved. Ferrite-to-austenite transformation was observed to take place at higher strain rates with an increase in strain beyond the peak strain; especially at 10 s^{-1}. At lower strain rates of 0.1 and 1 s^{-1}, no increase in the austenite phase fraction was observed.

The increase in austenite phase fraction was observed to take place simultaneously with softening in the flow stress. It was concluded that the phase change was not the cause of the observed flow softening, since flow softening was still observed even in the absence of a phase change (an increase austenite fraction). EBSD results confirmed the flow softening to be due to DRX. The ferrite-to-austenite transformation is suggested to be strain-induced. This strain-induced transformation is based on the fact that the deformation of a dual austenite-ferrite structure results in unequal strain distribution over the two phases and ferrite bearing more strain since it is the softer phase. Upon deformation beyond the peak strain where softening processes are active in both phases; the two phases undergo different softening kinetics due to their difference in SFE. The austenite phase undergoes DRX due to its low SFE and ferrite basically undergoes DRV due to a high SFE (with possibility of CDRX at high strains). This leads to more deformation energy being stored in the ferrite, and hence the driving force for the nearby austenite strain induced boundary migration (SIBM) into the

ferrite in order to minimize the system energy and achieve equilibrium condition. The increase in austenite fraction in turn leads to a shift in the equilibrium phase fractions of ferrite and austenite. Microstructural analysis and processing maps revealed DRV as the operating power dissipation process below the peak strain, ensuring good workability. The flow behaviour in work hardening and dynamic recovery regime was successfully modelled through a physically-based Estrin-Mecking (EM) model. Likewise, the fractional softening regime was also modelled through the Avrami equation. Consequently, an EM model coupled with the Avrami equation was shown to accurately predict the flow behaviour of the 2304 LDSS. A model based on the change in Gibbs free energy resulting in the observed change in phase equilibrium was proposed. The model was developed through incorporating the results from microstructural and EBSD analysis to substantiate the observed dynamic transformation. The model seems to concur with the observation in this study that the ferrite-to-austenite ($\alpha \rightarrow \gamma$) dynamic transformation (DT) taking place was not responsible for the flow softening. Rather it was the DRX in austenite and DRV in ferrite resulting in dislocation density differences which resulted in SIBM that is responsible for the observed $\alpha \rightarrow \gamma$ DT.

No phase fraction change was observed below the peak strain, i.e. up to a strain of 0.3. The significant observation applicable to typical industrial steel processing is whereby the strain per pass is generally below 0.3. Hence, no phase fraction changes would be expected at any stage during a typical industrial finish rolling which would lead to better control of the final microstructures and the subsequent mechanical properties.

Nomenclature

α	ferrite
γ	austenite
LDSS	Lean Duplex Stainless Steel
DIFT	Dynamic Induced Ferrite Transformation
DRV	Dynamic Recovery
DRX	Dynamic Recrystallization
CDRX	Continuous Dynamic Recrystallization
DDRX	Discontinuous Dynamic Recrystallization
SIBM	Strain Induced Boundary Migration
LAGB	Low Angle Grain Boundary
HAGB	High Angle Grain Boundary
EBSD	Electron Backscatter Diffraction
G	Free energy
μ_{Fe}^{α}	Chemical potential of Iron in ferrite
μ_{Fe}^{γ}	Chemical potential of iron in austenite
Θ	Work hardening rate
Q	Activation energy
RD	Rolling Direction
γ_{SF}	Stacking fault energy

Chapter 1

1.1 Background of duplex stainless steels

The need to come up with steels that combine the properties of the single phase austenitic and ferritic stainless steels led to the development of duplex stainless steels, which to-date, have been in existence for close to 80 years. Duplex stainless steels are regarded as steels containing a mixed microstructure of almost equal amounts of austenite and ferrite [1].

Correct amounts of the major alloying elements are crucial in obtaining a stable duplex structure and steel with the desired properties and diverse applicability. The major controlling factors that are necessary for diverse applicability are good mechanical properties such as toughness and good workability characteristics. Currently, duplex stainless steels are widely applied in petroleum refineries, paper manufacturing and marine applications, to name just a few.

To be able to achieve any desired functionality or aspect of the steel, it is fore mostly crucial to understand how that particular steel comes into being. Stainless steels are derived through additions of chromium ranging from 12 to 30 percent which gives these steels their corrosion resistance ability. For this reason a Fe-Cr phase diagram shown in Figure 1.1 is considered first and how the presence of alloying elements can modify this phase diagram and give rise to duplex steel is discussed next.

While chromium especially in substantial amounts, gives steels their “stainless” property, adding more chromium results in the extension of the alpha phase. Presence of other alloying elements however modifies this phase diagram, with the crucial elements being Ni and Mo and N. The presence of Cr, which is a ferrite stabiliser, ensures that the ferrite phase exists over a wider temperature range, and increasing the Cr content in excess amounts of 13 Cr (wt %) in Fe-Cr alloys, for instance will result in a full ferritic structure [2]. On the other hand, adding both Ni and Mn in exceess of 8 and 13 (wt%) respectively, such as in Hadfield steel, results in the bcc-iron α phase being completely eliminated and replaced, down to room temperature, with the γ –phase [2].

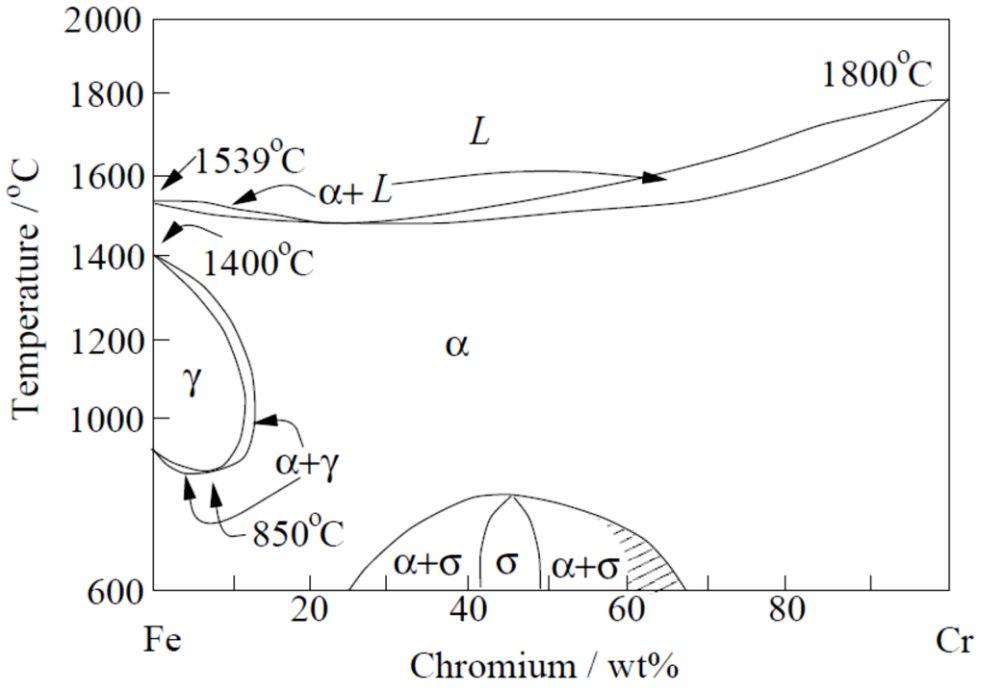

Figure 1.1: The Fe-Cr equilibrium phase diagram **[3]**.

However, the presence of Ni, which is an austenite stabiliser, in an amount of approximately 4 percent [4], is just enough to prevent the steel from becoming fully ferritic and at the same time not fully austenitic. The presence of both austenite and ferrite stabilisers in such a steel gives rise to a duplex structure, *i.e.* the austenite - ferrite ($\alpha + \gamma$) dual phase. Carbon and nitrogen play a crucial role of shifting the gamma loop to higher Cr levels and widening the duplex ($\alpha + \gamma$) phase field [2], as indicated in Figure 1.2.

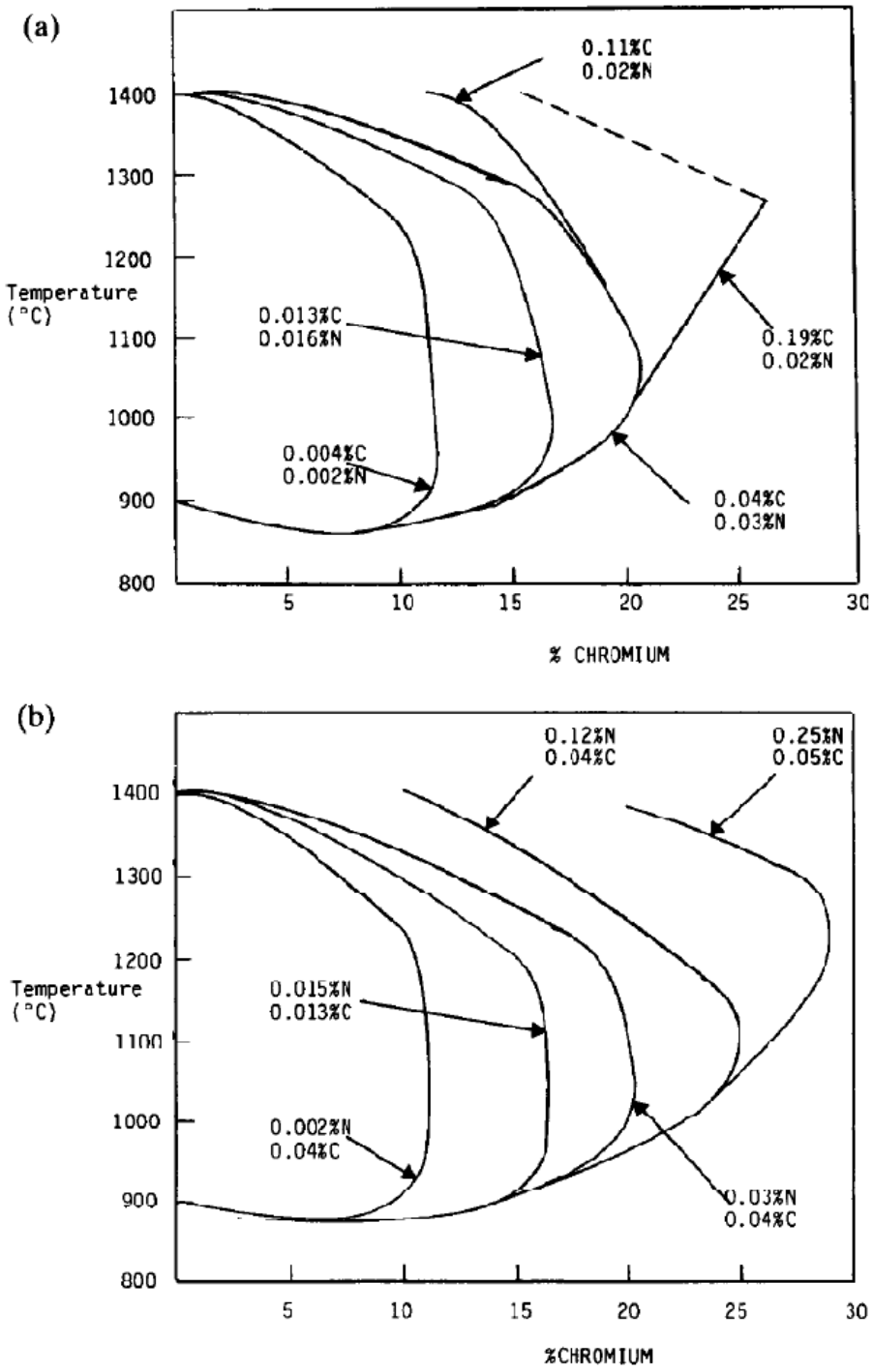

Figure 1.2: Shifting of the phase boundary line (α + γ)/γ in the Fe-Cr system through additions of (a) carbon and (b) nitrogen **[4]**.

Nitrogen which is a strong austenite former is also largely responsible for the balance between the two phases [5]. The addition of the other alloying elements is done on the basis of the effect they have on the (α + γ) phase field and on strengthening of the steel, while ensuring that an almost equal phase ratio is achieved at the end. Though the phase ratio in particular, duplex stainless steel largely varies with temperature, it is also strongly dependent

on the cooling rate. The amount of ferrite that can transform to austenite at high temperatures is lowered when fast cooling rates are used, resulting in ferrite retention [5]. The presence of nitrogen, however, raises the austenite transformation temperature, leading to a higher volume fraction of austenite.

Figure 1.3 below shows why duplex stainless steels are more sought after than austenitic grades in chemical process industries where the risk of stress corrosion cracking (SCC) is high. When compared with austenitic stainless steels with similar chloride pitting and crevice corrosion resistance, the duplex stainless steels have shown to exhibit better SCC resistance [1]. Pitting resistance equivalent number (PREN) is a measure of stainless steel resistance to local pitting in a chloride-containing environment based on their composition. Not shown in the figure but adding to the desirability of duplex stainless steels, is their reduced cost when compared to their counterparts due to the lower alloying elements, especially the Nickel content. [6].

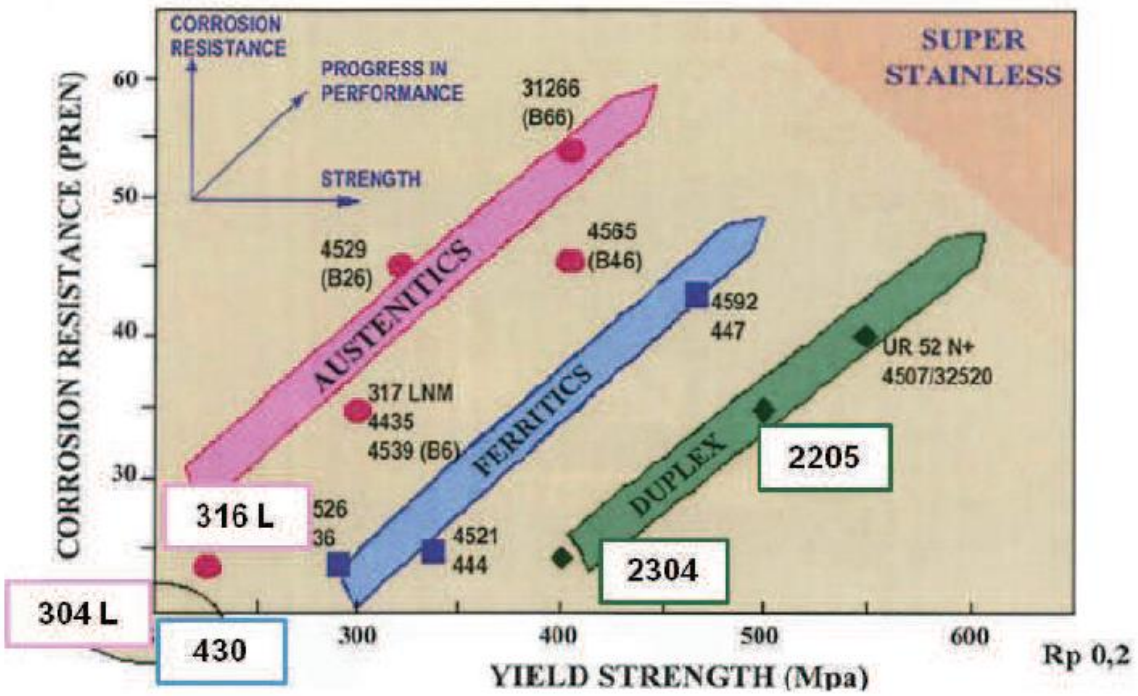

Figure 1.3: Performance of the different stainless steel families in terms of pitting corrosion resistance and yield strength **[7]**.

Despite all the favourable attributes associated with duplex stainless steels, there are still several challenges associated with the processing of these steels compared with single phase

steels. The most critical concern is the poor hot workability of these steels which often results in the appearance of edge slivers and cracks in many instances after a hot working process as shown in Figure 1.4 [7]. Such shortcomings in the mechanical integrity of duplex steels have adverse effects on their applicability and sales, hence it needs to be addressed.

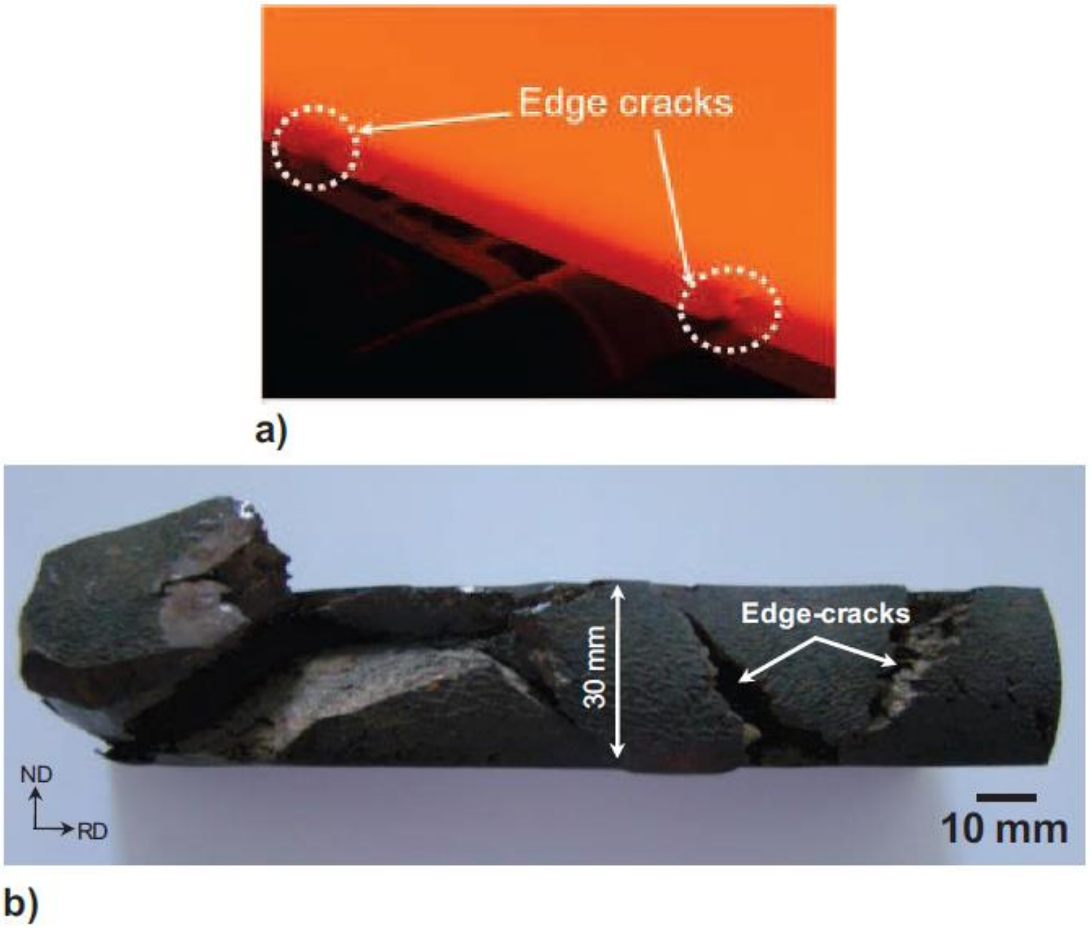

Figure 1.4: Illustration of the poor hot workability of duplex stainless steels; a) occurrence of the first edge-cracks during the roughing mill operations; b) example of edge cracks after the roughing-mill operations **[7]**.

The poor hot workability has been widely attributed to the presence of two phases with different deformation behaviours leading to an inhomogeneous stress and strain distribution during deformation [8], [9], [10], [11]. The issue of inhomogeneous stress and strain distribution is not only peculiar to duplex stainless steels but many other two phase alloy systems as shown in studies by Unkel and many others [12], [13], [14], [15]. The mechanical properties of phases present, their volume fractions, morphology and size determine the nature of the inhomogeneities that will prevail [13]. Another major concern in hot working

duplex stainless steels is ensuring that the desired phase balance and microstructure is achieved during the hot working process.

All the aforementioned factors do also have an effect on the restoration mechanisms during hot rolling and hence have an impact on the mill loads used, which in turn will need to be adjusted accordingly as rolling progresses. One current major concern at one of South Africa's steel producers, is that the phase balance that is used to optimise the rolling processes, is predicted from Thermo-Calc computer software calculations that assume full equilibrium and that optimisation is assumed to remain constant throughout a pass at a given temperature [16]. However, the hot rolling is a non-equilibrium process and, therefore, the phase balance is most likely to change and so do the other factors affecting homogeneity as mentioned above.

Several studies have shown that changes in the volume fraction of the phase ratio α/γ in a given duplex stainless steel can be achieved through altering the temperature [17]. At a given temperature, the volume fraction of the phases present is a function of the chemical composition and in duplex stainless steels, the major alloying elements are chromium, nickel, molybdenum and nitrogen. The roles of each of these alloying elements and other elements also present in duplex stainless steels, will be discussed in the next chapter. Despite several studies on the effects of the second phase on the hot workability of duplex steels and the evolution of the microstructure during hot working of these steels, the studies on phase balance and texture in duplex stainless steel that changes during hot working still remains less studied. Thus, more studies are needed to improve our understanding in the processing of these steels and hence address the associated problems.

1.2 The hot rolling process of steels

Rolling is one of the most widely used processes in metal forming in which the shape, size and microstructure of the metal are changed by passing it through a pair of rolls. The current work will mainly focus on rolling that is carried out above the recrystallization temperature of the metal hence the theme hot rolling (deformation). Typical hot working temperatures are 70 to 80% of the absolute melting temperature of the material [18]. Hot rolling is one of the fundamental steps in steel processing where mechanical properties and quality can be

optimized. This is often achieved through modifying the process parameters according to knowledge gathered from metallurgical and mathematical models of the industrial process [19]. A large amount of research on how each of the rolling parameters, from the geometry of the rolls to roll pass design, influences the gauge variations, shape and metallurgical and mechanical properties of the product and power consumption [20], [21], [22], [23], [24], [25], [26], [27]. Of great significance is the effect of the roll force and roll torque which are the main parameters controlling flatness, geometrical accuracy, yield strength and the hardness of the product, among other attributes [28]. Pioneering work by Sellars and co-workers [29], [30], [31], [32] followed by others [33], [34], [35], [36], [37] has shown that there is indeed microstructural evolution and changes in the mechanical properties of steel during hot rolling which ultimately have an impact on the final product. Of importance to note, is that the build-up of dislocations and subgrain boundaries can result in the material having a stored energy. This stored energy can also be lowered through rearrangement and annihilation of dislocations which also takes place concurrently with deformation. This process is known as recovery. Most importantly, a metallurgical phenomenon that needs to be accounted for is dynamic recrystallization since this will result in microstructural changes taking place during hot rolling [19]. Recrystallization can only take place if there is still enough remaining stored energy after recovery and this will act as the driving force for the process of recrystallization. The two processes are dependent on the deformation and time history of the rolling pass [38] which translates to strain rate, strain and rolling time or inter-pass time [19]. The strain rate plays a fundamental role in influencing the nucleation mechanisms of recrystallized grains [19], [39], [40]. Thus steel microstructures from roughing and finishing mills are bound to be different. Recrystallization has been mostly attributed to the observed decline in the flow stress of some materials during hot rolling. This decline in flow stress should practically be accompanied by adjustments to the mill loads and torque during rolling. Determining this point where mill loads and torque or overall flow behaviour of a material varies with the associated metallurgical phenomena is an area of immense interest and study in order to optimize the hot rolling process. Figure 1.5 shows the schematic diagram of a Steckel mill where process optimization is necessary during rolling in the four-high reversing stands in point B located between two coilers in points A and C.

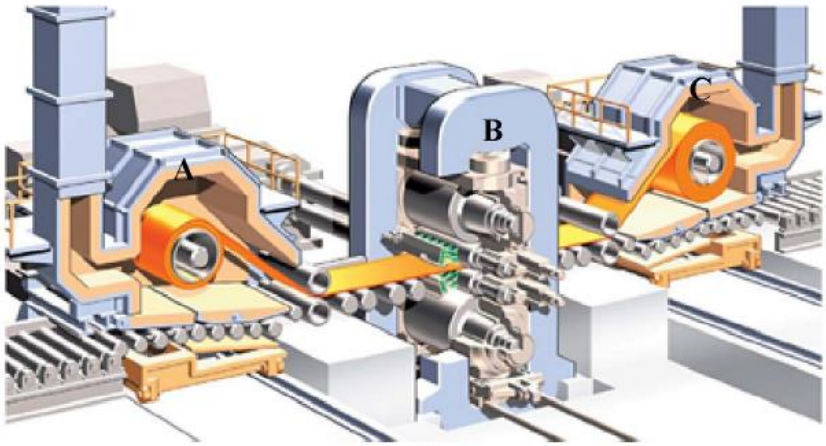

Figure 1.5: Schematic diagram of a Steckel mill **[41]**.

Up to this point, it would appear that there is a knowledge gap and not much is found in literature to date on models correlating for duplex stainless steels the initial phase balance and processing parameters to the final phase balance. Also, up to this point, no work quantifying the amount of phase changes through hot rolling or deformation has been reported in duplex stainless steels. The common assumption is that the austenite and ferrite phase fractions remain constant during hot working. However, in reality the phase fraction is a function of both the chemical composition and the hot working conditions, i.e. strain rate, amount of strain, interpass time and deformation temperature. So far there is a lack of constitutive hot working models that take into account dynamically induced phase transformations in predicting the hot rolling mill loads and the phase balance after hot working.

The finishing rolling process can be carried out through the tandem hot strip finishing mill. Figure 1.6 shows the typical set up of the tandem hot strip finishing mill, where the metal slab is prepared prior to rolling by being passed through the reheating furnace and heated to the desired temperature suitable for intermediate processing and entry into the finishing process. Unlike the previously mentioned reverse finishing mill where the metal strip goes back-and-forth through one stand, in the tandem hot strip finishing mill, the strip is passed through a series of five to seven individual independently driven work rolls, one after the other. A back-up roll of larger diameter supports each work roll (Figure 1.6). The thickness of the strip is successively reduced as it passes through these pairs of individual work rolls. The reduction in thickness is as a result of a high compressive stress from hydraulic cylinders acting in the small region between the work rolls. The desired metallurgical properties are

achieved through cooling the strip with water sprays as it travels towards the coiling mechanism.

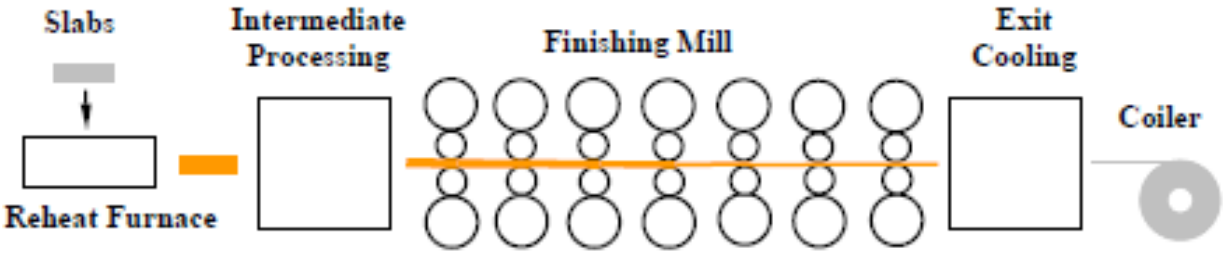

Figure 1.6: Schematic representation of a tandem hot strip finishing mill **[42]**.

The interpass times in the Steckel mill are longer than those in the tandem hot strip mill but the temperature losses between the passes in the steckel are not greater than in the tandem mill due to insulated coil boxes at both ends. Quality problems such as tearing and cracking often result in the Steckel mill due to these temperature losses [43]. These losses are compensated for by holding the coiled strips at elevated temperatures between 950 ^{o}C and 1100 ^{o}C [44]. Interpass times and temperature fluctuations during Steckel rolling are thus some of the important factors to be considered and addressed when optimising the steckel rolling process. However, in the case of stainless steels such as the one under study, temperature loss during Steckel rolling is not an issue due to their low thermal conductivity. The major challenge in the Steckel rolling is that the two ends (front and back) may be affected by longer delay times within the coil box in one direction, with no delay in the reverse direction. The head in one pass is the tail in the subsequent pass, and this makes the interpass times non-uniform. Therefore, the effect of variation in interpass times during Steckel rolling poses a challenge during hot working simulations. In most instances an average interpass time is assumed. Tandem hot strip finishing mills have challenges of their own such as difficulty in obtaining reliable measurements of important variables like strip speed and intermediate stand exit thicknesses due to the challenging hot strip rolling environment [42].

1.3 Problem Statement

The presence of two ductile phases (austenite and ferrite) with different mechanical properties in duplex stainless steels presents complex material behaviour during hot working. Strain localization and defect formation which manifest in form of edge cracks indicate that

there is still need for further work and understanding in the manner in which the imposed deformation is accommodated among the two phases in order to improve the hot working of these steels. The hot working behaviour is further complicated by any changes in the phase balance. This work is thus aimed at understanding the deformation behaviour and phase balance evolution of 2304 LD stainless steels in the Steckel rolling mill and to optimize the finish rolling process. The aspects of the finishing rolling process covered in the current study, together with scope of the thesis are presented in Figure 1.6.

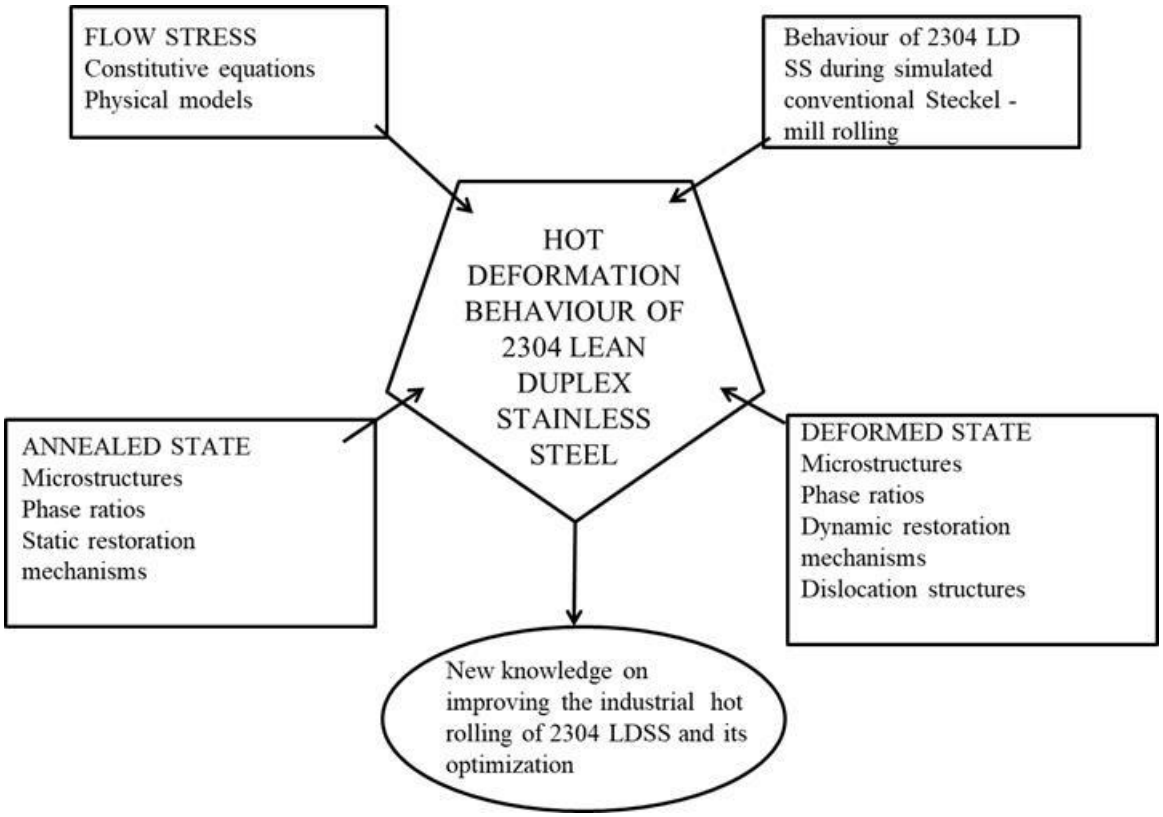

Figure 1.7: Flowchart illustration of the scope of this study.

1.4 Objectives

- Investigate the effect of the processing parameters on the hot working behaviour of 2304 LD stainless steel,
- Develop a model for the prediction of the hot working behaviour of this steel for the Steckel Mill,
- Determine the mechanisms at play during hot working and their effects on phase balance and microstructures,

- Evaluate the optimum processing window and optimise the in-plant hot working process for this steel through laboratory thermomechanical simulation.

The deformation of steels in general and role of dislocations in deformation are implicitly presented in Chapter 2. Chapter 3 presents a review on the restoration mechanisms related to plastic deformation and their role in overall behaviour of steels with different stacking fault energy properties. These present a foresight into the possible metallurgical mechanisms that will impact the phase fraction and microstructure evolution processes. Plastic deformation in many cases provides the extra driving force through stored energy for either phase transformation or microstructure evolution to take place. Relevant constitutive models are reviewed in Chapter 4. In Chapter 5, the experimental design is presented. This chapter encompasses all the experiments carried out which to a greater extend involved deformation in either the Bȁhr dilatometer or Gleeble, and various characterization techniques employed thereafter. The experimental findings from the study are presented in Chapter 6; plastic deformation was found to be associated with a change in phase fraction and morphology, and flow curves exhibited substantial dynamic softening. The findings from the present study are discussed in Chapter 7. The suggested model according to the findings from the study is also presented in this chapter. Finally, the conclusions drawn from the study and its contributions to the current knowledge base are stated in Chapter 8.

Chapter 2

2.1 Introduction

In steelmaking, a number of processes are employed in order to achieve the desired final product. The mechanical properties are modified through control of the microstructure which can be done by a combination or one of the following:

- Modifying the alloy composition which in turn will modify the equilibrium and non-equilibrium second phases present in a material, including their volume fractions, shapes and sizes and distribution.

- Heat treatment can also be used to modify the mechanical properties through altering the defect structure, grain size, and also the other aspects already mentioned under alloy composition.

- Plastic deformation which can be carried out through either a hot or cold route, also modifies the microstructure of the steel and hence the mechanical strength. Hot or warm rolling is carried in the two-phase region which is crucial to this study, and in application is mostly reviewed in low carbon steels. The region of interest lies between the A_1 and the A_3 temperatures, where austenite co-exists in equilibrium with ferrite at a given temperature as shown in the Fe-C phase diagram below.

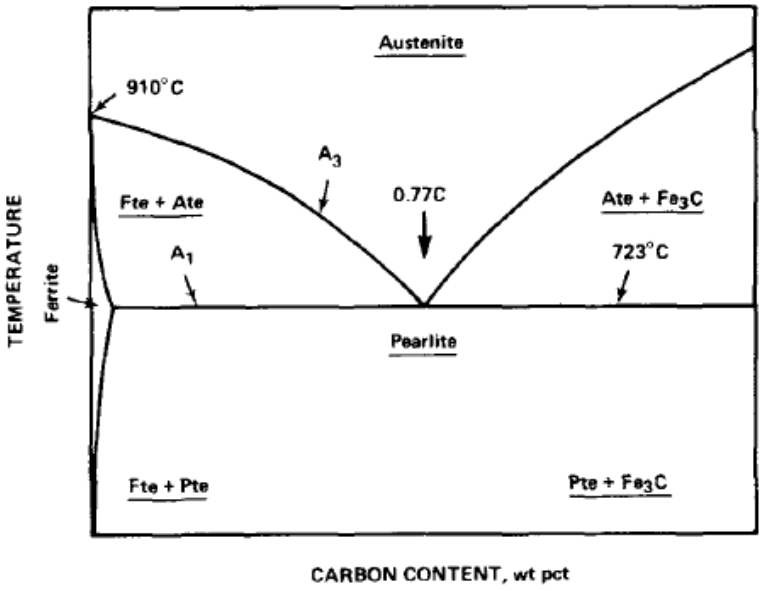

Figure 2.1: Fe-C phase diagram showing the two phase α + γ region.

In the region between the A_1 and A_3 temperatures a certain amount of austenite exists in equilibrium with a certain amount of ferrite at a given temperature. In this two phase ($\alpha + \gamma$) region, the chemical potentials of Fe and Carbon in the ferrite and austenite must be equal across the interface, in order for equilibrium to be sustained. In such a scenario; the chemical potentials are as follows:

$$\mu_{Fe}^{\alpha} = \mu_{Fe}^{\gamma} \text{ and } \mu_{C}^{\alpha} = \mu_{C}^{\gamma} \qquad [2\text{-}1]$$

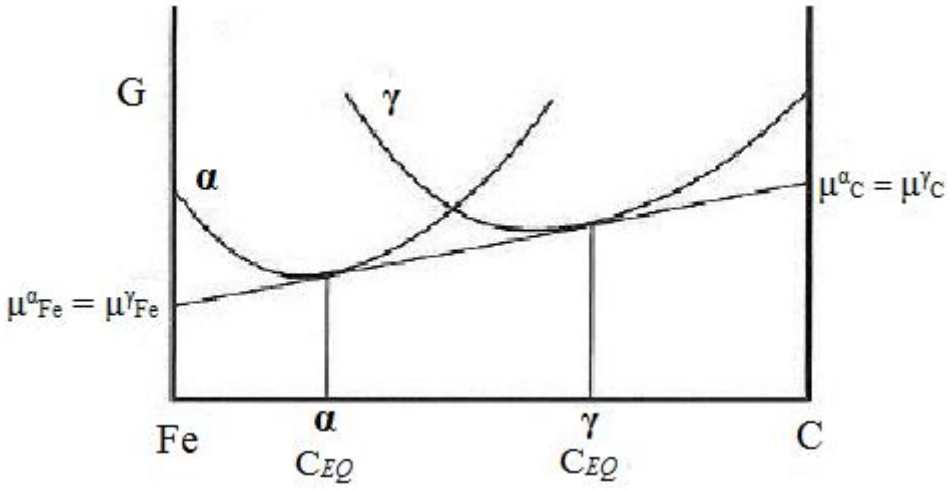

Figure 2.2: A two phase system of (α + γ) at full equilibrium.

Under the equilibrium condition with a Gibbs free energy curve shown in Figure 2.2, the phase fraction of each of the two phases is a function of both temperature and composition. The amount of either of the phases is determined using the lever rule, given that the system is at equilibrium. The lever rule is applied as shown in Figure 2.3.

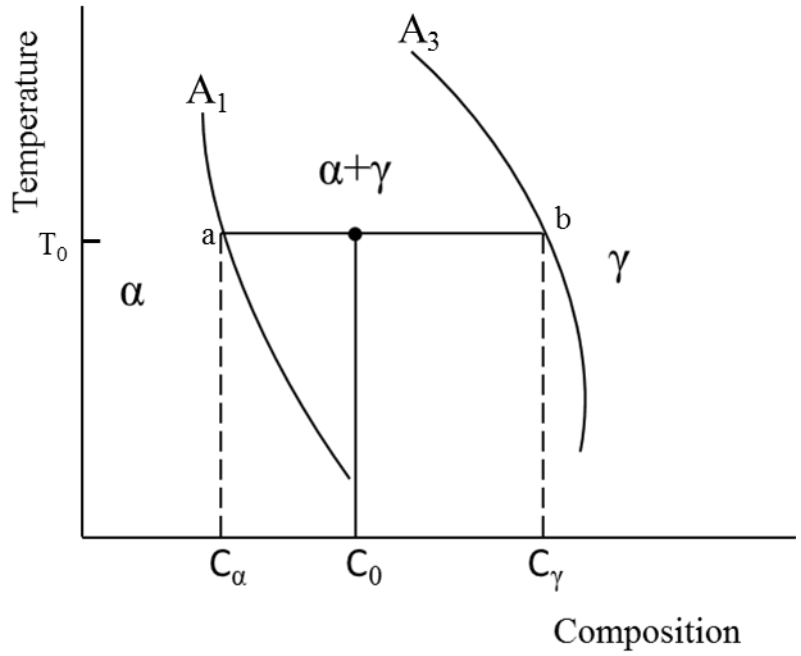

Figure 2.3: Application of the lever rule in a two-phase region to determine phase fractions.

Figure 2.3, shows a section of a Fe-C phase diagram illustrating how the lever rule is used to determine the phase fraction of each phase at a given temperature T_0 and composition C_0 in the two-phase region. The tie-line ab intersects with the A_1 and A_3 lines at a and b and these points correspond to the composition values of C_α and C_γ, respectively.

The phase fraction of ferrite:

$$V_\alpha = \frac{C_\gamma - C_0}{C_\gamma - C_\alpha} \qquad [2\text{-}2]$$

and austenite:

$$V_\gamma = \frac{C_0 - C_\alpha}{C_\gamma - C_\alpha}. \qquad [2\text{-}3]$$

2.2 Plastic deformation in the two-phase region

The existence of two phases with different structures means that deformations in the two phases are likely to be different. Deformation takes place through slip on the close packed planes in close packed directions and these differ in austenite and ferrite. It is worthwhile to consider deformation behaviour of the two individual phases before considering their behaviour in combination with each other.

2.2.1 Stacking Fault

Stacking faults are one of the most important planar defects found in metallic materials that give rise to the major difference in deformation behaviour of austenite and ferrite phases. A stacking fault is easier to consider in face centred cubic (fcc) structure as a disturbance in the ABC stacking sequence of the close packed {111} layers. The energy difference arising between a perfect ABC stacking sequence and an imperfect or disturbed stacking sequence is termed the stacking fault energy (SFE). The interaction between stacking fault energy and dislocations forms the fundamental basis of plastic deformation and hence other processes important to rolling. Plastic deformation in austenitic steels can occur through different mechanisms and the most important deciding factor in the operating mechanism is the stacking fault energy (SFE). The SFE of austenitic steels has been reported to vary typically in the range of 14 – 28 mJ/m^2 [45], [46], [47], though this can vary due to alloying, as will be shown shortly.

Stacking fault energy plays a fundamental role in determining the rate at which dislocations are annihilated. In high SFE microstructures, dislocation movement through glide, climb and cross slip takes place with relative ease since the recombination of partials that is required before climb or cross slip that takes place easily because partials exist relatively close to each other. Dislocation climb with the assistance of vacancies and cross slip from the high SFE, are rate controlling for recovery, making recovery the predominant process in high SFE materials.

Recovery is thus detrimental to the accumulation of dislocations or deformation stored energy and hence inhibits grain boundary migration and DRX [48]. The extent of recovery at low stresses increases with temperature as processes such as dislocation climb and cross slip become more pronounced at elevated temperatures [8], [49]. Thus, high SFE materials such as the BCC ferrite are characterized by low deformation resistance and low activation energy Q values for recovery due to the ease with which dislocation annihilation and rearrangement takes place through recovery [8]. On the other hand, the partial dislocations in low SFE materials are further apart, which makes dislocation recombination difficult and hence deterring processes such as cross slip and the ability of the dislocation to glide onto the intersecting slip plane.

The process of recovery is significantly inhibited in low SFE materials such as austenite [50], causing an increase in the dislocation density and strain accumulation due to the presence of planar dislocation structures, even at elevated temperatures [48]. This strain accumulation allows sufficient driving force for DRX to be attained and to be triggered once the dislocation density reaches a critical value [51], [52], [53], [54]. Since dislocation cross slip, annihilation and rearrangement are shifted to higher temperatures in low SFE materials, such materials are characterized by higher activation energy Q values for recrystallization than those perceived for recovery in high SFE materials [8].

The effect of SFE on the respective deformation behaviours of austenite and ferrite is strong in each of these two phases in the absence of the other phase, while in combination in a dual phase microstructure, the effect of the adjacent phase is important [55]. The two phases also have different strengths at hot working temperatures which ultimately affect the strain distribution between the two constituents in duplex steel. Generally, the softer phase is perceived to accommodate most of the strain than the harder phase, as it is easier to plastically deform [55], [56].

Another important factor is the effect of temperature on the movement of dislocations. Different obstacles affect the movement of dislocations at low and high temperatures, most of which at high temperatures become trivial due to thermal activation. At low temperatures both short range and long range order obstacles are effective in hindering the movement of dislocations as they can only move through glide mechanism at this point. Thus, movement of dislocations is often hindered by various obstacles, such as interactions with other mobile and immobile dislocations and with solute atoms and precipitates. Interactions with grain boundaries also hinder the dislocation movement. However, as the dislocations move with different overall speeds within the material, an average velocity $\bar{v}$ is used to describe the movement and this is dependent on the applied strain rate. The relationship between the average velocity $\bar{v}$ and the strain rate $\dot{\varepsilon}$ is given as:

$$\dot{\varepsilon} = \rho_m b \bar{v} \qquad [2\text{-}4]$$

where ρ_m is the density of mobile dislocations and b is the magnitude of the Burgers vector.

Apart from hard precipitates which pose an obvious impediment to the movement of dislocations resulting in an increase in flow stress, coherent and less hard precipitates which in most cases are often easily cut by moving dislocations, can also impede the movement of mobile dislocations if their density is high enough.

At higher temperatures such as those at which high temperature rolling is carried out glide ceases to be the only mechanism by which dislocations can move. Apart from only gliding and limited to a single plane as in the case of low temperatures, at high temperatures, dislocations are also able to climb on to other planes due to the presence of many vacancies. By so-doing, dislocations can overcome obstacles more than at lower temperatures where less vacancies are present. The ability of dislocations to be able to climb is envisaged to be facilitated by vacancies which are created at high temperatures. Thus, the climb rate of dislocations is dependent on the vacancy flow to and from dislocations [57]. Though both glide and climb of dislocations are involved in the migration of sub-boundaries which ultimately impacts on processes such recovery and recrystallization, it is the process with the lower rate of movement that becomes the rate limiting process [58]. Thus, the migration of sub-boundaries is dependent on the climb velocity of dislocations and, according to Hirth [57] in pure metals is given by:

$$v_0 = \frac{D_{SD} b^2 2\pi}{kT ln\left(\frac{R_d}{b}\right)} \sigma \qquad [2\text{-}5]$$

where D_{SD} is the self-diffusion coefficient, b is the Burger's vector, R_d is the cut-off radius of the stress-field of a dislocation, i.e. the distance between dislocations which is estimated to be ($\sim$ 100b), σ is the applied stress, with k and T having their usual meanings. In reality, metals are hardly pure and thus the modification of the above equation by Sandstrom and Lagneborg [58], taking into account the effects of substitutional atoms, is more applicable:

$$v_0 = \frac{D_{SD} b^2 2\pi}{kT} \cdot \frac{\sigma}{ln\left(\frac{R_d}{b}\right) + \left(\left(\frac{D_V^{III}}{D_V^{II}}\right) ln\left(\frac{r_1}{r_0}\right)\right)} \qquad [2\text{-}6]$$

where D_V^{II} and D_V^{III} are the diffusion coefficients of vacancies in the region of the dislocation core as affected by the solvent and solute, respectively, r_0 is the radius of the dislocation core ($\sim b$), and r_1 is the radius in the vicinity of the dislocation core ($\sim 2b$). According to Sandstrom and Lagneborg [58], the following equations can be assumed for D_V^{II} and D_V^{III};

$$D_V^{III} = D_{SD}^{A} C_V v_a \quad [2\text{-}7]$$

and

$$\frac{1}{D_V^{II}} = \frac{1}{D_V^{III}} + \frac{1}{D_{SD}^{B} C_V v_a exp\left(-\frac{\Delta E_{ie}}{kT}\right)} \quad [2\text{-}8]$$

where C_V is the concentration of vacancies while the activation energy for formation of vacancies in FCC iron with the enthalpy value ΔH = 284 kJ/mol. The above scenario of climb is only prevalent for edge dislocations at high temperatures and not for screw dislocations, which cannot climb due to lack of the extra half plane of atoms. However, screw dislocations can cross-slip onto other planes in order to overcome obstacles on their slip planes. These two types of dislocations will be discussed further below.

2.2.2 Edge and Screw Dislocations

For an edge dislocation, climb of only one slip plane is possible per vacancy (or a set of vacancies) at a time due to the Burgers vector being perpendicular to the dislocation. On the other hand, in a screw dislocation, the Burgers vector and the dislocation are parallel, thus making any valid slip plane containing the dislocation a possible alternative slip plane. The orientation of the Burgers vector and the slip plane of the dislocation, therefore, fundamentally distinguish the way the dislocation can move. Whereas the screw dislocation can move by slip or glide in any valid direction perpendicular to the line itself, an edge dislocation can only glide in its single slip plane [59], [60]. However, through climb an edge dislocation is also able to move in a direction perpendicular to its slip plane.

As the material is further strained, the interaction of dislocations as they continue to multiply and their interaction is increased, is an important issue in plastic deformation. As such, the ease with which the gliding dislocations overcome the barriers provided by this forest of dislocations, will determine whether the material will work harden or not, as each dislocation moves past other dislocations intersecting its slip plane. Thus, the intersection of dislocations will in part determine whether slip will be easy or difficult [59].

A sessile jog formed in a screw dislocation can however, result in the movement of dislocations being significantly impeded, leading to work hardening. At higher temperatures, vacancies diffuse more rapidly and climb of jogs contributes to dynamic recovery when work

hardening and the recovery process are in equilibrium. However, alloying atoms can also affect dislocation climb and related processes through solute drag on the dislocations [61].

2.2.4 Cross slip of dislocations

Apart from climb, dislocations can cross slip to another valid slip plane in the same direction to avoid other dislocations in their slip plane or obstacles such as precipitates, especially at intermediate temperatures [62]. Cross slip is prominent in metals with high SFE, for the reason that will be elaborated shortly and only screw dislocations can cross slip as their Burgers vector lie parallel to the dislocation line. Though cross slip is thermally activated, it does not however require the diffusion of vacancies [3].

When a dislocation dissociates into two partial dislocations, an equilibrium distance d_{SF} exists where the repelling forces between the two partial dislocations and the attracting force to keep the stacking fault area as small as possible, are in balance. To be able to cross slip the two partial dislocations need to constrict first and energy is required to overcome the repulsive force between the two partial dislocations. The energy required is dependent on the equilibrium distance d_{SF}. The equilibrium distance however varies with the SFE through the relationship:

$$d_{SF} = \frac{G_M b^2}{4\pi\gamma_{SF}} \qquad [2\text{-}9]$$

where G_M is the shear modulus of the material, b is the Burgers vector of the partial dislocations and γ_{SF} is the stacking fault energy. From the above equation, an inverse relationship exists between the separation distance between the two partials and the stacking fault energy:

$$d_{SF} = f\left(\frac{1}{\gamma_{SF}}\right) \qquad [2\text{-}10]$$

Thus, the higher the SFE the narrower the separation between the two partials and the lower the energy required to constrict the dislocations, hence the prominence of cross slip in materials with high SFE. In such materials, recovery of the dislocation structures into sub-grains during annealing will take place before recrystallization. In materials with low SFE, the opposite is true. Thus, recrystallization will take place without any prior recovery [63].

As pointed out earlier, the SFE is strongly modified by large concentrations of alloying elements. Hence, the alloying elements can alter the ability to cross-slip and ultimately the recovery kinetics [3].

2.2.5 Law of mixture in an austenite-ferrite dual phase material

Massive second phases tend to plastically deform different from the matrix material. In the case of duplex steels, strain partitioning has been widely reported to take place in the early stages of plastic deformation [64], [65], [66], [51], [67], [68].

Plastic strain is initially accommodated by the softer phase (ferrite) and transferred to the harder one (austenite) when the strain level is increased [69], [70]. The strain distribution between austenite and ferrite in duplex stainless steel (DSS) is given by the law of mixtures as [71]:

$$\varepsilon_{DSS} = F\varepsilon_F + A\varepsilon_A \qquad [2.11]$$

where ε_{DSS}, ε_F and ε_A denote the strain of DSS, the strain accommodated by ferrite, and the strain accommodated by austenite, respectively; F and A are the contribution effects of ferrite and austenite, respectively.

Equation [2.11] presents a classical law of mixtures where the properties of the mixture are expressed in terms of the bulk properties and the relative amounts of the constituents in the two-phase material. The fact that the two phases have different mechanical properties implies that the phases will react differently to the applied stress [72]. The difference in response to applied stress depends on strength difference between the phases, their volume fractions and morphology of the phases [72], in addition to the flow properties of the constituent phases [73]. For this reason, Cho and Gurland [73] indicated that the yield strength, like strain, which is generally expressed according to the law of mixtures in equation [2.12], needs to be modified.

$$\sigma_y = \sigma_0^{\alpha} V_{\alpha} + \sigma_0^{\gamma} V_{\gamma} \qquad [2.12]$$

where σ_{α}^{0} and σ_{γ}^{0} are the yield strengths of the constituents as measured in bulk, and $V_{\alpha}$and V_{γ} are their volume fractions.

Equation [2.12] is limited by the fact that it is only valid for cases where there is an equal amount of strain in both phases, which is often not the case with most of the two-phase

alloys. Many factors are at play, hence the properties and stress states of the in-situ phases are strongly dependent on the microstructure, and this entails the size, shape, orientation and connectivity and the interaction between the phases [73].

Among the comprehensive reviews of the deformation behaviour or plasticity of two phase alloys, Ankem and Margolin [13] proposed an alteration to the linear law of mixtures for the purpose of accounting for microstructural and interaction effects. Their resultant yield strength relation took the following form:

$$\sigma_y = \sigma_{y\alpha}^{c} V_\alpha + \sigma_{y\gamma}^{c} V_\gamma + I_{\alpha\gamma}^{y} \qquad [2.13]$$

where $\sigma_{y\alpha}^{c}$ and $\sigma_{y\gamma}^{c}$ respectively represent the bulk yield strengths of α and γ phases corrected for variations in grain size and texture, and $I_{\alpha\gamma}^{y}$ is due to the interaction between α and γ phases.

From equation [2.13], it is clear that the interaction between the two phases does indeed modify the ultimate yield strength. The interaction term can either be additive or subtractive depending on factors such as microstructure, alloy system and composition as illustrated in Figure 2.4.

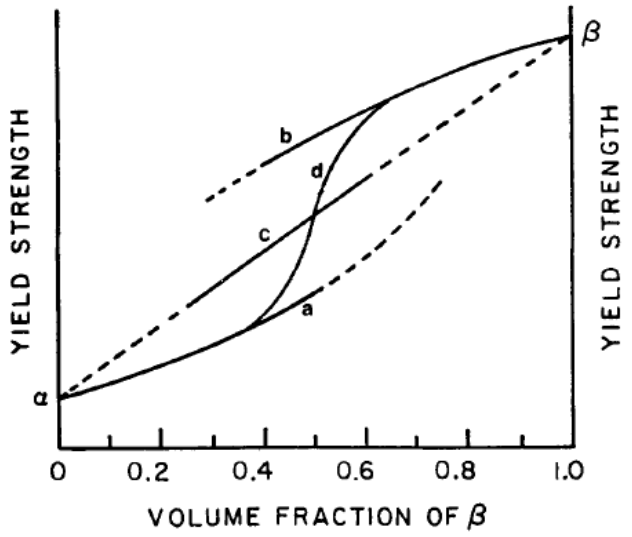

Figure 2.4: Schematic representation of the variation of yield strength as a function of composition: (a) discontinuous hard phase, continuous soft phase; (b) continuous hard phase, discontinuous soft phase; (c) both phases continuous; (d) transition between structure (a) and structure (b) **[73]**.

Despite the capability of equation [2.13] to explicitly feature the interaction term, it does however fail to identify the contribution of each phase to the alloy is strength and ultimately

its flow behaviour. This led to the development of the "modified" law of mixtures, first empirically by Tamura *et al*. [74] and subsequently applied by Fischmeister and Karlsson [75]. The "modified" law of mixtures uses the average stresses and strains in each phase to describe adequately the distribution of stress and strain between the constituents [73].

For an alloy consisting of two phases α and γ, under uniaxial loading, the modified law of mixtures is given by the following equations [73]:

$$\sigma_c = \bar{\sigma}_\alpha V_\alpha + \bar{\sigma}_\gamma V_\gamma \qquad [2.14]$$

$$\varepsilon_c = \bar{\varepsilon}_\alpha V_\alpha + \bar{\varepsilon}_\gamma V_\gamma \qquad [2.15]$$

where V is the volume fraction, and $\bar{\sigma}$ and $\bar{\varepsilon}$ are average values, respectively of the directional components of stress and strain parallel to the load direction. The subscript c refers to the composite alloy (not to be confused for critical stress or strain).

It is confirmed that the equations above are applicable to any direction of loading and all possible structural arrangements of two-phase mixtures, also encompassing the limiting cases of parallel and series arrangements of the constituents. Of noteworthy is despite all the attributes of the modified law of mixtures, it still does seem to hold in cases where the volumes of the phases or constituents remain static during plastic deformation. This however, might not always be the case as shown in the study in titanium alloys where straining during thermo-mechanical processing triggers a phase transformation [76]. The same phenomenon is also applicable to other metals such as steel [77] [78], hence the need to address this in the case of the material under study: duplex stainless steel and how this may affect the overall flow behaviour.

Chapter 3

3. Plastic Flow Stress and Related Mechanisms

Analysis of the plastic flow behaviour is important in the estimation of flow stress and in determining the required forces for deformation of that particular material. In addition, this also helps in achieving the dimensional accuracy of final products from processes such as hot rolling.

The general consensus is that the plastic flow behaviour can be described by flow stress curves, Figure 3.1. Flow stress curves are mainly divided into the regimes of work hardening and softening. A balance can also be between work hardening and softening resulting in a third regime. Each of these regimes is characterized by interaction between dislocations and microstructural evolution within the material.

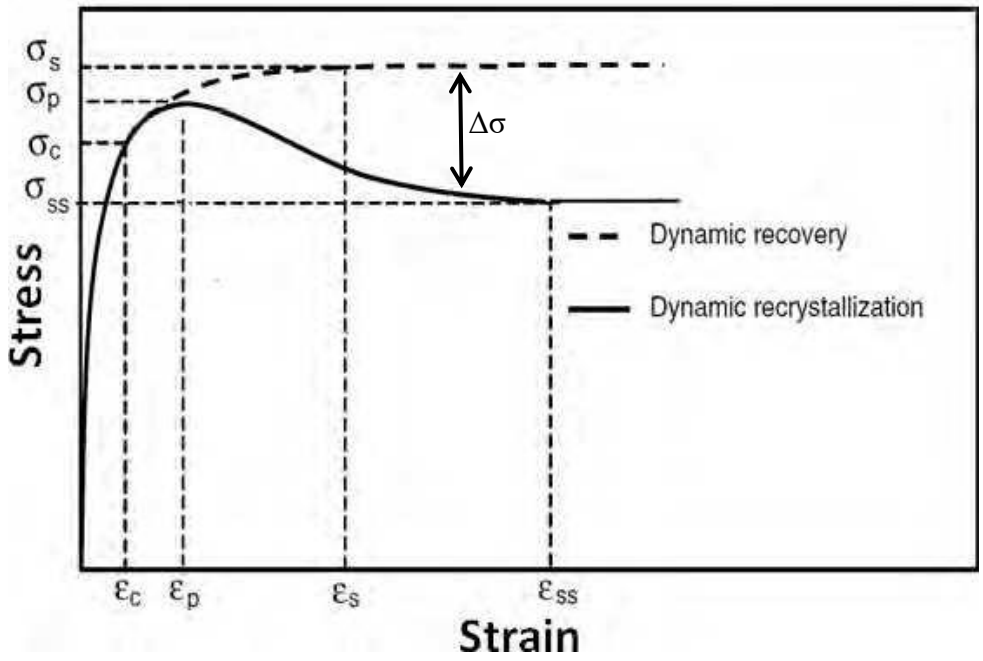

Figure 3.1: Typical flow curves during hot deformation.

Nes et al. [79] came up with a model to describe the evolution of microstructure during deformation, and in this model they considered three global parameters. These are the dislocation density inside the cells (ρ_i), the cell/subgrain size (δ) and the cell/sub-boundary misorientation (at low strains this will be the cell wall thickness and dislocation density in the cell wall). The model of Nes et al. [79] is depicted in Figure 3.2.

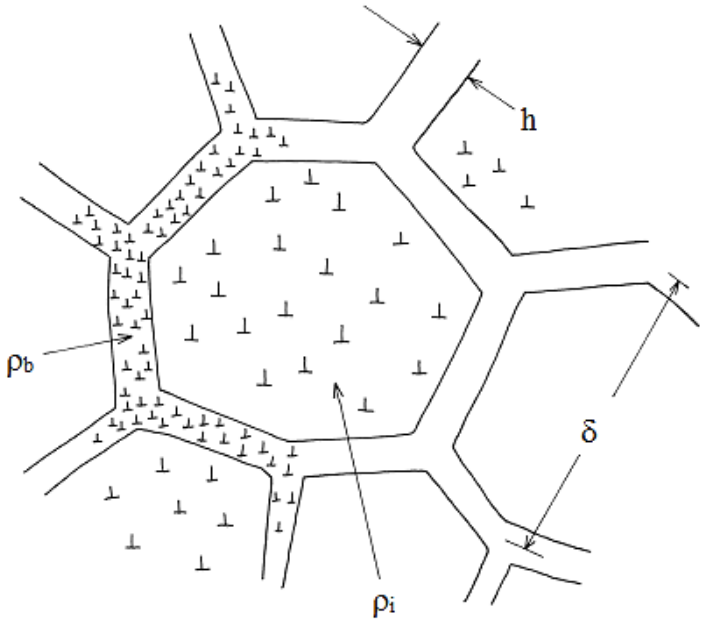

Figure 3.2: A schematic presentation of the microstructure, cell diameter δ, cell wall thickness h, cell wall dislocation density ρ_b and dislocation density within the cell ρ_i **[79].**

Nes et al. [79] developed the model above for pure metals with fcc structures. However, it can still be used to illustrate the dislocation-microstructure interaction within the work hardening regime of flow stress. The most important elements being the cell/subgrain size δ and the dislocation density in the cell interior ρ_i. Within this hardening regime, the evolution of dislocation density (ρ) is controlled by the competition between dislocation storage and annihilation and is considered to be the sum of two independent terms [69], [79].

$$\frac{d\rho}{d\varepsilon} = \left(\frac{d\rho}{d\varepsilon}\right)^{WH} + \left(\frac{d\rho}{d\varepsilon}\right)^{RV} \qquad [3\text{-}1]$$

where ρ is the dislocation density.

The first term on the right hand side of equation [4-1] stands for the work hardening rate and the second term denotes the contribution of DRV. The change in strain however, does not have any influence on the work hardening term [80], [81], [82] but dislocations continue to evolve such that the above can be rewritten as [83]:

$$\frac{d\rho}{d\varepsilon} = h - r\rho \qquad [3\text{-}2]$$

where h is the athermal work hardening rate and r denotes the rate of dynamic recovery at a given temperature and strain rate. The driving force for dynamic recovery is applied stress

while in static recovery, it is the defect interaction [79]. No energy changes take place during recovery, since the process only involves the rearrangement of dislocations into a configuration of lower energy through a series of events as shown below [63].

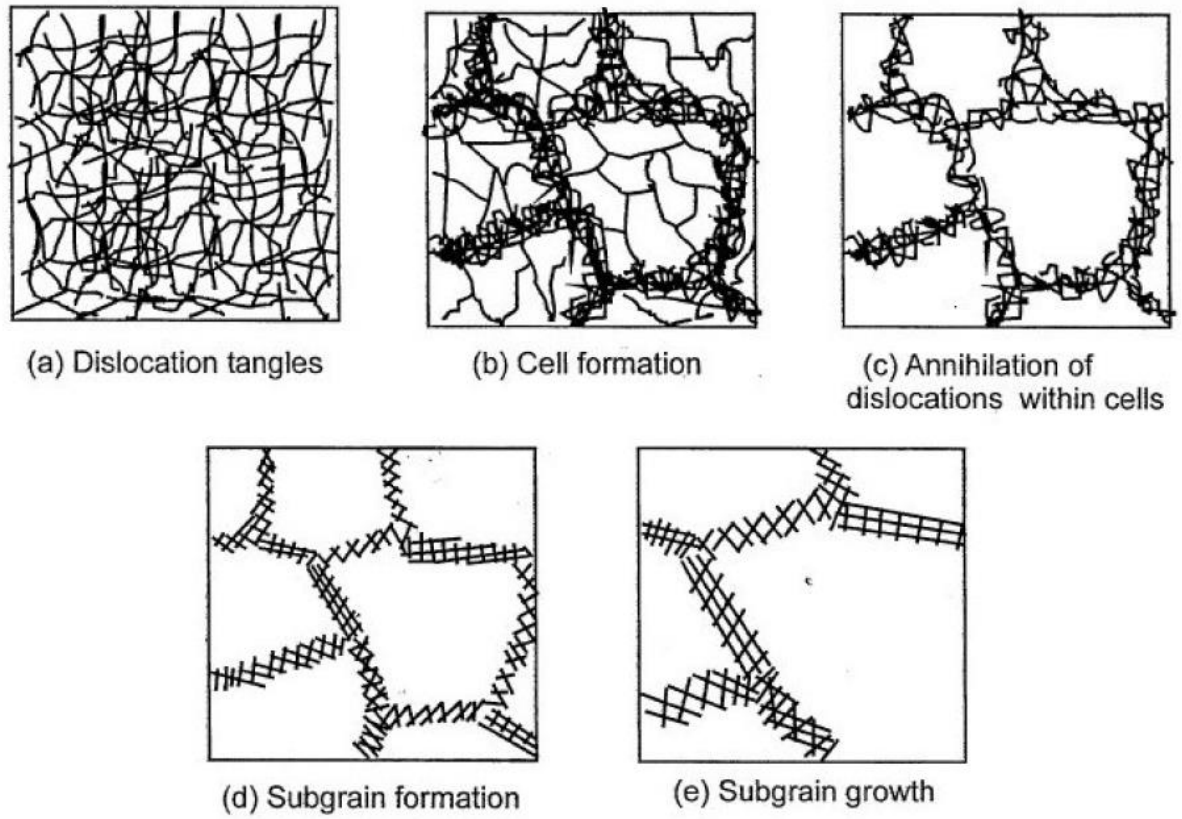

Figure 3.3: The stages of recovery where first cells are formed, to the rearrangement of dislocations and then subgrains which are formed and grow due to annihilation of dislocations [**63**].

Recovery readily takes place in materials with high stacking fault energy (SFE) through dislocation cross-slip and climb at high temperature [68], [84]. No dynamic softening takes place during recovery which generally results in a monotonic hardening to a steady-state plateau as shown in Figure 4.1 [68]. Ferrite has a high stacking fault energy and, therefore, generally undergoes DRV during deformation [85], [86], [87], [88], [89], [52], [53].

Equation [3-2] can be manipulated further to evaluate the flow behaviour of materials that undergo recovery only, or the flow behaviour of materials until the steady state is achieved, that is at the saturation stress. By integrating equation [3-1], using equation [3-2] and converting dislocation density into stress, the flow stress in the work hardening–dynamic recovery (WH + DRV) region can thus be deduced from [90]:

$$\sigma_{wh} = \left[\sigma_{sat}^2 - (\sigma_{sat}^2 - \sigma_0^2)exp\left(-r(\varepsilon - \varepsilon_0)\right)\right]^{1/2} \quad [3\text{-}3]$$

where σ_{wh} is the work hardened flow stress, σ_0 is the yield stress (at yield stress $\rho = \rho_0$ and $\varepsilon = \varepsilon_0$) and σ_{sat} is the saturation stress. The saturation stress is dependent on the rate of dynamic recovery, r and the athermal work hardening rate, h through [91]:

$$\sigma_{sat} = M\alpha G_m b\sqrt{(h/r)} \quad [3\text{-}4]$$

In the WH + DRV region, the stress-strain relationship can also be expressed by the generalized Voce equation [92] below:

$$\sigma = \sigma_0 + (\sigma_p - \sigma_0)[1 - exp(-C\varepsilon)]^e \quad [3\text{-}5]$$

The initial stress σ_0 in hot working is very small compared to the peak stress such that the Voce equation can be rewritten as:

$$\sigma_{(WH+DRV)} = \sigma_p[1 - exp(-C\varepsilon)]^e \quad [3\text{-}6]$$

where the coefficient C and WH exponent e are dependent on the strain rate and temperature.

Conversely, still within the work hardening region, equation [3-4] can be re-written by considering the contribution of the dislocation density ρ to the flow stress σ through the following relationship [82], [93], [94]:

$$\sigma = \gamma G_m b\sqrt{\rho} \quad [3\text{-}7]$$

where γ is the Taylor constant, b is the Burger's vector, G_m is the shear modulus and the variations of dislocation density ρ during hot deformation, is given as [62]:

$$\rho = \rho_0 exp(-\Omega\varepsilon) + \frac{U}{\Omega}[1 - exp(-\Omega\varepsilon)] \quad [3\text{-}8]$$

Substituting for the dislocation density ρ of equation [3-8] into [3-7], then σ can be given as:

$$\sigma = \gamma G_m b\left[\rho_0 exp(-\Omega\varepsilon) + \frac{U}{\Omega}\left(1 - exp(-\Omega\varepsilon)\right)\right]^{1/2} \quad [3\text{-}9]$$

Assuming that the initial dislocation density ρ_0 at $\varepsilon = 0$, is so much smaller than ρ during hot hot working that it may be discarded and equation [3-9] can be reduced to:

$$\sigma = \gamma G_m b \left[\frac{U}{\Omega}\left(1 - exp(-\Omega\varepsilon)\right)\right]^{1/2} \quad [3\text{-}10]$$

U is the work hardening rate, the term Ω is the remobilization parameter which contains an athermal contribution (Ω_0) and a thermal and strain rate dependent contribution (Ω_1), expressed as follows:

$$\Omega = \Omega_0 + k\left(\dot{\varepsilon}\, exp\left(\frac{-Q}{RT}\right)\right)^n \quad [3\text{-}11]$$

where k and n are model coefficients. The dislocation density ρ_{ss} during the steady state flow stress due to DRV can be expressed as [82], [93], [94]:

$$\rho_{ss} = \frac{U}{\Omega} \quad [3\text{-}12]$$

Hence, equation [3-11] can be modified accordingly and be re-written as:

$$\sigma = \left[\sigma_{ss}\left(1 - exp(-\Omega\varepsilon)\right)\right]^{1/2} \quad [3\text{-}13]$$

$$\text{where } \sigma_{ss} = \gamma G_m b\sqrt{\rho_{ss}} \quad [3\text{-}14]$$

σ_{ss} is the steady state stress in the work hardening region which can be predicted from the work hardening rate – stress plot using a method that will be discussed later.

By considering interplay between storage and annihilation of dislocations as still being the main mechanism in the absence of DRX, Kocks and Mecking [95] proposed that from equations [3-2] and [3-6] the working hardening rate and flow stress can be expressed as [80]:

$$\theta = \theta_0\left(1 - \frac{\sigma}{\sigma_s}\right) \quad [3\text{-}15]$$

Estrin and Mecking [83] considered the storage rate U to be constant and modified the Kocks –Mecking method above to give:

$$\frac{d\rho}{d\varepsilon} = U - \Omega\rho \quad [3\text{-}16]$$

where U still represents the work hardening rate constant. The above equation can be rewritten in the following form:

$$\theta\sigma = A - B\sigma^2 \quad [3\text{-}17]$$

Integrating equation [3-17] results in the equation for the flow stress in the WH + DRV regime according to the Estrin-Mecking modification given by:

$$\sigma = [\sigma_{sat}^2 + (\sigma_0^2 - \sigma_{sat}^2)exp(-2\mathrm{B}\varepsilon)]^{1/2} \quad [3\text{-}18]$$

where: $\sigma_{sat} = \sqrt{\frac{A}{B}}$ [3-19]

3.1 Recrystallization and Softening

Recrystallization during hot deformation is important for it brings about a drop in flow stress (mill loads in the plant) indicated as Δσ in Figure 3.4. The drop in stress results in fractional softening of the flow stress of the material undergoing hot deformation. The stacking fault energy (SFE) is one aspect of fundamental importance with regards to recrystallization. Recrystallization is prominent in materials with a low-to-medium SFE, where DRV is less rapid and dislocations are able to accumulate to sufficiently high densities to trigger DRX [96]. In the case of high SFE materials, a dynamic balance between DRV and work hardening can be achieved at a relatively low level of dislocations due to relatively easy movement of dislocations through climb, cross slip and glide. The overall energy of the system is thus lowered through the formation of low angle subgrain boundaries. In essence, the occurrence of recovery in a material results in the reduction of the driving force for recrystallization [97]. The dislocation density critical for the initiation of DRX is altogether not attained, hence the absence of DRX. However, the asymptotic stress in the (WH + DRV) region, σ_{sat} represents the most work hardened grains and hence the driving force for the continuation of DRX upon further straining, as shown in Figure 3.4. The fraction of the material that has dynamically recrystallized is given as:

$$X_s = \left(\frac{\sigma_{sat} - \sigma}{\sigma_{sat} - \sigma_{ss}}\right) \quad [3\text{-}20]$$

where σ_{sat} is the saturated stress at steady state, σ is the flow stress at the strain ε and σ_{ss} is the experimental flow stress at the steady state stress.

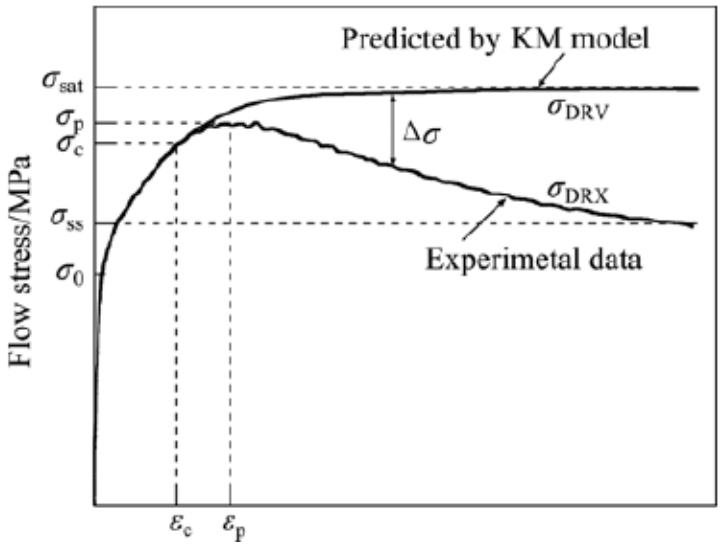

Figure 3.4: Stress – strain curve during hot deformation showing the typical softening behaviour at high strains **[98]**.

The softening behaviour represented by equation [3-21] can also be expressed using the Avrami type equation. Following the works of Gronostajski [99] and Oudin *et al*. [100], the fractional softening can also be given as:

$$X = 1 - \exp\left[-r_c\left(\frac{\varepsilon}{\varepsilon_p}\right)^q\right] \qquad [3\text{-}21]$$

where r_c is a chemical composition dependent constant that indicates how fast the stress reaches a steady state and q, which is dependent on hot deformation conditions, indicates the softening kinetics. The values of these two constants r and q are found through fitting of experimental data.

ε_p is the peak strain, defined as:

$$\varepsilon_p = A_1 D_0^m Z^u \qquad [3\text{-}22]$$

where A_1, m, u are material constants and D_0 is the initial grain size.

Substituting for X_S in equation [3-20] by equation [3-21], the variation of stress with strain during DRX (strain hardening and softening at $\varepsilon > \varepsilon_p$) is written as:

$$\sigma = \sigma_{ss} + (\sigma_{sat} - \sigma_{ss})\, exp\left[-r\left(\frac{\varepsilon}{\varepsilon_p}\right)^q\right] \qquad [3\text{-}23]$$

The flow stress behaviour after the peak strain given by equation [3-23] can be generally expressed as:

$$\sigma = \sigma_{WH+DRV} - \sigma_{DROP} \qquad [3\text{-}24]$$

where the first term on the right hand side has already been defined and σ_{DROP} is the drop in stress due to DRX.

Recrystallization is generally considered to be the movement of an interface such as a grain boundary between a recrystallized and unrecrystallized material. Like any other reactions or processes, the driving force behind recrystallization is the lowering of the system's free energy. Figure 3.5 shows a schematic diagram of an interface with an area element of dA moving through a distance dx resulting in the lowering of the free energy as a depiction of the process of recrystallization.

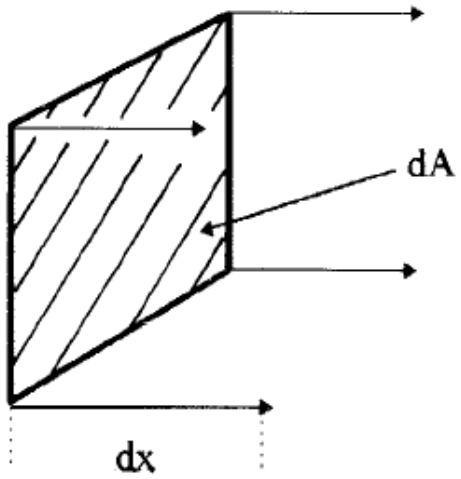

Figure 3.5: Schematic diagram illustrating the movement of a volume element dA.dx from an area of low stored energy to an area of higher stored energy.

Considering Figure 3.5, the change in free energy due to movement of the interface is given by:

$$dG = -p\, dA\, dx = -p\, dV \qquad [3\text{-}25]$$

Hence the driving force or the free energy change per unit volume due to movement of the interface or grain boundary is:

$$p = -\{dG/dV\} \qquad [3\text{-}26]$$

Three models have generally been developed for the nucleation of recrystallization namely: classical nucleation theory, strain induced boundary migration (SIBM) and sub-grain coalescence. The first two are applicable to low deformations up to 50% while the third is relevant to higher deformations of typically 80%.

3.1.1 Classical nucleation theory

The classical nucleation theory was adopted from phase transformations into recrystallization by Burke and Turnbull in 1952. This theory postulates that nucleation is established by embrionic random atomic fluctuations leading to the formation of a thermodynamically stable small crystallite with a high angle grain boundary [63].

3.1.2 Strain induced boundary migration

The SIBM model is also known as the Bailey-Hirsch model. A defect free-area at a high angle grain boundary may bulge into a higher energy grain through boundary migration. Since this process takes place under strain, it is termed strain induced boundary migration (SIBM). The driving force for SIBM between two adjacent grains is the difference in their stored energies due to differences in dislocation densities. This difference in the stored energies will be the driving force for the grain at lower energy to grow into the higher energy deformed matrix. As the boundary migrates it leaves a region of lower dislocation content behind it, as shown in Figure 3.6.

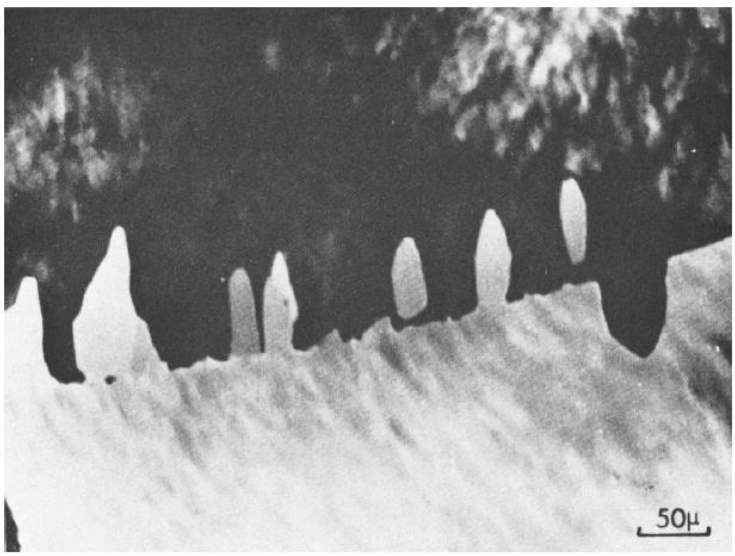

Figure 3.6: Optical micrograph showing strain- induced grain boundary migration in aluminium **[101]**.

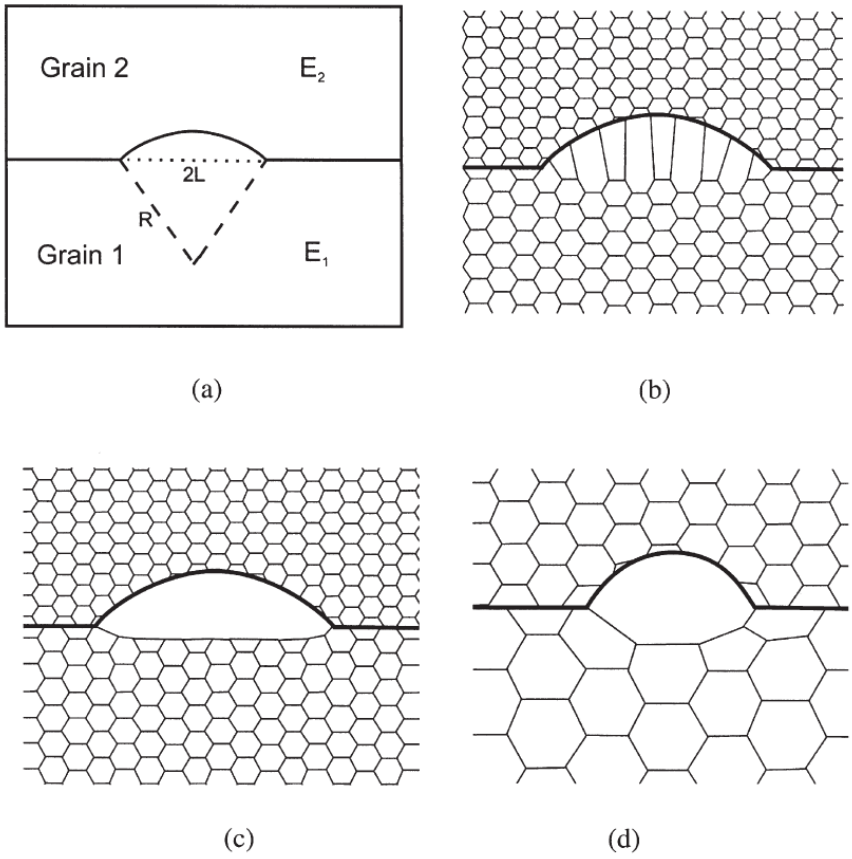

Figure 3.7: (a) Boundary separating a grain of low stored energy (E1) from one of higher energy (E2) migrating due to SIBM, (b) the dislocation structure is dragged behind the migrating boundary, (c) the migrating boundary is free from the dislocation structure, (d) recrystallization originating at a single large grain **[63]**.

Considering the capped region in Figure 3.7 (a) above, the capped region at the hemispherical condition is associated with the stored energy (E_B) given by:

$$E_B = 2\pi R^2 \gamma \qquad [3\text{-}27]$$

where R and L are as shown in the figure, γ is surface energy per unit area.

$$\frac{dE_B}{dR} = 8\pi R\gamma \qquad [3\text{-}28]$$

The energy of the system is lowered as the high energy grain is replaced by a low energy grain. Thus the capped region will now be associated with a free energy change given by:

$$G_v = \frac{2\pi}{3} R^3 \Delta G_{SIBM} \qquad [3\text{-}29]$$

Differentiating equation [3-29] above:

$$\frac{dG_v}{dR} = 4\pi R^2 \Delta G_{SIBM} \qquad [3\text{-}30]$$

where ΔG_{SIBM} is the difference in energy per unit volume between the two grains.

For the bulge to grow: $\frac{dG_v}{dR} > \frac{dE_B}{dR}$ [3-31]

Hence, $R > \frac{2\gamma_b}{\Delta E}$ [3-32]

A critical value is reached when the bulge becomes hemispherical, i.e. $R = R_{crit} = L$ and

$R_{crit} > \frac{2\gamma_b}{\Delta E}$. [3-33]

The effect of dislocations from plastic deformation is an internal energy E which is the resultant of the heat supplied to the system Q and the work done on the system W. In hot working processes, however, PΔV and VΔP are usually negligible. In dislocations also, ΔS is usually very small which makes ΔG≈ ΔE. Thus, ΔG and ΔE, can be used interchangeably, as is the case in some parts of this work, see appendix 8.

3.1.3 Subgrain rotation and coalescence model

This model was originally developed by Hu in 1962. The theory of subgrain rotation and coalescence was further developed by Li [102]. The theory points out that, subgrains rotate through subgrain diffusion, coalesce and eventually form a high angle boundary that is mobile through which recrystallization will take place, Figure 3.8.

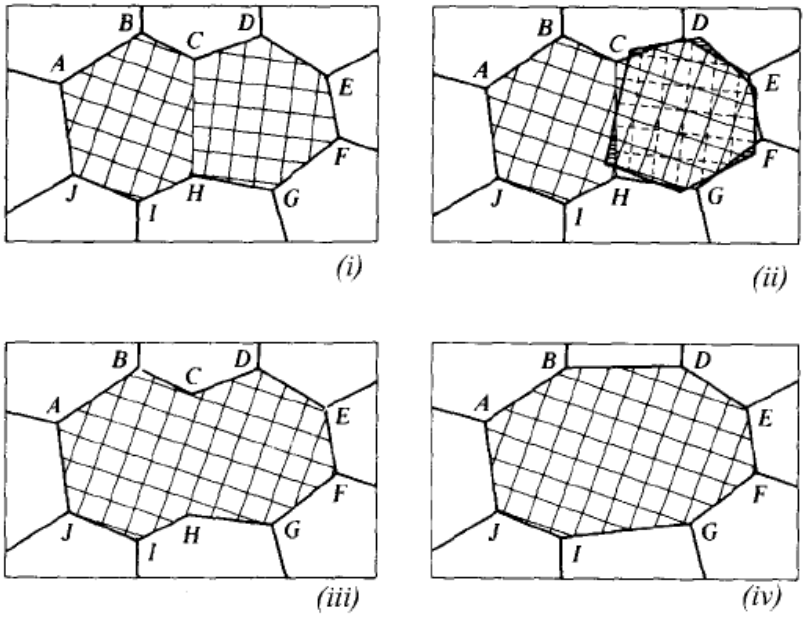

Figure 3.8: Schematic representation of subgrain rotation, leading to coalescence and an increase in orientation difference at the growth front. (i) Original subgrain before coalescence, (ii) Subgrain CDEFGH rotates through boundary diffusion (iii) The original orientation difference between the two subgrains has disappeared and the orientation difference at the front DEFG is now larger (iv) Grain boundary sections BCD and IHG straighten out to achieve a lower energy state **[102]**.

3.2 Dynamic Recrystallization

As already pointed out above, dislocations are associated with a certain elastic energy and their accumulation in metals or alloys during deformation will result in an increase in the internal energy of the material. This energy can be reduced through lowering of the dislocation content in the material [97]. Dynamic recrystallization is one such process where the system lowers the stored energy from dislocations through discontinuous nucleation of new dislocation-free grains which also migrate into the nearby matrix that still has structural defects.

Dynamic recrystallization strongly depends on high angle grain boundaries and is often preluded by the bulging of these grain boundaries. Two schools of thought pertaining the cause of this grain boundary bulging are; strain induced boundary migration and a mechanism proposed by Drury and Humphreys [103] of boundary sliding resulting in lattice rotation at grain serrations. The growth of a dynamically recrystallized grain is an energy dependent process which requires the driving force for growth. This driving force is a

function of the distribution and density of dislocations in the form of subgrains and free dislocations. The process of dynamic recrystallization is schematically depicted in Figure 3.9.

As the boundary at A moves from the left to the right into unrecrystallized material which has a high dislocation density ρ_m, the dislocation density in its vicinity is sharply reduced. Since this is under dynamic conditions, the continued deformation will raise the dislocation density in the new grain, so that it builds up behind the moving boundary and reaches ρ_x at a distance x behind the boundary. This value once again tends toward a value of ρ_m at large distances.

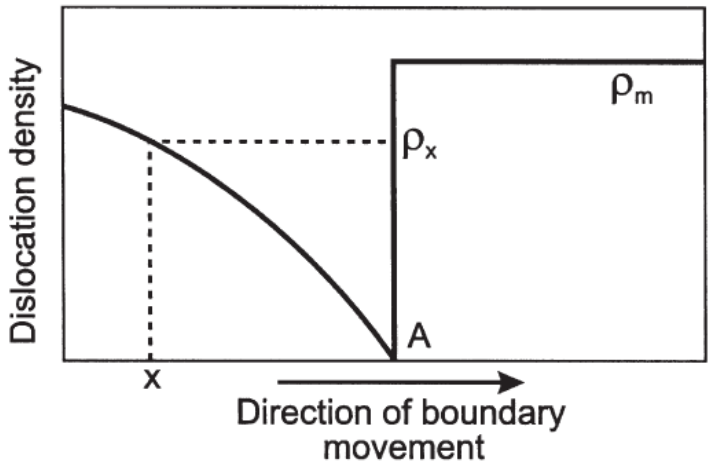

Figure 3.9: Schematic diagram of the dislocation density at a dynamic recrystallization front **[58]**.

The difference in dislocation density across the boundary gives rise to the driving force which moves the migrating boundary with a rate:

$$\frac{dx}{dt} = M\rho_m G_m b^2 \qquad [3\text{-}34]$$

By differentiating equation [3-34] that relates the applied strain ε, dislocation density ρ and mean slip distance of dislocations L:

$$\varepsilon = \rho b L \qquad [3\text{-}35]$$

The rate of increase of dislocation density behind the migrating boundary due to continuing deformation is given as:

$$\frac{d\rho}{dt} = \frac{\dot{\varepsilon}}{bL} \qquad [3\text{-}36]$$

Making dt in equation [3-34] subject of the formulae and substituting for dt in equation [3-36] gives:

$$\frac{d\rho}{dx} = \frac{\dot{\varepsilon}}{MLGb^3\rho_m} \quad [3\text{-}37]$$

and $\rho = \frac{\dot{\varepsilon x}}{MLGb^3\rho_m}$ [3-38]

Thus, it can be inferred that the dislocation density behind the moving boundary will reach the value of ρ_m when $x = x_c$, hence

$$x_c = \frac{MLGb^3\rho_m^2}{\dot{\varepsilon}} \quad [3\text{-}39]$$

Assuming nucleation has occurred through the bulge mechanism, the critical condition for formation of a nucleus of diameter x_c is given:

$$E_B > \frac{2\gamma_b}{x_c} \quad [3\text{-}40]$$

From above, E is the stored energy and this is considered to be a fraction K of the driving pressure ($\rho_m G_m b^2$). Considering the equation [3-39] and [3-40], the condition for nucleation is:

$$\frac{\rho_m^3}{\dot{\varepsilon}} = \frac{2\gamma_b}{KLMGb^5} \quad [3\text{-}41]$$

At a particular temperature, the term $\frac{2\gamma_b}{KLMGb^5}$ on the right hand side of equation [3-41] is a constant, such that nucleation for dynamic recrystallization requires that a critical value of $\frac{2\gamma_b}{KLMGb^5}$ needs to be achieved before nucleation can proceed. This value is however reduced mostly by an increase in boundary mobility; hence an increase in boundary promotes dynamic recrystallization.

Having an understanding of the driving force behind dynamic recrystallization taking place, it is also crucial to understand how it proceeds in the existing microstructure and subsequent microstructural changes taking place. Old grain boundaries are commonly preferential sites for initiation of dynamic recrystallization. New grains are thus subsequently nucleated at the boundaries of the growing grains. A thickening band of recrystallized grains is formed

without any significant change in the mean size of the dynamically recrystallized grains as shown in Figure 3.10.

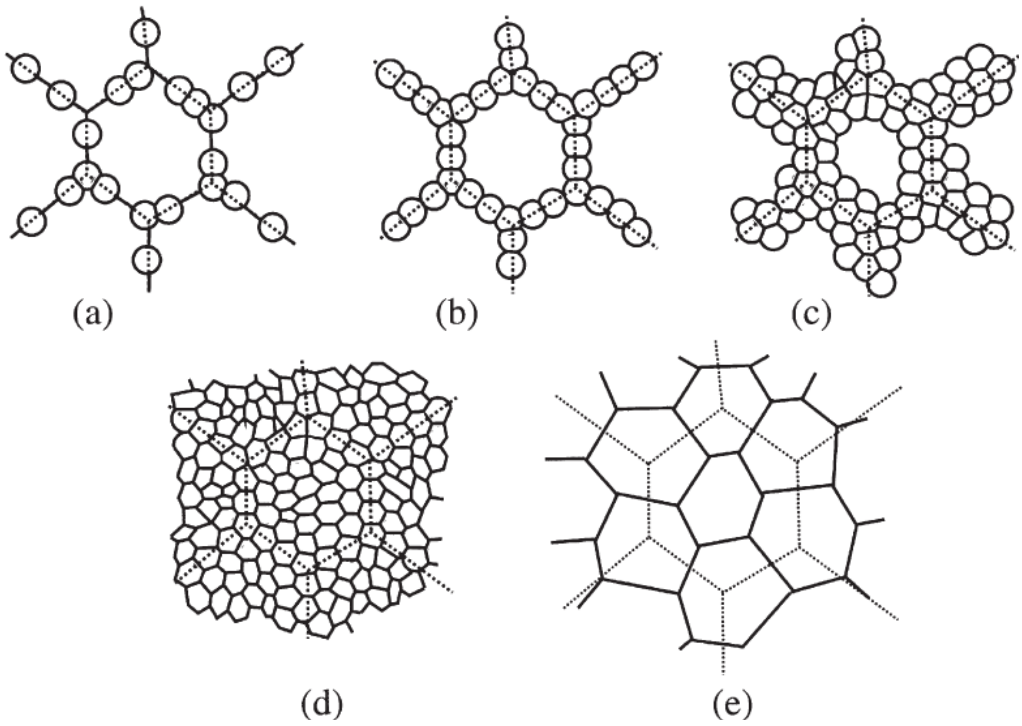

Figure 3.10: The development of the microstructure during recrystallization. (a)-(d) A large initial grain size, (e) a small initial grain size. The dotted lines show the prior grain boundaries **[63]**.

3.2.1 Dynamic recrystallization in single phase austenite

Metals and alloys such as Cu, Ni and austenitic steels have a low-to-medium SFE and as such do undergo dynamic recrystallization during hot working [104], [105], [106], [107], [108]. Due to limited glide and climb in austenite, DRV is very limited and sufficient stored energy to trigger DRX is often attained. In the austenite recrystallization region, new strain free refined grains are produced without any ferrite generation [109]. As the strain or dislocation free grains replace the deformed structure through migration of high angle grain boundaries, softening takes place which decreases the work hardening rate thus producing a clear stress peak. The significant drop in flow stress from the peak stress σ_p to low flow stress values by DRX is very crucial to adjustment of mill loads during hot rolling in industry. Further straining will result in a decrease in flow stress until a dynamic equilibrium between strain hardening and strain softening due to formation of new grains and the associated boundary migration is reached [110]. Several studies [84], [111], [112] have confirmed that a critical strain has to be attained first before dynamic recrystallization can take place.

Deformation of austenite to low strains was observed to result in equiaxed grains in the microstructure being elongated and the formation of serrated grains [113], [114]. DRX in austenite has since been confirmed [115], [116], [117], [118] to proceed by formation of new small grains which form at pre-existing grain boundaries through the mechanism of bulging, giving rise to what has become to be popularly known as the necklace structure. Dehghani-Manshadi *et al*. [113] and Abbaspour and Farmenesh [114] confirmed the formation of more DRX grains on the interface of the first necklace layer and un-recrystallized material (i.e. at the recrystallization front). Figure 3.11 shows how the DRX proceeds in austenitic material through the bulging mechanism as the material is deformed to higher strains.

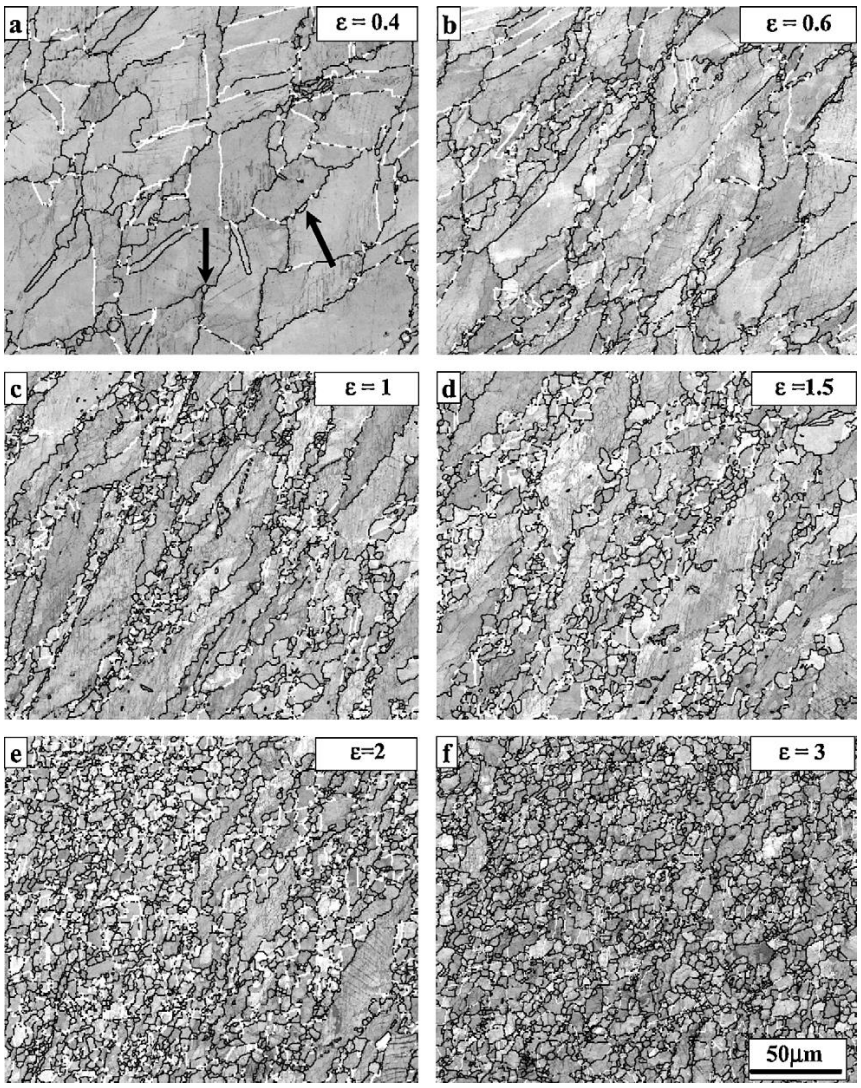

Figure 3.11: EBSD maps of austenitic steel samples deformed at 900 ^{o}C and strain rate of 0.01 s^{-1}. High angle (θ >15^{o}) and twin boundaries shown by black and white lines respectively (ε_c = 0.45; ε_p = 0.8) **[113]**.

3.2.2 Dynamic recrystallization in single phase ferrite

It is now well confirmed that high SFE materials such as ferritic steels and ferrite soften by dynamic recovery due to rearrangement and annihilation of dislocations which takes place with relative ease at high temperatures [119]. DRV is characterized by appearance of equiaxed sub-grains. These sub-grains are formed in the strain hardening region during hot working and reach an equilibrium size which is maintained throughout the steady state [120]. The other characteristic of DRV is that it results in low deformation resistance and a low apparent activation energy for deformation Q_{app} [121], often observed when high SFE materials are deformed. However, unlike DRX, DRV does not result in a decrease in flow stress during hot working (Figure 3.1). Despite, above norm that "high SFE materials cannot undergo DRX", there are a large number of studies showing that DRX readily occurs in high SFE materials, such as ferritic steels. Studies by Gao *et al*. [122] showed that ferritic stainless steels can still undergo dynamic recrystallization through subgrain rotation. Work by Glover and Sellars [123] in α-iron also confirmed that indeed the dynamic restoration mechanisms in this material can change from dynamic recovery (DRV) to DRX, depending on the value of Z. In the study by Glover and Sellars [123], DRV was prominent at high values of Z, i.e. at low temperatures and high strain rates and the restoration mechanism changed to DRX at low values of Z, i.e. high temperatures and low strain rates. The dependence of the processes of DRV and DRX on Z is confirmed through changes in the substructure with strain at different values of Z, Figures 3.12 and 3.13.

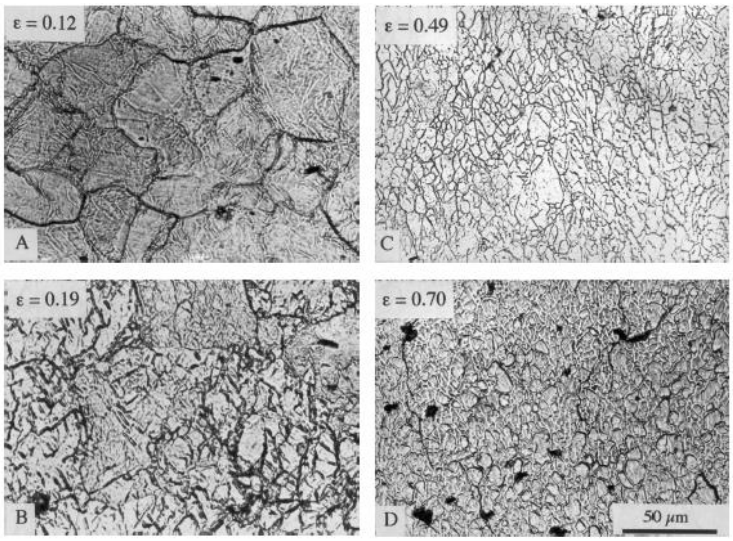

Figure 3.12: Optical micrographs showing substructures in Fe-26Cr deformed at 900 ^{o}C and 0.1 s^{-1} to strain of (a) 0.12 (b) 0.19 (c) 0.44 (d) 0.7 **[122]**.

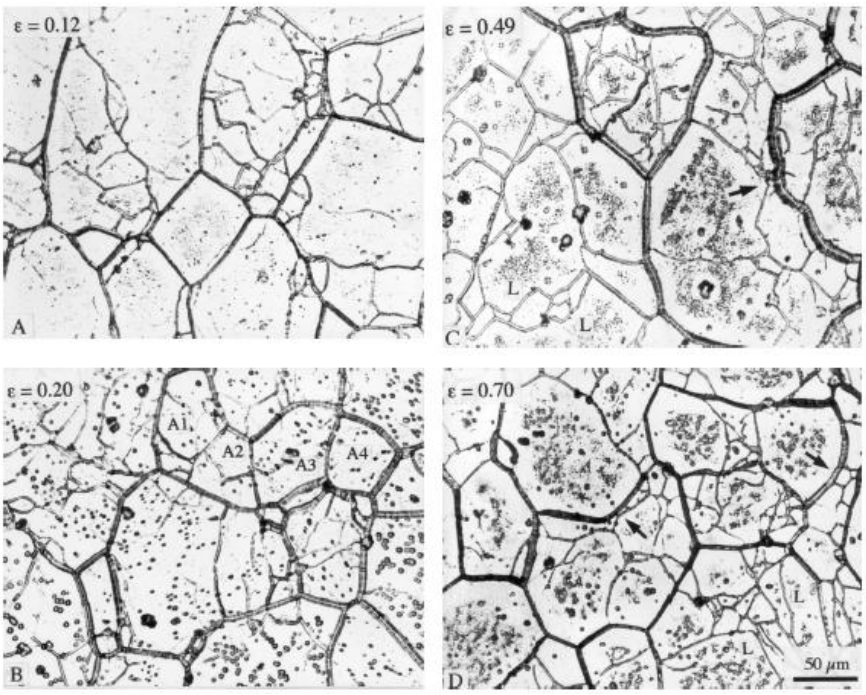

Figure 3.13: Optical micrographs showing substructures in Fe-26Cr deformed at 1100 ^{o}C and 0.05 s^{-1} to strain of (a) 0.12 (b) 0.20 (c) 0.44 (d) 0.7 **[122]**.

Gao *et al*. [122] also showed that the effect of Z on dynamic recrystallization of ferrite in both single phase ferritic and two-phase steels, can be represented schematically as shown in Figure 3.14. Confirming findings by Glover and Sellars [123], work by Gao *et al*. [122] also showed that at high values of Z, recovery dominated and interactions between dislocations in sub-boundaries was able to maintain a stable substructure in ferrite. The same work [122], also indicated dynamic recrystallization taking place at lower values of Z when new grains formed by coalescence of sub-grain boundaries and the rotation of sub-grains. Maki *et al*. [124] observed dynamic recrystallization in a 430 ferritic stainless deformed at above 1000 ^{o}C. All studies [122], [123], [124] indicated that high a temperature is favourable for DRX in ferritic steels.

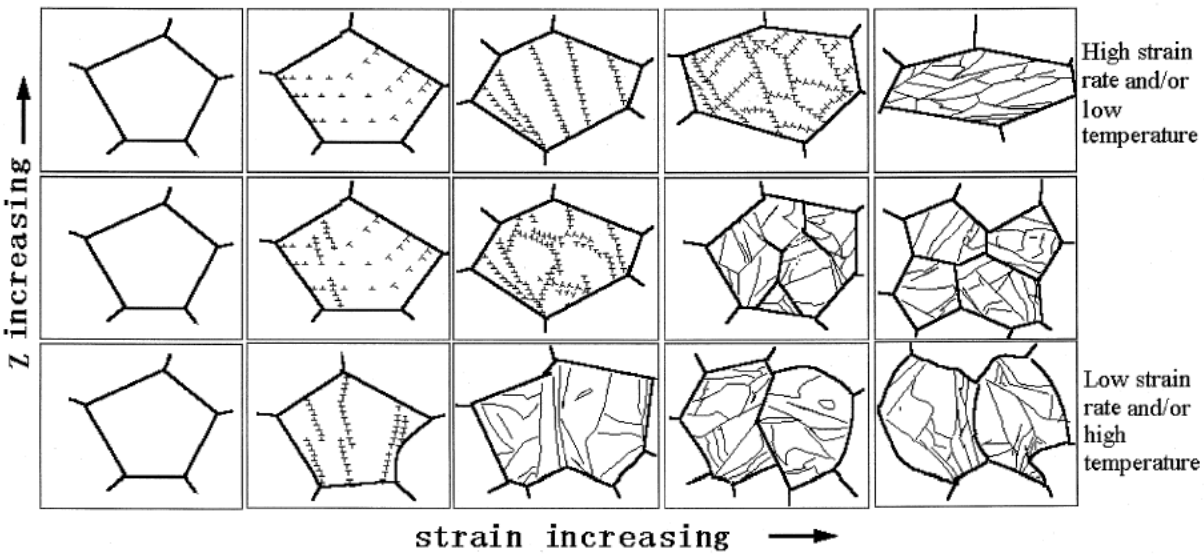

Figure 3.14: Schematic diagram showing the processes of substructure formation and annihilation and start of dynamic recrystallization with deformation at different Z values **[122]**.

3.2.3 Dynamic recrystallization in the two phase (austenite + ferrite) region

Due to the differences in their SFEs, recrystallization in austenite is known to be preceded by little recovery and is delayed in ferrite as recovery would have preceded recrystallization and removed some of the driving force for recrystallization. The two phase austenite-ferrite region is of importance as most dual phase stainless steel's thermomechanical processes are carried out in this region and the dynamic evolution of one phase affects the adjacent phase [55]. To be able to understand the dynamic recrystallization in the two-phase region, studies where deformation was carried out in the inter-critical region of low carbon steels need to be considered.

Several studies [55], [125] have confirmed that when a two phase material is strained, deformation is always concentrated in a softer phase, which is ferrite in this case. It is thus necessary to investigate the overall recrystallization behaviour in such materials. Studies by Pandi and Yue [126] in the two-phase region of austenite and ferrite in a low carbon steel, showed that austenite began recrystallizing only when the recrystallization of ferrite was more or less complete due to strain partitioning. It was confirmed in the same study [126], that the activation energy for deformation corresponding to the critical strain required for the onset of recrystallization in austenite, remained the same in single and in two-phase regions. In such case the dynamic recrystallization behaviour of austenite was unaffected by the

presence of ferrite. However, a study by Dehghani-Mansadi [127] showed that the presence of ferrite in the vicinity of austenite slowed down the DRX kinetics of austenite when compared to single phase material.

In another deformation study [55] carried out in the two-phase region, it was observed that austenite remained deformed and did not recrystallize, while a necklace structure of ferrite grains formed at ferrite/austenite grain boundaries instead of sub-grains. In the same study [55], nucleation of new recrystallized grains, i.e. discontinuous dynamic recrystallization (DDRX) was observed in ferrite that was in the vicinity of the harder austenite phase, resulting in intense local straining. Thus, a synergistic effect of processing variables and localized strain accommodation was assumed to take place, resulting in the transition from DRV to DDRX in ferrite in two-phase steels [55].

A study of deformation of a low carbon steel in a two phase ($\gamma + \alpha$) region by Simielli *et al.* [128] confirmed the findings by Mohamizadeh *et al.* [55], where austenite regions were observed to act as initiation sites for recrystallization within the deformed ferrite phase. This was in both cases attributed to strain localization in the ferrite surrounding the harder austenite phase. Hence, nucleation was observed to take place in the deformed ferrite near the interface. Sas *et al*. [129], showed that deformation carried out in a two-phase ($\gamma + \alpha$) region of a low alloy steel resulted in grains in both phases being deformed, with austenite grains becoming elongated, consequently providing larger surfaces for nucleation and phase transformation. Dislocation cells were also observed to form within the ferrite grains resulting in grain refinement through conversion of low-angle grain boundaries to high-angle grain boundaries. However, observations in the above study [129] seem to suggest that DRX takes place in the ferrite phase only.

Other studies [120], [130], [131] confirmed that austenite in the dual-phase of low carbon steel deformed in the same manner as austenite deformed in the non-recrystallizing region, with DIFT taking place. The same studies [120], [130], [131] also showed that in as much as austenite does not undergo DRX during warm deformation, ferrite does however and recrystallization nuclei preferentially nucleate at lattice defects such as grain boundaries and deformation bands. Ferrite recrystallization and hence refinement in the instance of warm deformation is attributed to various mechanisms such as DIFT, DDRX and CDRX [132], [133], [134], [135], [136].

3.3 Dynamic induced ferrite transformation

Dynamic induced ferrite transformation (DIFT) is a solid state process whereby austenite is deformed in the austenitic non-recrystallization region and transforms to ferrite during the process [137]. In other words, DIFT is a dynamic transformation (DT) of austenite to ferrite during deformation and in low carbon steels and austenitic steels occurs at definite temperatures close to Ar_3 or Ae_3 [109], [138], [132]. In the case that DIFT has occurred during plastic deformation, the ferrite grains will be more refined compared to when it is absent [130], [139], [140]. In the study by Choi *et al*. [141], observation of an increase in the fraction of polygonal ferrite with strain in Figures 3.15 and 3.16, showed the occurrence of DIFT. DIFT also contributes to softening during deformation giving rise to a single peak flow curve similar to that observed in DRX [112]. Thus, both DRX and DT are considered as flow softening mechanisms. In a study by Pandi and Sue [126], an increase in the ferrite fraction was observed when deformation was carried out in both single phase and in two-phase austenite-ferrite regions of low carbon steel. The increase in ferrite in both cases was attributed to dynamic induced ferrite transformation (DIFT). The effect of DIFT on flow behaviour is more prominent when deformation is carried out in a single austenite phase rather than the two phase austenite-ferrite region. Analysis of the flow behaviour in the two-phase region is complicated by strain accommodation between the two phases which can result in either softening or hardening [55]. However, though the process of DIFT was identified as early as the 1980s [142], the mechanism by which the process takes place still remains controversial [77]. Dong and Sun [77] point out that DIFT is different from both massive transformation and pro-euctoid ferrite transformation. Though dynamic transformation of ferrite or DIFT has been widely reported to take place in either single or two-phase regions of low carbon steels [109], reports of its occurrence in duplex steels are almost non-existent. Figures 3.17 and 3.18 show the dependence of microstructural evolution (misorientation angle distributions) in the ferrite phase with strain and temperature, respectively. Such studies help in understanding the softening mechanisms operating in each phase and contributing to the overall flow behaviour of the material.

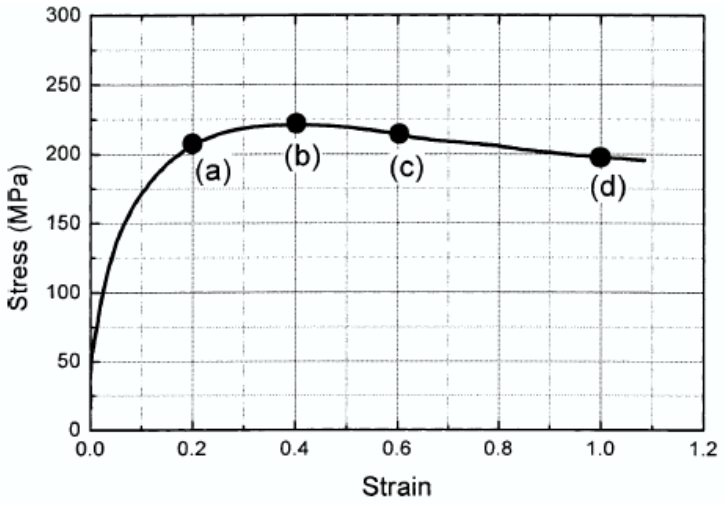

Figure 3.15: Evolution of flow stress with compressive strain at a deformation temperature of 750 ^{o}C in a low carbon steel ($\dot{\varepsilon} = 0.1\ s^{-1}$, reheating temperature = 1050 ^{o}C) **[141].**

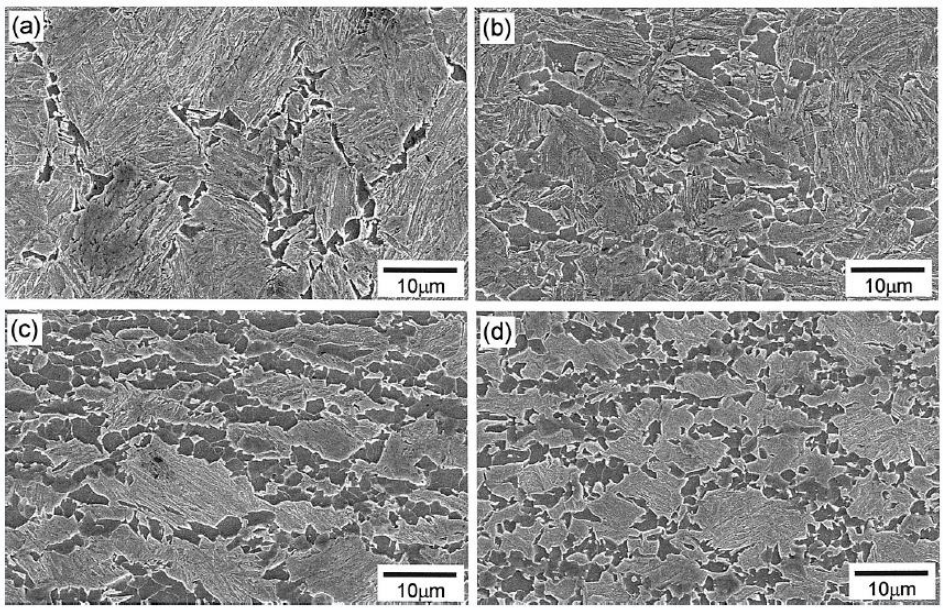

Figure 3.16: Microstructures (SEM) of quenched specimens at pre-set strain values in Figure 4.15: (a) ε = 0.2, (b) ε = 0.4, (c) ε = 0.6 and (d) ε = 1.0 **[141].**

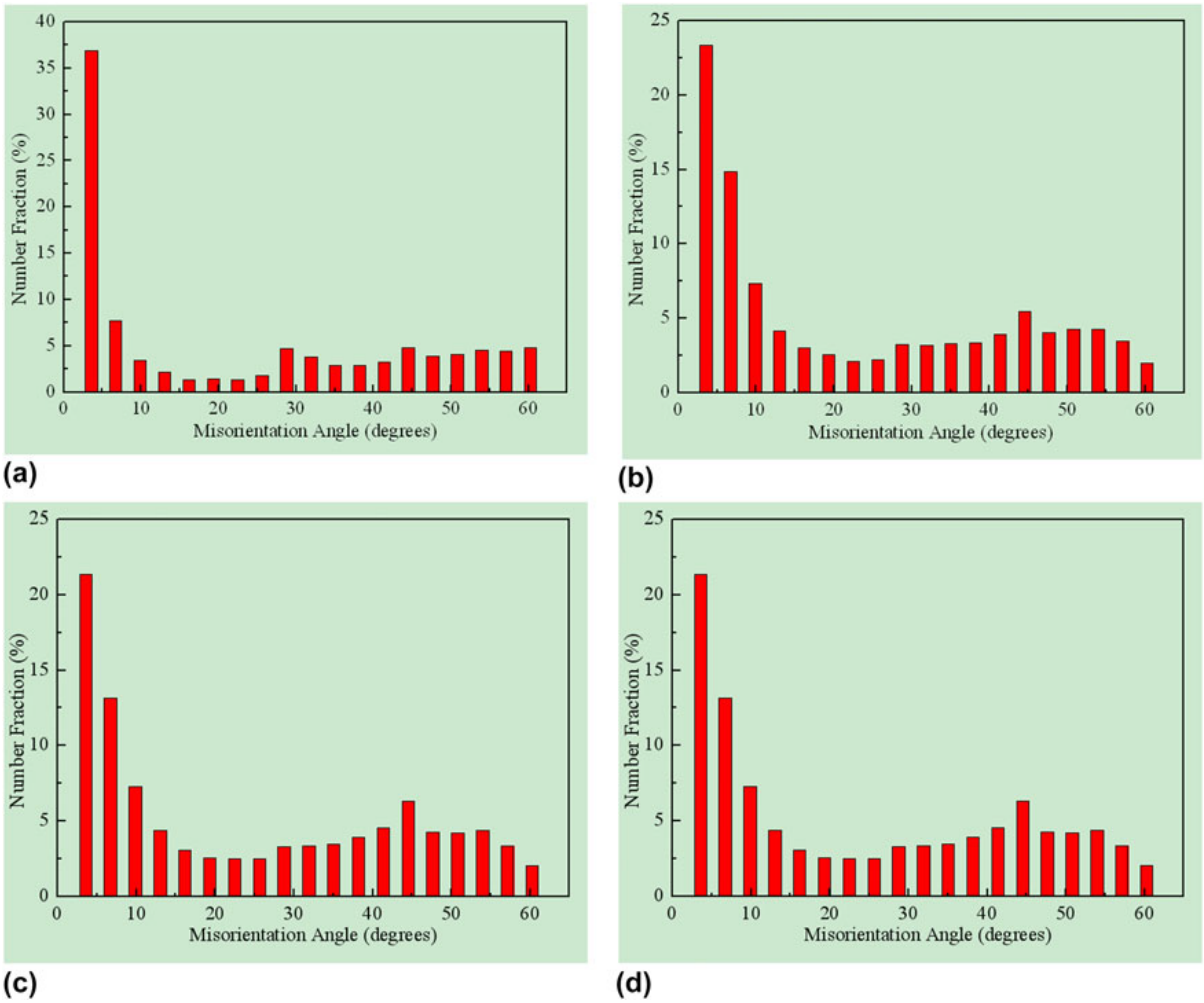

Figure 3.17: Distribution of misorientation angles in ferrite that had been warm deformed to different strains at 750 ^{o}C with a strain rate of 0.01 s^{-1}: (a) 0.69 (b) 0.91 (c) 1.2 (d) 1.4 **[109]**.

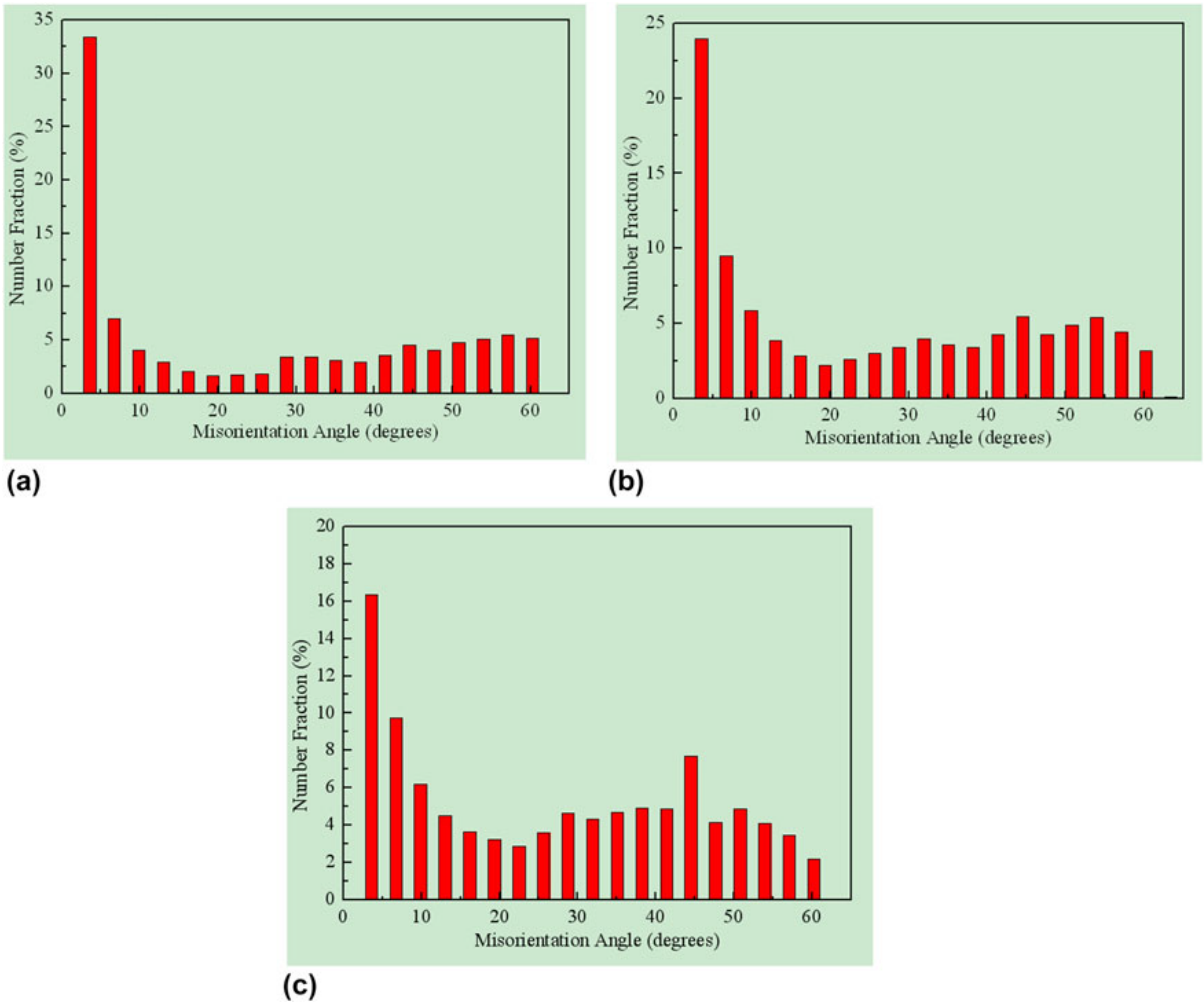

Figure 3.18: Distribution of misorientation angles in ferrite warm deformed at different temperatures to a strain of 1.2 and at a strain rate of 0.01 s^{-1}: (a) 850 ^{o}C; (b) 800 ^{o}C; (c) 775 ^{o}C **[109]**.

3.4 Critical strain for DT and DRX in austenite

Traditionally, the presence of the peak stress during hot deformation tests is more often considered as the reliable indication of the imitation of DRX [143], [144], [96]. Under certain conditions, DRX is known to have taken place despite the absence of stress peaks in the flow curve [145]. In some materials, especially in compression tests, the stress peaks are not that pronounced [22], [146], [147]. Thus, the use of a stress peak as an indicator to verify the presence of DRX in such materials will arguably not be advisable. To overcome that challenge, a number of studies [148], [145], [149], [150] have however used a method of identifying DRX, even in the absence of stress peaks. To achieve this, part of the flow curve in the plastic region was fitted and smoothed with a sixth order polynomial, as shown in Figure 3.19. The smoothed curve that is free of irregularities or fluctuations is differentiated

to obtain further information according to the Kocks-Mecking (KM) model [151], as shown schematically in Figure 3.20.

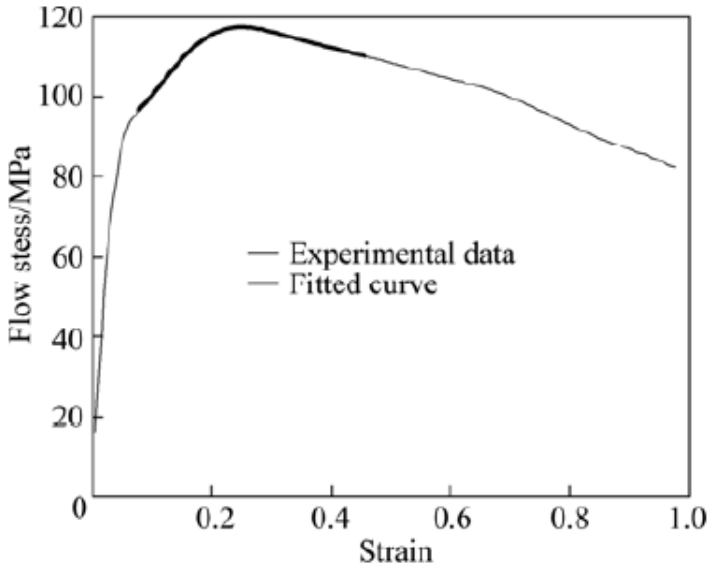

Figure 3.19: Experimental flow stress strain curve with a 6th order fitting in the plastic region **[152]**.

The inflection in the plot of strain hardening rate θ against stress σ or, alternatively, the inflection in the ln θ against ln σ plot is an indication of the occurrence of DRX [145]. The important parameter in DRX can then be determined as shown in Figure 3.20. The most critical point is the point where DRX is initiated which coincides with the critical stress σ_c or critical strain ε_c, where softening is basically attributed to early bulges of DRX. This point is always at a strain less than the peak strain ε_p, and represents the true stress or strain necessary for DRX to be initiated under those particular conditions for a given material. The decrease in the strain hardening rate ($d\sigma/d\varepsilon$) above the inflection point is due to DRV, as elaborated by Dehghan-Manshadi *et al*. [113]. Thus the gradient of the $d\sigma/d\varepsilon$-σ plot in Figure 3.20 represents the rate of dynamic recovery [69].

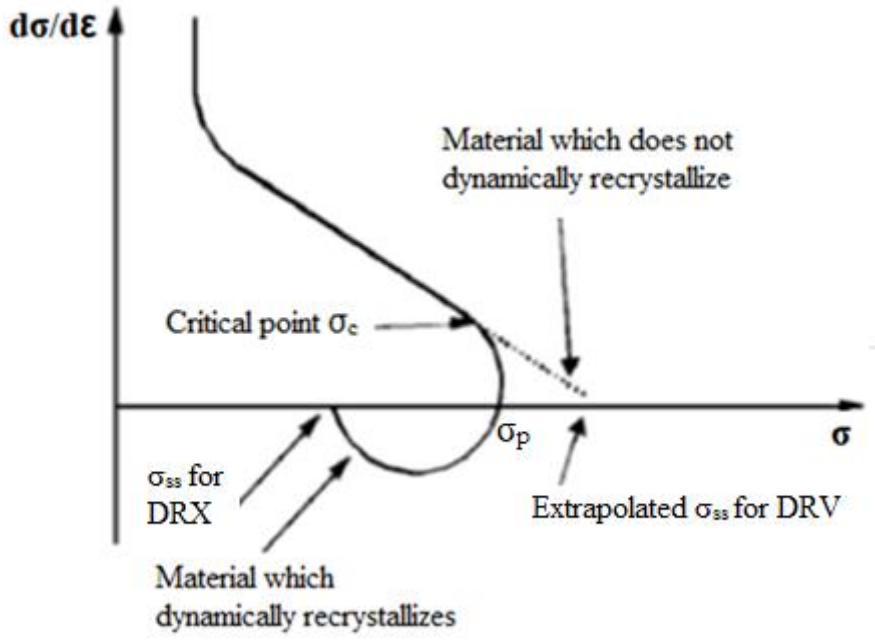

Figure 3.20: Schematic strain hardening plot indicating the determination of σ_c, σ_p and σ_{ss} **[148]**.

Figure 3.21 shows that though the strain hardening rate plots are better indicators of the occurrence of DRX than the presence of a peak stress in flow curves, locating the precise point corresponding to the critical stress, σ_c can still be a challenge. The peak stress σ_p and steady-state stress σ_{ss} can be easily determined since these are the points where the strain hardening curve cuts the stress axis. The first point it cuts, the stress axis corresponds to σ_p and the second to σ_{ss}. For the flow stress that does not attain a steady state there is only a single point where the strain hardening curve cuts the stress axis, that is, for peak stress. The difficulties associated with finding the precise value of σ_c from strain hardening plots are overcome by the use of ln-plots, that is, ln θ – ln σ plot, Figure 3.21. By using the ln θ – ln σ plot (Figure 3.21) instead of θ –σ plot (Figure 3.20) there is a significant improvement in the ease and accuracy with which σ_c can be determined.

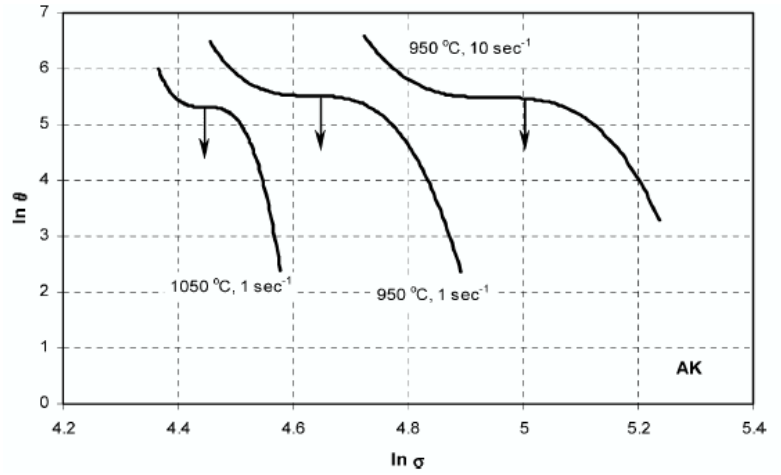

Figure 3.21: ln θ vs ln σ plot to determine σ_c **[145]**.

So far the appearance of a peak stress in the flow curve has been treated as a result of softening arising from DRX. According to studies that began in the 1980's [142], [153] an ubiquitous single peak flow curve can also result from microstructural and mechanical softening due to dynamic transformation (DT). Therefore, in addition to processes of recovery and recrystallization, concurrent phase transformation in the form of DIFT may also take place during deformation at elevated temperatures [63]. The process of dynamic transformation is also strain driven, it depends on energy acquired from deformation and hence it also has its critical strain as in the case of DRX. The double differentiation method used to determine the critical stress or strain in DRX can also be used to determine the critical strain in DT according to Sun *et al*. [154] and Choi *et al*. [141]. Figure 3.22 shows how the double differentiation method can be used in determining the critical strain associated with DT, where double minima appear, one for DT and another for DRX. The aforementioned procedure has been widely applied in cases where a single hard phase region or materials were deformed. Its applicability in the two- phase region of materials where a softer and a harder phase generally co-exist and constantly interact is still questionable. It can arguably be pointed out that the existence of the softer phase will most likely limit the applicability of the double differentiation method in discerning whether DRX and/or DT has taken place in the warm working or two-phase region.

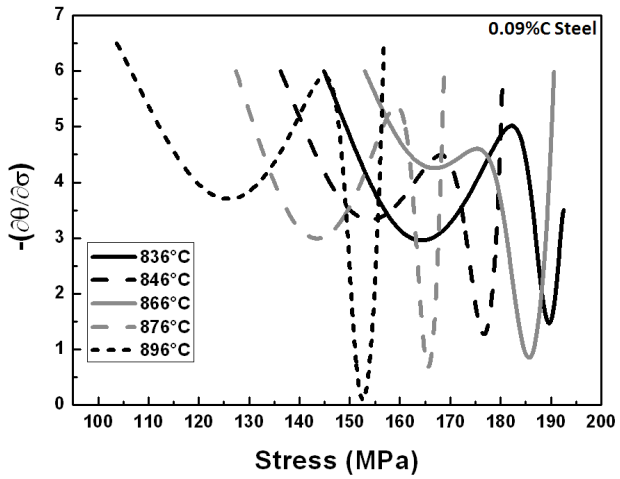

*Figure 3.22: (**∂**θ/**∂**σ) vs. σ showing double minima for DT and DRX* **[155]**.

Chapter 4

4.1 Constitutive Equations

Constitutive equations are formulations that can be fed into programs for processes such as rolling in order to achieve the desired product or for development of new products. Material behaviour during such processes is often described with reference to processing variables such as strain, strain rate and temperature. A number of constitutive equations have been well studied and developed over a number of years and in steels of different compositions. These constitutive equations are often modified or used as a basis for development of new constitutive equations for describing a particular material under study.

4.2 The Zener-Hollomon Parameter (Z)

The strain rate and deformation temperature necessary for microstructural evolution at temperatures where thermally activated deformation and restoration processes take place, are often incorporated into a single parameter [63]. This parameter, known as the Zener-Hollomon parameter, is given as [156]:

$$Z = \dot{\varepsilon}\, exp\left(\frac{Q}{RT}\right) \qquad [4\text{-}1]$$

$$\dot{\varepsilon} = AF(\sigma) \exp\left(\frac{-Q}{RT}\right) \qquad [4\text{-}2]$$

where the Z-parameter is the temperature-compensated strain rate, $\dot{\varepsilon}$ is the strain rate, A is a material constant, Q is the activation energy of deformation, T is the absolute temperature and R is the gas constant.

The Zener-Hollomon parameter can also be expressed as a hyperbolic sine function in addition to the exponent type equation as follows:

$$Z = A\,[sinh(\alpha\sigma)]^n \qquad [4\text{-}3]$$

Combining the above equations, an Arrhenius-type equation relating the Zener-parameter with flow stress is found to be as follows:

$$\sigma = \frac{1}{\alpha} ln\left\{\left(\frac{Z}{A}\right)^{1/n} + \left[\left(\frac{Z}{A}\right)^{2/n} + 1\right]^{1/2}\right\} \qquad [4\text{-}4]$$

In order to describe the flow behaviour of the investigated material using equation 4.4, the material constants α, n, Q and A in the constitutive equation need to be determined first [157]. Equations [4-1] to [4-3] can be manipulated in a number of ways to determine these material constants.

4.3 Determining the material constants

The full solution for F(σ) is given as:

$$\big(F(\sigma)\big) = \begin{cases} \sigma^n & \alpha\sigma < 0.8 \\ exp(\beta\sigma) & \sigma\sigma > 1.2 \\ [sinh(\alpha\sigma)]^n & for\ all\ \sigma \end{cases} \quad [4\text{-}5]$$

Substituting the value F(σ) for high and low stress levels in equation [4-5], gives the following relationships respectively,

$$\dot{\varepsilon} = B\sigma^n \quad [4\text{-}6]$$

$$\dot{\varepsilon} = Cexp(\beta\sigma) \quad [4\text{-}7]$$

where B and C are constants.

Considering the logarithms of both sides in equations [4-6] and [4-7], results in the following equations:

$$\ln(\sigma) = \frac{1}{\eta} ln(\dot{\varepsilon}) - \frac{1}{\eta} ln(B) \quad [4\text{-}8]$$

$$\sigma = \frac{1}{\beta} ln(\dot{\varepsilon}) - \frac{1}{\beta} ln(C) \quad [4\text{-}9]$$

From the two equations above, the values of η and β can be determined, from which the value of α can be obtained from the ratio of β over η. In most cases, it is sufficient to estimate this value as 0.012 MPa^{-1} [53], [158], [159].

Rewriting equation [4-5] so that both low and high stress levels are considered, the following equation is obtained:

$$\dot{\varepsilon} = A[sinh(\alpha\sigma)]^n\ exp\left(\frac{-Q}{RT}\right) \quad [4\text{-}10]$$

Taking the logarithm of both sides of equation [4-10], the values of the constants A, n and Q can be determined from plots using the equation [4-11]. Table 4.1 gives the values of the

constants α, A, n and Q of the 2304 DSS from other studies using different deformation modes. The variation in the values of the constants noted in Table 4.1 can be attributed to the different deformation modes, as the material mechanically behaves differently in response to different deformation modes [160].

$$ln[sinh(\alpha\sigma)] = \frac{ln\dot{\varepsilon}}{n} + \frac{Q}{(nRT)} - \frac{\ln A}{n} \qquad [4\text{-}11]$$

Table 4.1 Values for the parameters of the constitutive equation in 2304 DSS

Ref	n	α	A	Q	Deformation mode
[51]	4.2	0.0139	$7.12x10^{16}$	450	PSC
[53]	5.63	0.012	$10.0x10^{20}$	525	Torsion
[158]	2.6	0.012	$2.7x10^{10}$	263	UC

* Constants in Table 4.1 are from hot working studies in 2304 DSS. PSC stands for Plane Strain Compression and UC stands for Uni-axial compression.

4.4 Mean flow stress (MFS)

The interaction of the processes taking place during hot rolling such as recrystallization, strain-induced precipitation and strain accumulation can be best described by the mean flow stress (MFS). By so doing, experimental results can be applied to industrial applications through analysis of flow characteristics by MFS measurements [71]. The mean flow stress can be calculated through considering the area under a given stress-strain curve using the following equation:

$$MFS = \frac{1}{\varepsilon_1 - \varepsilon_0} \int_{\varepsilon_0}^{\varepsilon_1} \sigma . d\varepsilon \qquad [4\text{-}12]$$

Equation [4-12], with its relative simplicity, is basically used for the calculation of the mean flow stress in stress-strain curves from laboratory experiments. The mean flow stress in an actual rolling operation is however much more complex and cannot be generally described by equation [5-26] as indicated by the studies quoted in [26], [38].

The MFS in each pass of rolling is basically calculated using the equation developed by Sims [26]. This relationship takes into consideration the physical parameters of the work roll itself and thus the following need to be known strip width, thickness, work roll diameter and rolling force in order to get:

$$MFS = \frac{P}{\left(\frac{2}{\sqrt{3}} w[R(H-h)]^{1/2} Q\right)} \qquad [4\text{-}13]$$

where P is the roll force, R is the roll radius, W is the strip width, H is the entry thickness, h is the exit thickness, and Q is the geometrical factor.

Although a significant amount of work has been done in 2304 DSS [7], [51], [158] and other closely related duplex steels such as 2101 DSS [161] and 2205 DSS [8], [68], [162], [119], it can still be appreciated that the full understanding of the hot working behaviour of these steels still remains limited. Most work on the flow behaviour of duplex stainless steels is limited to the use of constitutive equations with no knowledge of how the microstructure, amount of dynamic softening, recrystallization and volume fraction during deformation vary with processing parameters. In all of the above studies, the volume fraction of the second phase (austenite) was observed or considered to be constant with variation of processing parameters, except for temperature. Thus, the change in volume fraction of phases in duplex stainless steels has been always considered to be invariant at a given temperature [7], [158], [162]. For optimization of hot working in duplex stainless to be achieved, further work has to be carried out to investigate the interaction between processes within the material and the hot rolling parameters, especially in 2304 DSS, where there is substantially limited knowledge.

4.5 The Hot Working Window

This is a processing window that is crucial in achieving the outcomes of the desired thermomechanical process without flow instabilities. Flow instabilities compromise the mechanical and microstructural integrity of the material being hot worked. These flow instabilities usually manifest themselves microstructurally in the form of flow localization, adiabatic shear band formation, mechanical twinning, and kinking or flow rotations. In any case, they are an indication that the specific flow localization parameter of the material being hot deformed, has been exceeded. Typically as a result of these microstructural instabilities and deformation adiabatic heating, flow softening does take place during hot working, and this can easily be interpreted to be from dynamic recrystallization. To operate within the

limits of thermo-mechanical processing where flow localization and hence flow instability does not occur, the hot working window needs to be defined. This can be done through processing maps of the material based on a dynamic material model (DMM) following the extensive work by Prasad and Seshacharyulu [163].

In the dynamic material model, a work piece undergoing hot deformation is considered to be a power dissipator. The power absorbed P by the material during plastic deformation is dissipated through two complementary processes: viscoplastic heat or temperature rising (G part) and microstructural changes (J part), expressed mathematically as [163]:

$$P = J + G = \sigma\dot{\varepsilon} = \int_0^{\sigma} \dot{\varepsilon} d\sigma + \int_0^{\dot{\varepsilon}} \sigma \, d\dot{\varepsilon} \qquad [4\text{-}14]$$

The efficiency η of this power dissipation process is calculated at a constant strain as follows:

$$\eta = \frac{J}{J_{max}} = \frac{2m}{m+1} \qquad [4\text{-}15]$$

where *m* is the strain rate sensitivity of the material and m = 1, where $J = J_{max} = \sigma\dot{\varepsilon}/2 = p/2$, for an ideal linear dissipater. The strain rate sensitivity is calculated from the usual equation:

$$m = \frac{\partial \, ln\sigma}{\partial \, ln\dot{\varepsilon}}\Big|_{\varepsilon,T} \approx \frac{\Delta \, log\sigma}{\Delta \, log\dot{\varepsilon}}\Big|_{\varepsilon,T} \qquad [4\text{-}16]$$

where the terms *σ, ε,* and *T* and *s* represents stress, strain and absolute temperature, respectively. The power dissipation map is constructed from the variation of efficiency η with the processing parameters of temperature and strain rate.

While the power dissipation map shows the specific microstructure formation mechanism, another mechanism of importance during hot working is microstructure instability, i.e. the region where this takes place also needs to be defined. Microstructure instability takes place when flow instability is negative, and this flow instability is given by the following equation [164]:

$$\xi = \frac{2m}{\eta} - 1 \; < 0 \qquad [4\text{-}17]$$

A negative ξ ($\dot{\varepsilon}$) represents flow instability and its variation with temperature and strain rate constitutes an instability map. Superimposing an instability map with the power dissipation

map, results in the construction of a processing map from which the processing parameters during the hot working process can be optimized [165], [166].

Chapter 5

5.1 Experimental Procedure

The steel that was investigated in this study was 2304 Lean Duplex stainless steel (LDSS) supplied by Columbus Stainless South Africa in the form of a transfer bar from the roughing mill. The chemical composition of the steel is given in Table 6.1. In order to investigate the hot working behaviour (phase and microstructure evolution) of 2304 DSS and the influence of process parameters in-plant, a series of uni-axial compression tests were carried in the laboratory. The tests were carried out in both the Bähr 850D® Dilatometer and the two Gleeble 1500^{TM} and 3800^{TM} thermomechanical processing simulators.

Table 5.1: Chemical composition of 2304 LDSS (mass %)

C	**Mn**	**Si**	**Nb**	**Ti**	**V**	**Cr**	**Mo**	**Ni**	**Cu**	**N**	**S (ppm)**	**Fe**
0.016	1.22	0.58	0.01	0.03	0.13	22.39	0.37	3.70	0.17	0.12	30	Bal.

The microstructure of the as-received material is shown in Figure 6.1. From the microstructure, it can be perceived that austenite (light phase) is elongated along the rolling direction. Though not perfectly homogeneous, the distribution of austenite within the ferrite (dark phase) can be considered approximately uniform. Attaining a perfectly homogeneous distribution and desired shape of the second phase, can be achieved by rigorous heat treatment and thermomechanical processing (TMP) procedures as indicated in a study by Martin [7]. To ensure that a homogeneous microstructure and phase stability were achieved in the sample at the target deformation temperature, the sample was held at temperature for 600 -1200 s before deformation. This holding time was confirmed in the preliminary tests where samples were heated to the same temperature at the same reheating rate and held for different varying times ranging from 300 3600 s. No phase fraction changes were observed in this case. The samples deformed and quenched from the same temperature after being held for 600 s and 1200 s, showed no variation in phase fraction. This gave an indication there was phase stability before deformation.

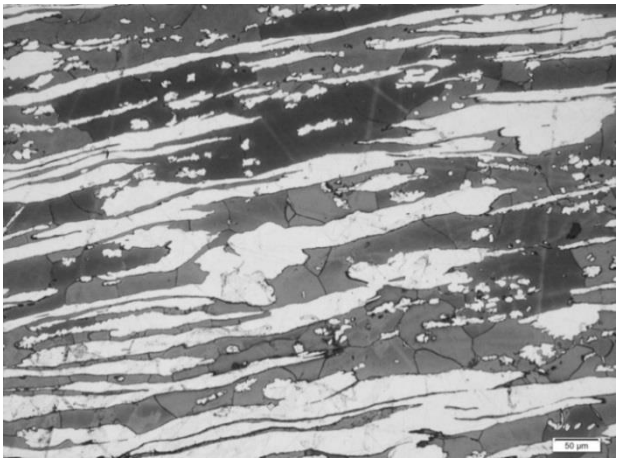

Figure 5.1: The microstructure of the as-received 2304 LDSS transfer bar showing ferrite and austenite (the light phase) elongated along the rolling direction.

5.2 Hot Compression Tests

The simulated process parameters were obtained from the Steckel hot rolling mill data log (as indicated in Appendix 6) and these are temperature, strain per pass, strain rate and inter-pass time. It is imperative to investigate the effects of each of these parameters on the evolution of the microstructure, phase balance and ultimately flow behaviour in ordr to optimize the processing of this duplex stainless steel. Although the highest temperature in the roughing mill before the steel goes into the steckel is around 1100 ^{o}C, the reheat temperature before the rougher will be even higher, thus in this study it was chosen to be 1200 ^{o}C, for homogenization of the material. A study [167] on the comparison of plain stress through which axial symmetric compression takes place (as in the current study) versus the plain strain condition which is typical of in-plant rolling showed comparable mean flow stress and Q values. The major exception was in the texture evolution. Since, the main focus of this study was not on texture analysis, axisymmetric compression was used. Single-hit compression tests were carried out using both the Bȁhr 850D^{TM} Dilatometer and the Gleeble 1500^{TM} as well 3800^{TM} (for the two Gleeble machines, at lower and higher strain rates, respectively).

5.2.1 Single-hit uniaxial compression test in the Bȁhr dilatometer

The specimens were machined into cylinders of 5 mm diameter and 10 mm length along the rolling direction of the transfer bar. Deformations were done in the temperature range of 850 to 1050 ^{o}C and the strain rates were varied as follows: 0.1, 1, 5, 10 and 15 s^{-1}.

After deformation, each specimen was immediately quenched at 600 ^{o}C/s using Helium, so as to retain the hot worked microstructure at room temperature. Single-hit tests were carried out to investigate the effects of dynamic conditions (temperature, strain rate, strain) in a pass on the evolution of the microstructures and their phase balance. The specimens were also held at deformation temperatures for varying times after deformation in order to investigate the effects of the inter-pass time. The test conditions used are summarized in a schematic diagram in Table 5.2 and Figure 5.2.

Table 5.2: Test parameters for single pass deformation tests in the Bähr 850D^{TM} Dilatometer

Parameters	Values
Reheating rate	10 ^{o}Cs^{-1}
Soaking temperature	1200 ^{o}C
Soaking time	300 s
Cooling rate to deformation temperature	10 ^{o}Cs^{-1}
Holding time before deformation	1200 s
Deformation temperature range	850 – 1050 ^{o}C
Total applied strain per pass	0.6, 0.8
Strain rate range	0.1, 1, 5, 10, 15 s^{-1}

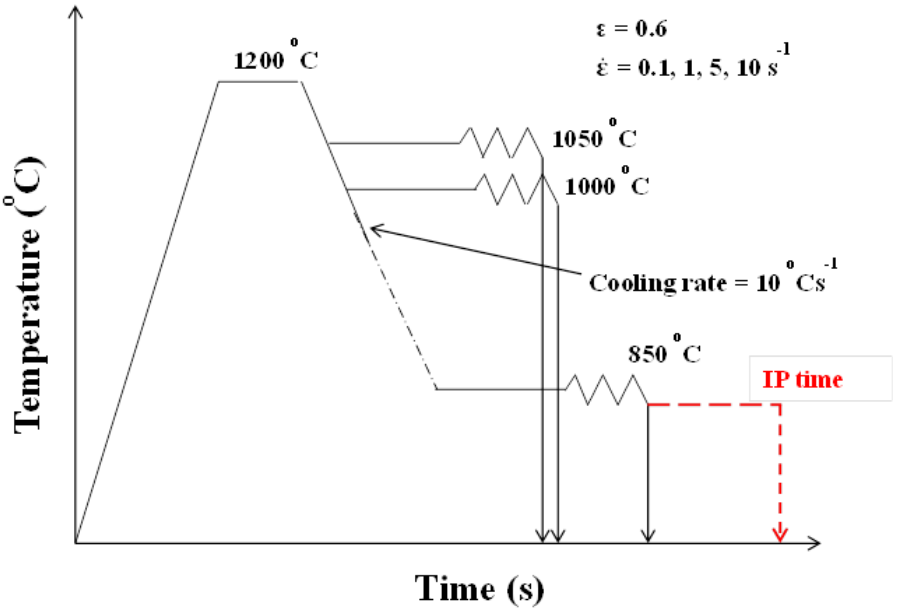

Figure 5.2: Schematic diagram for the single-hit uniaxial compression tests in the Bähr dilatometer.

The Gleeble 3800™ machine was used to investigate the effects of typical industrial strain rates and two strain rates were chosen, i.e. 30 and 50 s^{-1}. The total true strain was limited to 0.8 in order to avoid excessive barrelling. No inter-pass time effects were investigated at these higher strain rates but only the effects of strain rate and temperature were varied at the two respective strain rates. After deformation the samples were also quenched to retain the deformed microstructure at room temperature. The test schedule for single-pass deformation using the Gleeble 3800™ is shown in Figure 5.3.

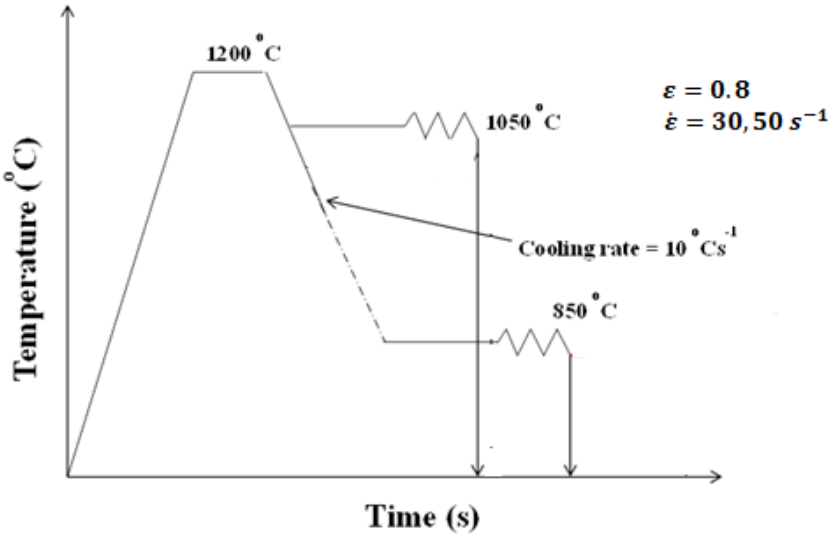

Figure 5.3: Schematic diagram for the single-hit uniaxial compression tests in the Gleeble 3800™.

5.2.2 Multi-pass uniaxial compression tests

Specimens were machined to the same dimensions as mentioned above. The multi-pass tests in the Gleeble 3800™ machine were mainly carried out to investigate whether strain accumulation could take place during multi-pass deformation of the 2304 LDSS. It was of interest to investigate whether strain accumulation takes place leading to build-up of stored energy from deformation and hence the possibility of higher driving forces for both dynamic recrystallization and dynamic ferrite-austenite phase transformation. Three deformation passes were carried out at strain rates of 10 and 30 s^{-1}; at two different temperatures of 850 and 1050 ^{o}C. These specimens were first heated to a soaking temperature of 1200^{o}C at 10 $^{o}Cs^{-1}$ and held for 300 s to ensure a homogeneous temperature distribution throughout the specimen. The specimens were then cooled at the same rate as the heating rate to deformation temperatures where they were again held for 1200 s to ensure an equilibrium condition of the

microstructures before deformation was carried out. The strains of the first two passes were 0.2 each and 0.4 for the last pass, giving a total strain of 0.8, see Table 5.3.

Table 5.3: Test parameters for multi-pass deformation tests in the Gleeble 3800^{TM}

Temp (^{o}C)	**Strain rate (s^{-1})**	**Strain**			
		P1	P2	P3	ε_{total}
850	10	0.2	0.2	0.4	0.8
850	30	0.2	0.2	0.4	0.8
1050	10	0.2	0.2	0.4	0.8
1050	30	0.2	0.2	0.4	0.8

Special care was taken when carrying out deformation tests in the Gleeble to reduce barrelling and friction between anvils and specimen. In the Gleeble the specimen was deformed between two anvils and isothermal conditions were necessary to ensure uniform temperature throughout the specimen. Tantalum foil was placed between the Tungsten Carbide anvils and the specimen to reduce friction and sticking. The anvil-specimen setup in the Gleeble is shown in Figure 5.4.

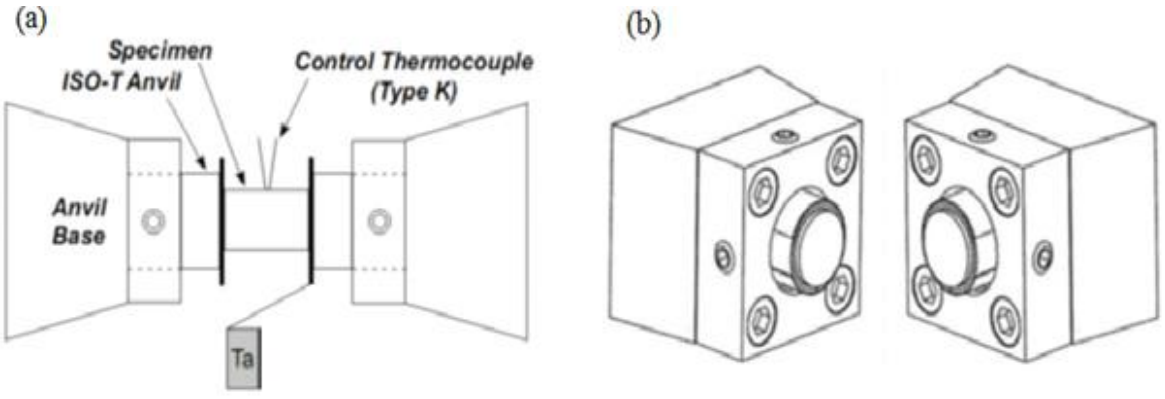

Figure 5.4: Schematic diagram for the isothermal compression test (a) arrangement [168], *(b) fixture* [169].

5.3 Microstructural Analysis

After isothermal compression testing, the specimens were cut under water along the deformation axis for microstructural analyses, see Figure 5.5. The specimens were then

ground using silicon carbide abrasive paper to 1200 grit size. Polishing to 3 μm diamond suspension proved sufficient to obtain good microstructures, however further polishing to 1 μm gave an even better polishing finish for optical microscopy. To be able to view the microstructures under the optical microscopy, a Beraha chemical selective etchant was used. This etchant is made up of 100mL H_2O, 30mL HCl and 1-1.5g $K_2S_2O_5$. The austenite volume fraction measurements were carried out using the point count method at a confidence interval estimate of 95%, according to ASTM Standard E562-83 [170].

Samples for electron backscatter diffraction (EBSD) analysis were further polished using colloidal silica after the 1 μm diamond suspension. A Joel Oxford Tungsten Filament scanning electron microscope (SEM) equipped with a fully automatic HKL technology EBSD attachment and operated at 20 kV with an electron beam size of 7 nA was used for EBSD studies. The specimen was tilted to 70 ^{o} with respect to the electron beam towards the EBSD detector. The use of 9 Kikuchi bands to analyse the diffraction patterns enabled the face centred cubic (fcc) austenitic to be clearly distinguished from the body centred cubic (bcc) ferrite [171]. Two step sizes of 2 and 0.5 μm were generally used; the coarse step size being for an area map of typically 0.55 mm^2 and the fine step size for an area map of 0.25 μm^2. Information about the grain structure, and the crystallographic texture was obtained from large area maps while substructure characteristics were derived from detailed orientation maps using a fine step size. The HKL Channel 5 software was used for both data acquisition and post-processing.

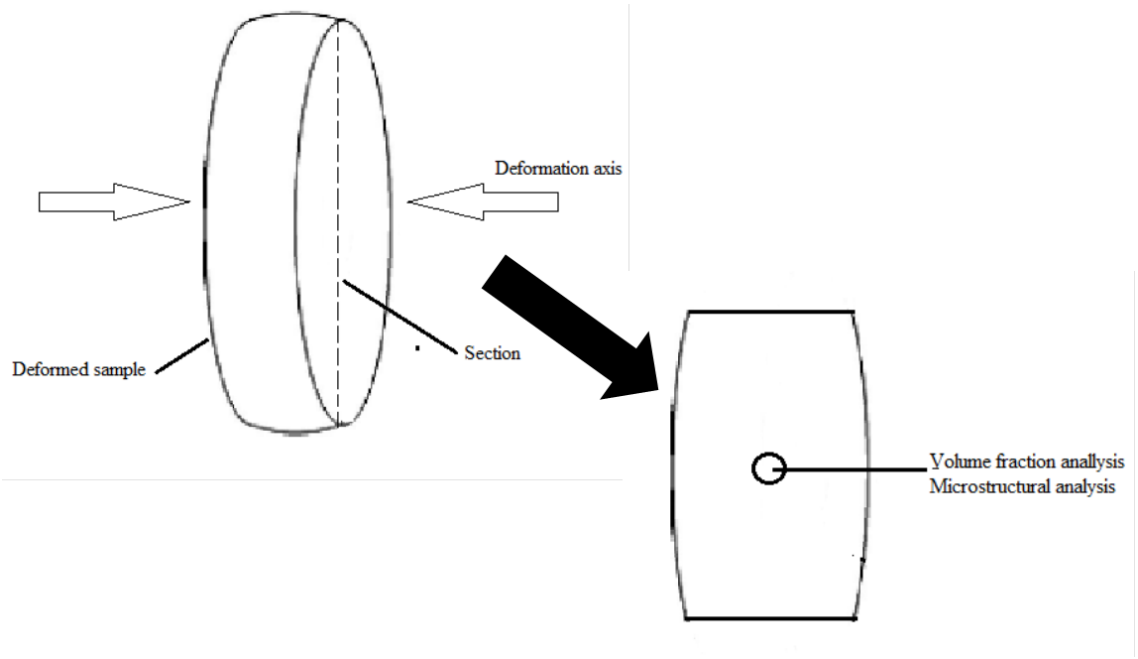

Figure 5.5: Schematic diagram showing location where austenite volume fraction and microstructure analysis were carried out after deformation.

5.4 Phase prediction

Thermo-Calc Computer Software's database was used to determine the volume fraction of austenite as a function of temperature. In studies [172] and [173], Thermo-Calc computer software was used to construct the equilibrium diagram and the phase fraction diagram for the steel under study. These diagrams were then used to find the inter-critical annealing temperatures and austenite phase fractions at various temperatures. In another study [174], Thermo-Calc was used to determine the A_{c1} and A_{c3} temperatures of a dual phase martensitic-ferritic dual phase steel. In the current study, the phases present at each temperature were predicted under equilibrium conditions as a guideline knowing that non-equilibrium conditions prevail during the hot rolling process. Figure 5.5 shows the results from those Thermo-Calc predictions. From these predictions the volume fraction of austenite was seen to increase with a decrease in temperature down to 850 ^{o}C where a maximum volume fraction of austenite was found to be approximately 43 %. At a temperature of 1200 ^{o}C, the predictions show no presence of austenite but only a 100 % ferrite phase fraction.

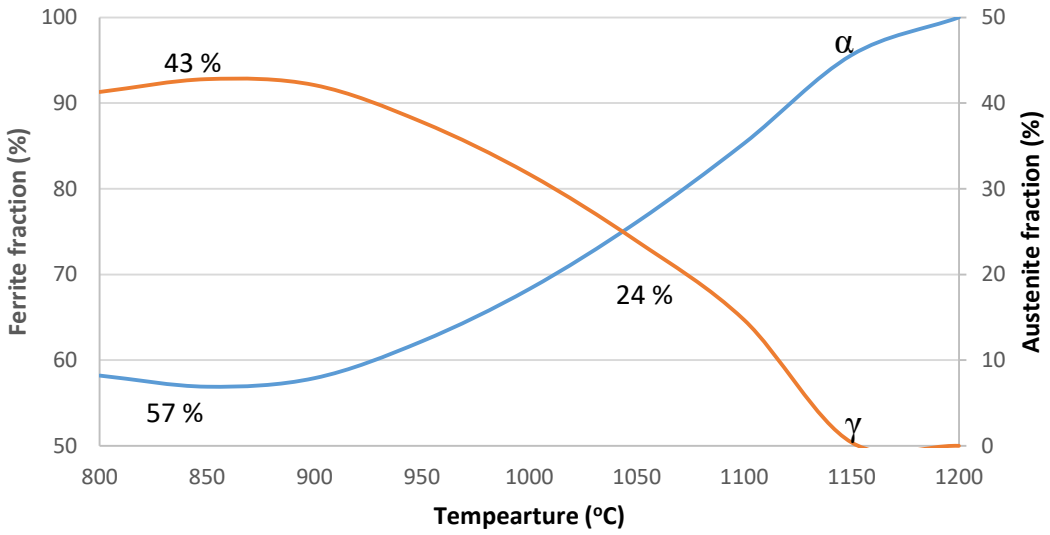

Figure 5.6: Thermo-Calc predictions of phase fractions as a function of temperature.

Chapter 6

6.1 Experimental Results

This chapter presents the experimental results obtained from both the single-hit and multipass isothermal deformation tests done in this sudy. Analysis of the flow stress behaviour and the microstructures was done in order to determine the effect of process parameters on the phase balance and microstructural evolution of the material and hence the overall effect on the hot working behaviour. Microstructural analysis was carried out using both optical microscopy and scanning electron microscopy. Since the aim of the work was to quantify the effect of these parameters in an industrial plant situation, the required information needed was obtained from the plant mill logs. This then enabled the experimental results obtained to be used for optimization of the rolling process in the plant, i.e. in terms of mill loads and torque to be used. The highlights of the results thus focuses on the following:

a. Effect of strain rate on the flow stress, microstructure evolution, phase ratio, and softening behaviour. A substantial amount of work was done in order to determine the mechanism or process responsible for the observed softening (decrease in flow stress). Analysis of the the true stress against temperature plots revealed that adiabatic heating during deformation was not present since the temperature increase hardly reached 5 ^{o}C.
b. Effect of temperature on the flow stress, microstructure evolution, phase ratio, and softening behaviour.
c. Effect of strain on the flow stress, microstructure evolution, phase ratio and softening behaviour.
d. Effect of strain accumulation on the flow stress, microstructure evolution, and phase ratio, softening behaviour. Short interpass times were used in this instance to allow strain from the previous pass to be carried over into the next.
e. Effect of interpass time on the flow stress, microstructure evolution, phase ratio and softening behaviour. In this instance, the deformed specimen was held at temperature for a time equivalent of a typical interpass time before being quenched.

The results from the above tests were then compiled in order to formulate a model for the hot working bevaiour of 2304 LDSS. The model was then modified to suit industrial hot rolling conditions.

6.2 Flow stress analysis

6.2.1 Single hit Bȁhr Dilatometer tests

All flow curves showed an increase in peak stress with increase in strain rate and decrease in temperature when temperature and strain rate were kept constant in each test, respectively. As may be seen in Figure 6.1, the flow curves showed that the material work hardens to a peak stress which thereafter continuously declines without attaining steady state. This was the general behaviour for all deformation temperatures for strain rates of 0.1 to 15 s^{-1} and strains of up to 0.6. At any given tempertaure, the peak stress or flow stress was observed to increase with strain rate. Increasing strain rate results in more dislocations being generated in the material, hence more tangled dislocation structures would be expected with an increase in strain rate. In turn these dislocation tangles will impede dislocation movement, resulting in more work hardening in the material, *i.e.* increased resistance to deformation.

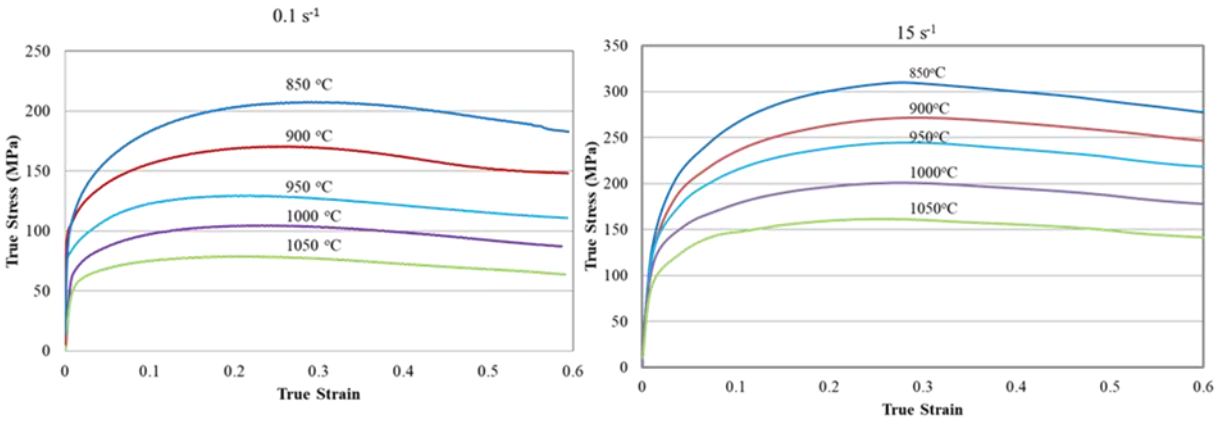

Figure 6.1: True stress-true strain curves for 2304 DSS for constant strain rate but varying deformation temperatures.

Figure 6.2 shows the variation of flow stress with strain rate in two different processing temperature regimes, *i.e.* 850 ^{o}C (low temperature) and 1050 ^{o}C (high temperature). The flow curves show an increase in flow stress with strain rate for both temperatures, though higher stresses were clearly attained when the deformation was carried out in the lower temperature regime. Foremost, this could be a result of stresses needed for dislocation breakaway from pinning points being higher at lower temperatures when compared to higher temperatures. Secondly, thermally activated restoration mechanisms such as slip and climb become more prominent with an increase in temperature.

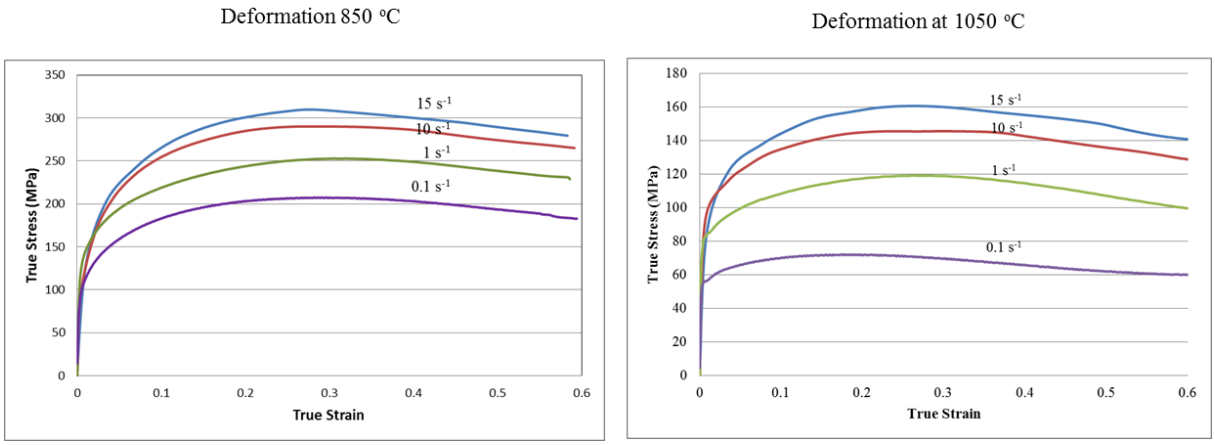

Figure 6.2: True stress-true strain curves for 2304 DSS for constant deformation temperatures but varying strain rates.

The obtained flow curves show a peak followed by continuous softening. This flow behaviour is persistent in all flow curves at all temperatures and strain rates studied except at a strain rate of 0.1 s^{-1} and temperature of 1050 ^{o}C. At this strain rate and temperature, the flow curve shows an early attainment of steady state. In alloys with a low to medium stacking fault energy, the presence of a peak followed by softening is an indication that the material has undergone DRX through migration of high angle boundaries. Under normal circumstances, the attainment of a steady state can be an indication that at 1050 ^{o}C and 0.1 s^{-1} strain rate, the time was long enough for complete recrystallization to take place. The high temperature (1050 ^{o}C) also made the condition ideal, since DRX is a thermally activated process and hence effective lowering of the deformation energy of the system through formation of new dislocation free grains. The typical steady state flow behaviour at 1050 ^{o}C and 0.1 s^{-1}, shows that this deformation condition allowed a dynamic balance between the nucleation of new grains and the migration of the boundaries of the previously nucleated grains to be attained. Continuous softening at all the other deformation temperatures is an indicator that the above condition of balance between nucleation of new grains and migration of boundaries has not been met [63]. While continuous softening was observed after deformation was carried out to a strain of 0.6 (Figures 6.1 and 6.2), steady state was observed with further straining to 0.8 strain (Figure 6.3). The steady state flow stress was determined or estimated to be achieved at strain of 0.7 for deformation at strain rate of 15 s^{-1}.

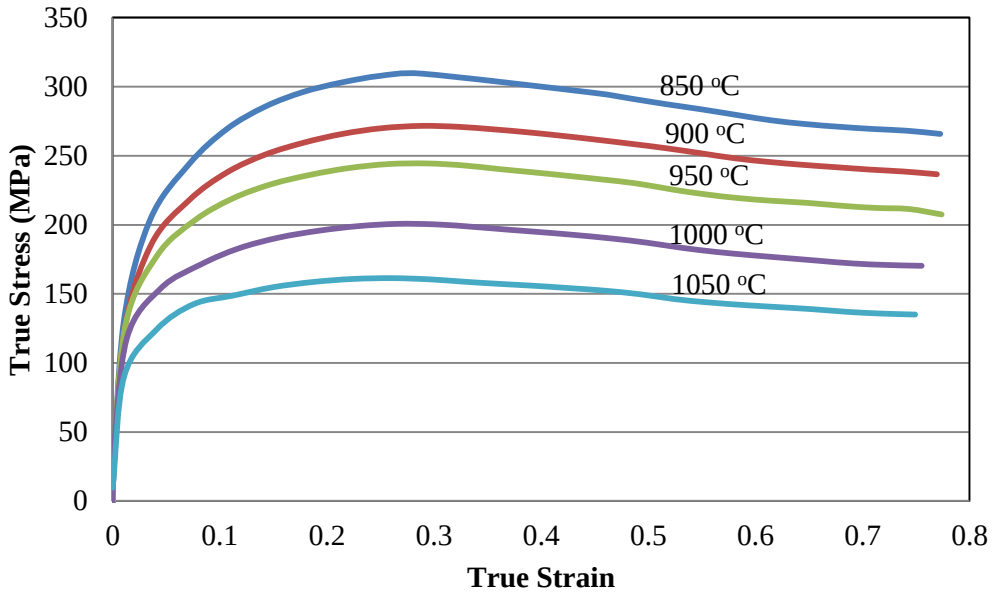

Figure 6.3: True stress-true strain curves obtained at a strain rate of 15 s^{-1}.

In a two phase material, the temperature determines the fraction of each phase present and the strain rate which phase is likely to bear greater deformation. Flow softening has also been attributed to dynamic transformation. DRX and DT are therefore competing processes. Both processes require a critical strain to be achieved for either process to take place [112]. The critical strain for initiation of DT is lower than that for DRX. The presence of DT in general, is confirmed by the presence of a second peak in the plot of the second order derivative of the flow curve for a single phase material [155]**.** The existence of two phases in a dual phase steel is most likely to obliterate the appearance of an inflection point associated with dynamic transformation. In the current study, only one inflection point was observed and this was attributed to DRX, since flow softening was observed both in the absence and presence of DT as confirmed by microstructural analysis, see Figure 6.4.

Figure 6.4 also shows the classical Kocks-Mecking approach [152] to analyse the work hardening behaviour of the material, see the dotted in Figure 6.4 (a). The analysis is based on the competition between storage and annihilation of dislocations through DRV. Generally, the work hardening rate decreases with stress under all deformation conditions. Since work hardening is countered by DRV, the work hardening rate was observed to decrease with decreasing strain rate and increase in temperature as higher deformation temperatures and lower strain rates promote DRV. The plots show that decrease in the work hardening rate with stress is not exactly linear as might be expected but undulates. The undulation could be a

result of variation in the work hardening rate in the two phases with more deformation (stress) as the strain accommodation by each phase also varies with strain. At a higher strain rate (10 s^{-1}), the region becomes more linear suggesting that there is a single recovery rate, hence deformation is more localized or accommodated by one phase. The dotted line in Figure 6.4 (a) shows how the initial work hardening rate θ_0 and the saturation stress σ_{sat} for all deformation conditions were determined through fitting linear equations in the latter stage of work hardening.

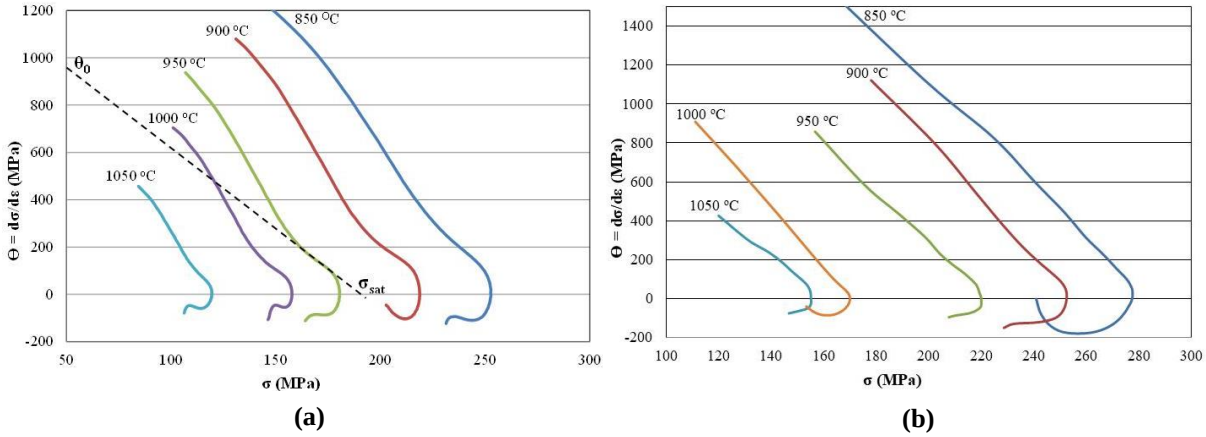

Figure 6.4: Stress dependence of the work-hardening rate at different temperatures: (a) 1 s^{-1} and (b) 10 s^{-1}.

Complete DRX and attainment of a steady-state was only observed at 850 ^{o}C with strain rates of 10 s^{-1} and 15 s^{-1}. All the other flow curves indicate that DRX was initiated but incomplete and the work hardening rate can be extrapolated to a hypothetical saturation σ_{sat}, where softening can be attributed to DRV alone and the work hardening rate is zero, as shown in Figure 6.4a. Thus σ_{sat} corresponds to the saturation stress where there is no additional softening due to DRX [80]. The drop in the work hardening rate below zero thus indicates the occurrence of DRX. The initial athermal work hardening rate θ_o is found from the linear extrapolation of the initial range of the work hardening rate – stress curves to where the stress is zero.

6.2.2 Multipass deformation tests

The flow stress results presented so far were from single pass deformations in the Bahr dilatometer. Though the multipass deformations performed in this study did not have exact parameters as those used in the plant, they gave an appropximation of what can be expected from the multipass rollling conditions in the plant. Interpass times of 20 s were used.

Comparing the flow curve from the single pass deformation at 850 ^{o}C and a strain rate of 10 s^{-1} to that of multipass deformation at the similar conditions (Figure 6.5(a)), shows that the flow softening that is observed after the peak strain in single pass deformation, is absent in multipass deformation. Instead, strain accumulation was observed with each subsequent deformation, Figure 6.5(a). Some form of flow softening is however observed in the strain range of 0.5 to 0.6, possibly from DRX after sufficient driving force for the DRX has been attained. In Figure 6.5(a), the single pass deformation was carried out in the Bähr-dilatometer while the multipass deformation was carried out in the Gleeble, hence the difference in peak flow stresses due to differences in sample size. The austenite volume fraction was noted to be the same for single and multipass deformation (Appendix 3). At a higher strain rate of 30 s^{-1}, strain accumulation was observed with the subsequent passes with no characteristic softening as shown in Figure 6.5 (b). Comparison of the single pass versus mutlipass deformation at a strain rate of 30 s^{-1}, shows that a multipass deformation at higher rates results in a stress increment $\Delta\sigma$. This could be attributed to the DRV during the interpass time that leads to some loss in driving force for subsequent DRX.

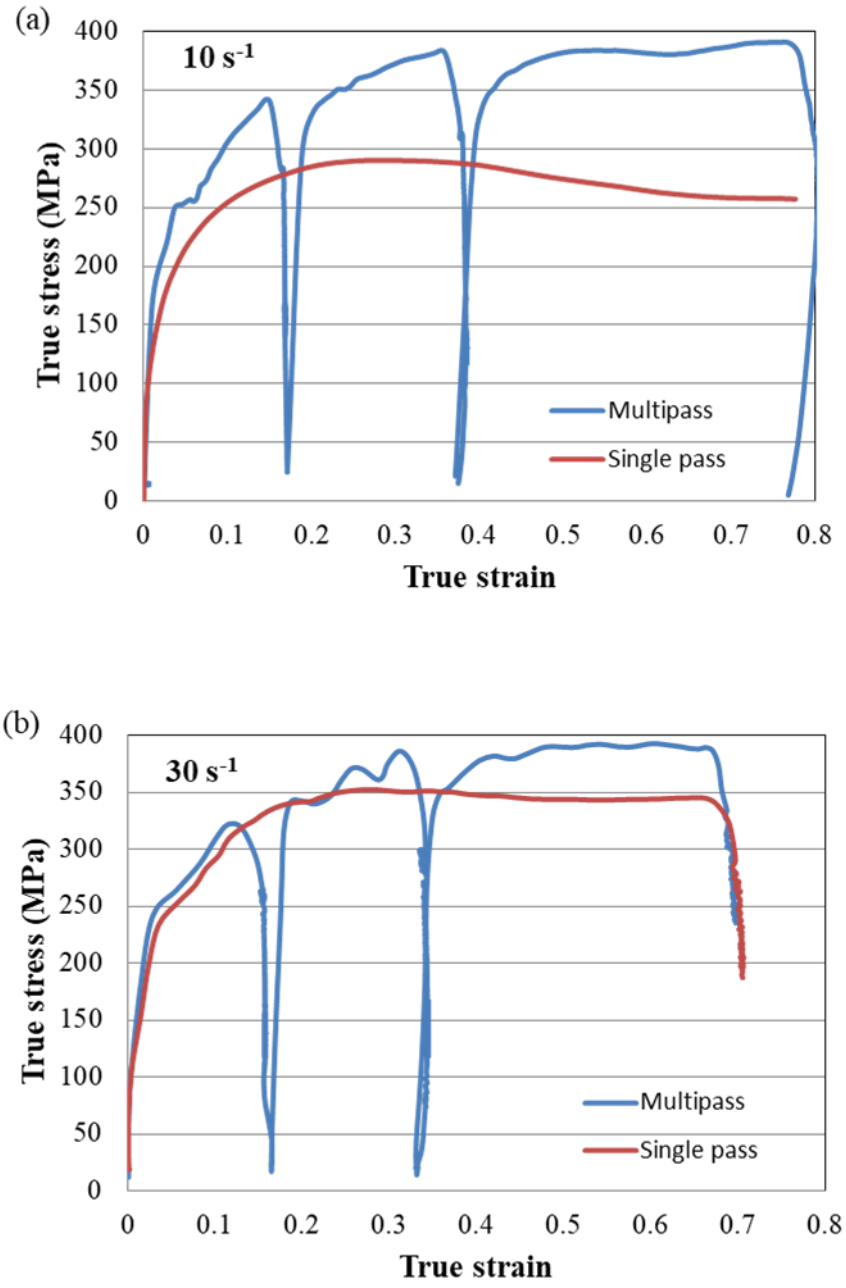

Figure 6.5: Comparison of single versus multipass deformations at 850 ^{o}C at (a) 10 s^{-1} (b) 30 s^{-1}.

6.3.1 Phase fraction measurements

Figure 6.6 shows the volume fractions of the two austenite phase fractions present after being homogenized at 1200 ^{o}C and annealed at temperatures of 850 ^{o}C and 1050 ^{o}C, i.e. 39 and 33% respectively, which define the extreme temperatures for the hot working window. The austenite volume fraction is known to increase with a decrease in temperature, and it is confirmed here that the austenite volume fraction does indeed decrease with temperature. The change in volume fraction is not very significant considering that the increase in volume

fraction is only about 6 % for a temperature drop of 200 ^{o}C. The values differ significantly from those predicted at equilibrium from Thermo-Calc, which suggests an increase of close to 20 %, i.e. an increase in austenite volume fraction from 24 to 44% between 1050 and 850 ^{o}C respectively. This could be due to phase fraction values predicted through Thermo-Calc being based on equilibrium heating and cooling conditions while during the actual experiments, heating and cooling rates are much higher than equilibrium rates. This then makes the holding time at a given annealing temperature crucial, which the software does not take into consideration [175]. In Thermo-Calc, the effects of solute drag on the transformation kinetics and moving boundaries or interfaces are also not considered. The effect of solute drag on moving grain boundaries and phase interfaces can have significant effects on phase transformations as shown in the following studies [176], [177], [178], [179], [180].

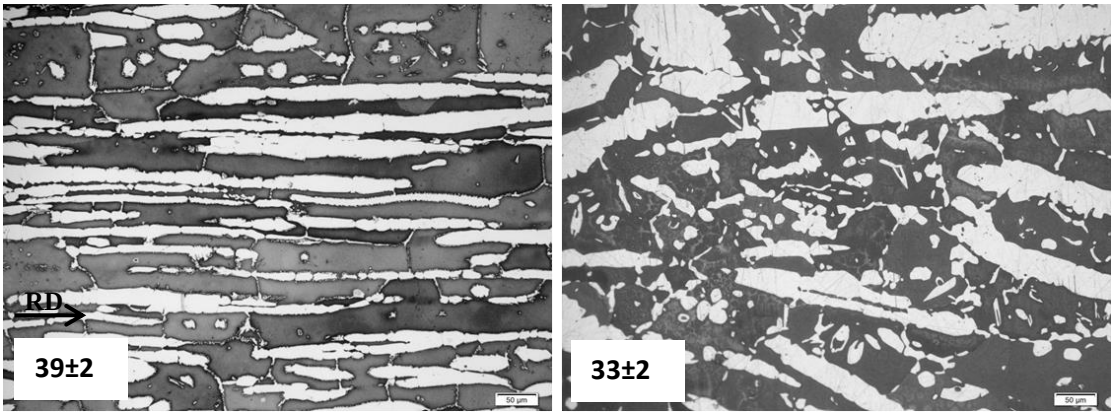

(a) (b)

Figure 6.6: The microstructure of the undeformed 2304 DSS annealed at: (a) 850^{o}C (b) 1050 ^{o}C after 1200 s hold at temperature and quench.

Microstructural analyses after high temperature deformation showed an increase in the volume fraction of austenite with strain rate. In Figure 6.7, the volume fraction of austenite at a temperature of 850 ^{o}C, strain rates of 0.1, 1, 5 and 10 s^{-1} were found to be 30 %, 30 %, 42 % and 49 %, respectively. The two temperatures of greater interest were 850 and 1050 ^{o}C and the volume fractions measured at these temperatures for strain rates 0.1, 1, 5 and 10 are shown in Table 6.1. The observations were for deformations to a total strain of 0.6.

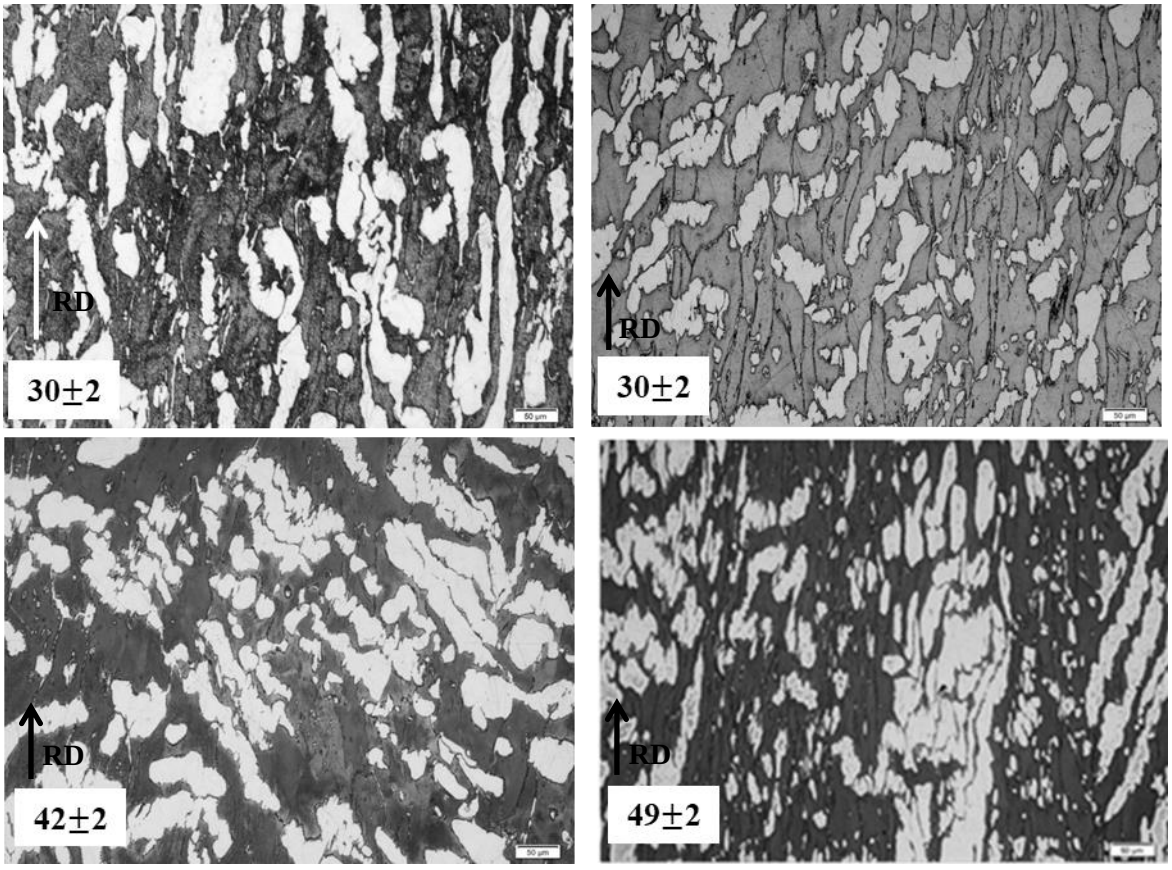

Figure 6.7: Variation of austenite volume fraction at 850 ^{o}C with strain rate (a) 0.1 s^{-1} (b) 1 s^{-1} (c) 5 s^{-1} (d) 10 s^{-1}.

Table 6.1: Variation of austenite volume fraction without deformation ($V_{\gamma E}$) and with deformation ($V_{\gamma D}$), peak stress and MFS with strain rate.

T (^oC)	$V_{\gamma E}$ (%)	$\dot{\varepsilon}$ (s^{-1})	$V_{\gamma D}$ (%)	σ_p (MPa)	MFS (MPa)
850	39 ± 2	0.1	30 ± 2	207	191
	39 ± 2	1	30 ± 2	253	233
	39 ± 2	5	42 ± 2	277	256
	39 ± 2	10	49 ± 2	290	277
1050	33 ± 2	0.1	28 ± 2	80	72
	33 ± 2	1	32 ± 2	120	111
	33 ± 2	5	37 ± 2	154	143
	33 ± 2	10	39 ± 2	154	152

Increasing the strain further beyond 0.6 to 0.8 had no effect on the volume fraction of austenite. Likewise, increasing the strain rate beyond 10 s^{-1} showed no significant effect on the volume fraction of austenite. At 850 ^oC, no volume changes were observed as the strain rate was increased from 0.1 to 1 s^{-1}, indicating insufficient driving force for dynamic transformation. Increasing the strain rate from 1 to 5 s^{-1} was accompanied by an increase in the austenite volume fraction from 39% to 42%, showing that an increase in the driving force had prompted dynamic transformation. An increase of strain rate from 5 to 10 s^{-1} resulted in a further increase in the austenite volume fraction. Deformation at a strain rate of 10 s^{-1} resulted in an increase of 10 % in volume fraction of the austenite when compared to the volume fraction of austenite in an undeformed sample at the same temperature. Similar results to those at 850 ^oC were observed at 1050 ^oC. Further analysis also showed that the strain within a compression test had an effect on the driving force for DT, as shown in Figure 6.8. Increasing the strain from 0 to peak strain (ε_p) had no influence on the volume fraction. However, increasing the strain beyond the peak strain resulted in an increase in the austenite

volume fraction. No phase change (DT) before the peak can be attributed to insufficient stored energy necessary for DRX in austenite which results in a difference in dislocation density between austenite and ferrite, hence the driving force for DT to take place. In this strain range the austenite islands are still aligned perpendicular to the rolling direction. An increase in austenite phase fraction was only observed with an increase in strain after the peak strain, as shown by microstructural analysis in Figure 6.9. At the same time softening is observed in this strain range as a result of DRX (Figure 6.8) and the austenite becomes aligned in the rolling direction. The initiation of DRX in austenite while ferrite is undergoing DRV or a possible increase in the dislocation density, both which maintains a higher dislocation density than in austenite, is likely to be the reason why DT takes place. This causes a strain induced boundary migration of austenite into ferrite which is contrary to DIFT where dynamic transformation is usually initiated before DRX takes place. Thus, according to the observations, no volume fraction changes are expected before the initiation of DRX.

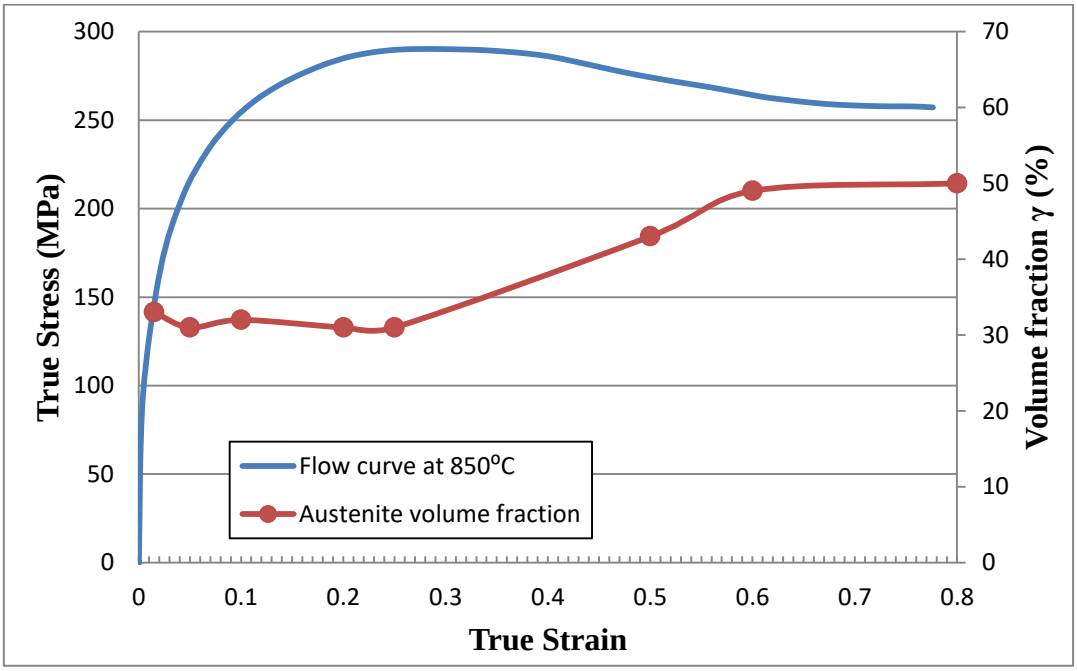

Figure 6.8: Variation of stress and austenite volume fraction with strain at 850 ^{o}C and 10 s^{-1}.

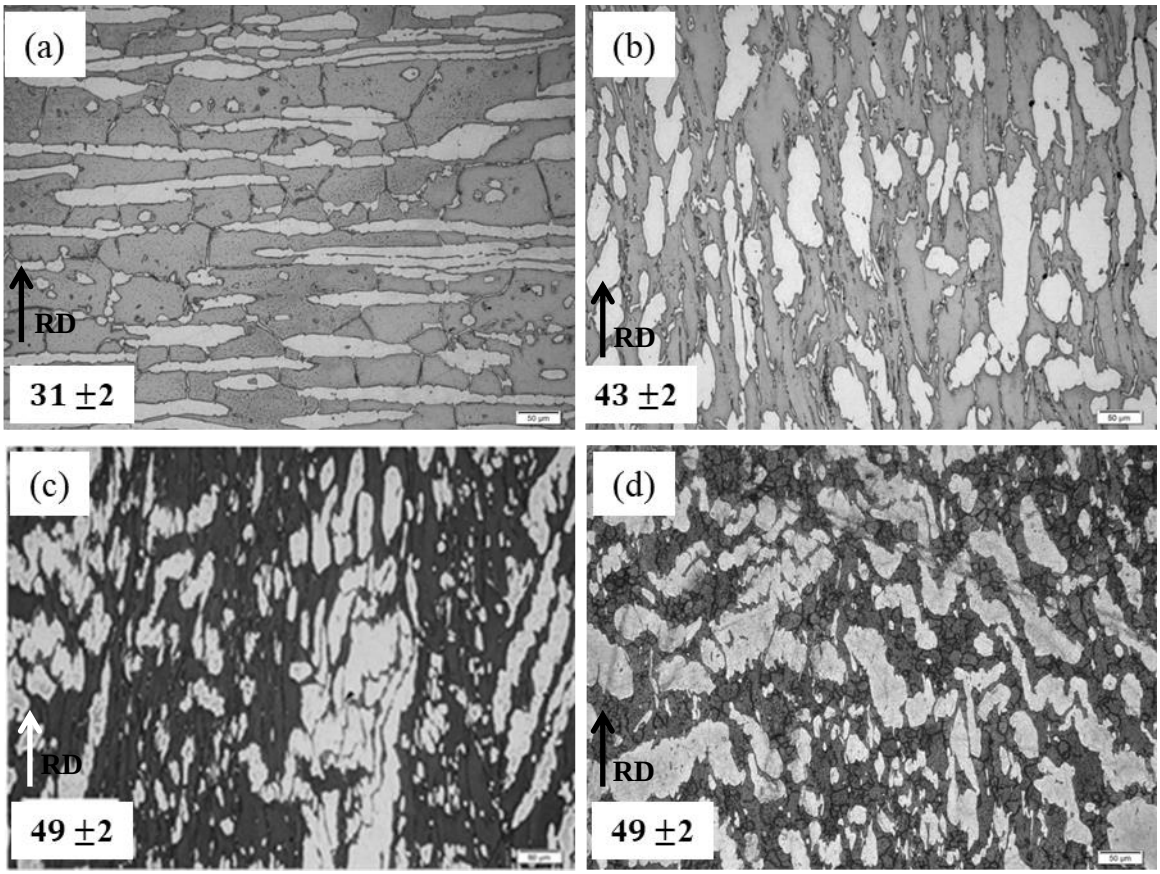

Figure 6.9: Microstructural analysis showing the effect of strain on the austenite volume fraction: (a) 0.25 (typical 0- ε_p) (b) 0.5 (c) 0.6 (d) 0.8.

Luo *et al.* [181] attributed the dynamic transformation from ferrite to austenite they observed after intercritical deformation of their C-Mn steel, to be a result of changes in the equilibrium fractions due to the variation of the respective stored energies in the two phases brought about by different softening mechanisms. In their case, ferrite to austenite transformation was observed after deformation and their results also suggest that ferrite-to-austenite DT was dependent on softening kinetics in the two phases. However, in this work, the ferrite-to-austenite DT was observed during deformation soon after the peak strain, giving an impression that a critical strain was necessary for the build-up of stored energy necessary for the DT, as is the case with DIFT [109], [141]. Attempts to determine the critical strains for DT for different deformation conditions using the double differential method suggested in previous studies [154], [155], proved futile. The reason for this can be attributed to the two phases already present while the method was validated when deformation was carried out on a single phase with a second phase being introduced during deformation. A study by Chung

et al. [182] also confirms the difficulty of predicting the critical strain of DT in a two-phase region. Most importantly, the manner in which ferrite to austenite DT is observed to take place is significantly different to that of austenite to ferrite dynamic transformation in fully austenitic materials, e.g. in C steels where it is easy to observe changes in flow behaviour due to commencement of DT [77], [126], [171], [181]. The reason for the conventional methods not being able to determine the critical strain for DT, can be attributed to the manner that DT takes place, which in this case is through strain-induced boundary migration, as pointed out later in the thesis and shown in Appendix A6. These interesting observations of a change in phase fraction with strain were critically analysed for deformation at 850^{o}C and 10 s^{-1} strain rate, and can also be done for other deformation conditions. Though the change in phase fraction with strain persisted at other deformation conditions, it will be worthwhile also to investigate if the pattern observed for 850^{o}C and the 10 s^{-1} strain rate, persists at other temperatures at this strain rate. Increasing the strain beyond 0.6 to 0.8 and strain rates to 15 s^{-1} rendered the temperature effect insignificant, as the volume fraction was found to be almost constant for the temperature range investigated (850 -1050 ^{o}C) as shown in Figure 6.10.

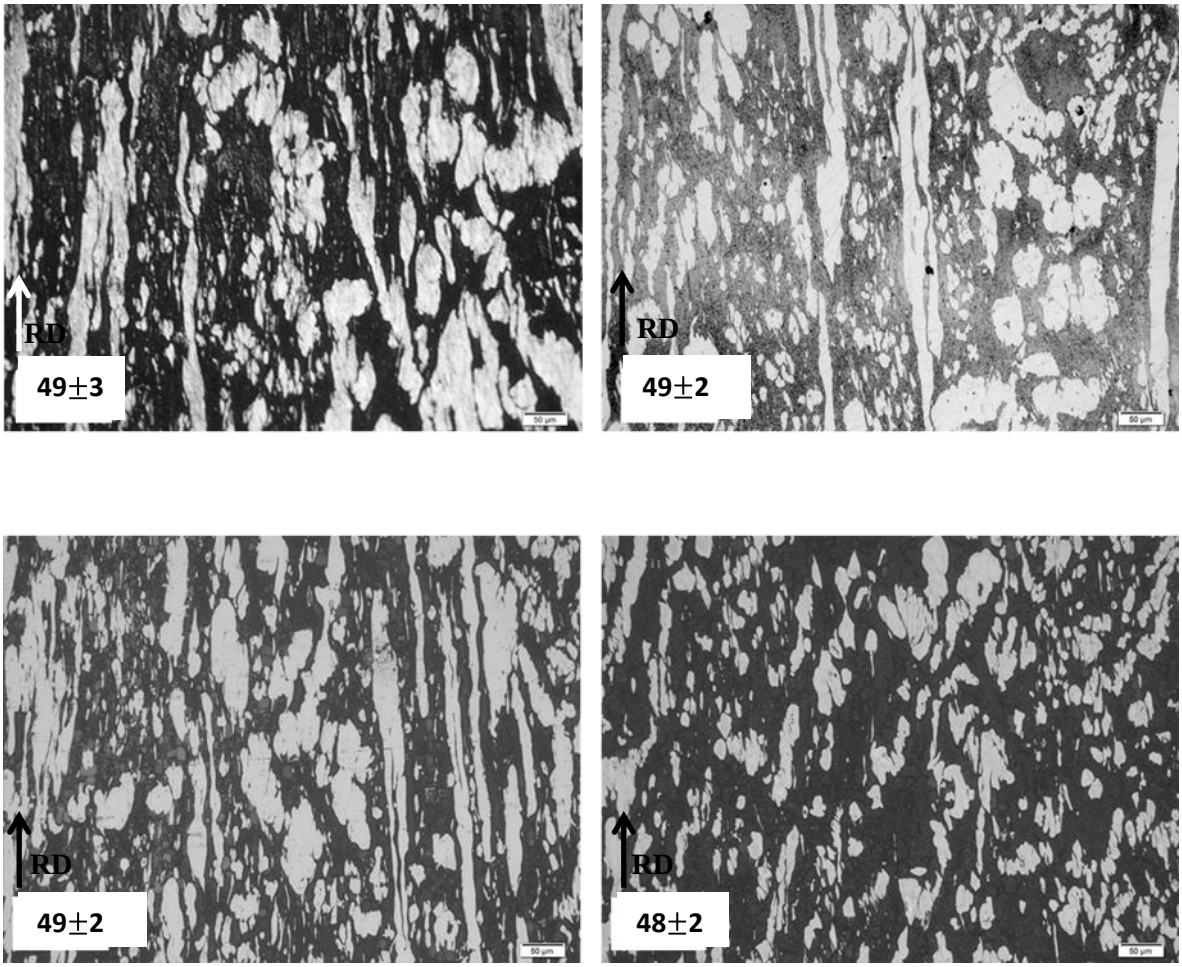

Figure 6.10: Variation of austenite volume fraction at a strain rate of 15 s^{-1} with temperature (a) 900 ^{o}C (b) 950 ^{o}C (c) 1000 ^{o}C (d) 1050 ^{o}C. (Strain = 0.8).

The mechanism behind DT can be inferred to be SIBM where the phase with lower strain energy (austenite) due to DRX, bulges into the one with higher strain energy (ferrite). DRV unlike DRX, does not lower the strain in ferrite and also due to ferrite being in the vicinity of the harder phase, is likely to have undergone further work hardening, resulting in the accumulation of more strain energy. This was observed by the boundary misorientation differences between the two phases, see Figure 6.11b. Thus, the driving force is the difference in strain energy across the austenite-ferrite phase boundary, resulting in the austenite bulging encompassing the high energy ferrite, as shown in Figure 6.11a. As may be seen, the occurrence of SIBM can be noted from protrusions of the austenite phase into the ferrite matrix (labelled 1and 2) and serrations of the austenite growth front (labelled 3 and 4). SIBM is thus regarded as responsible for the DT and hence the increase in austenite phase fraction observed during deformation, as illustrated in Appendix 7. The Gibbs free energy change related to this process is reviewed in Appendix 8.

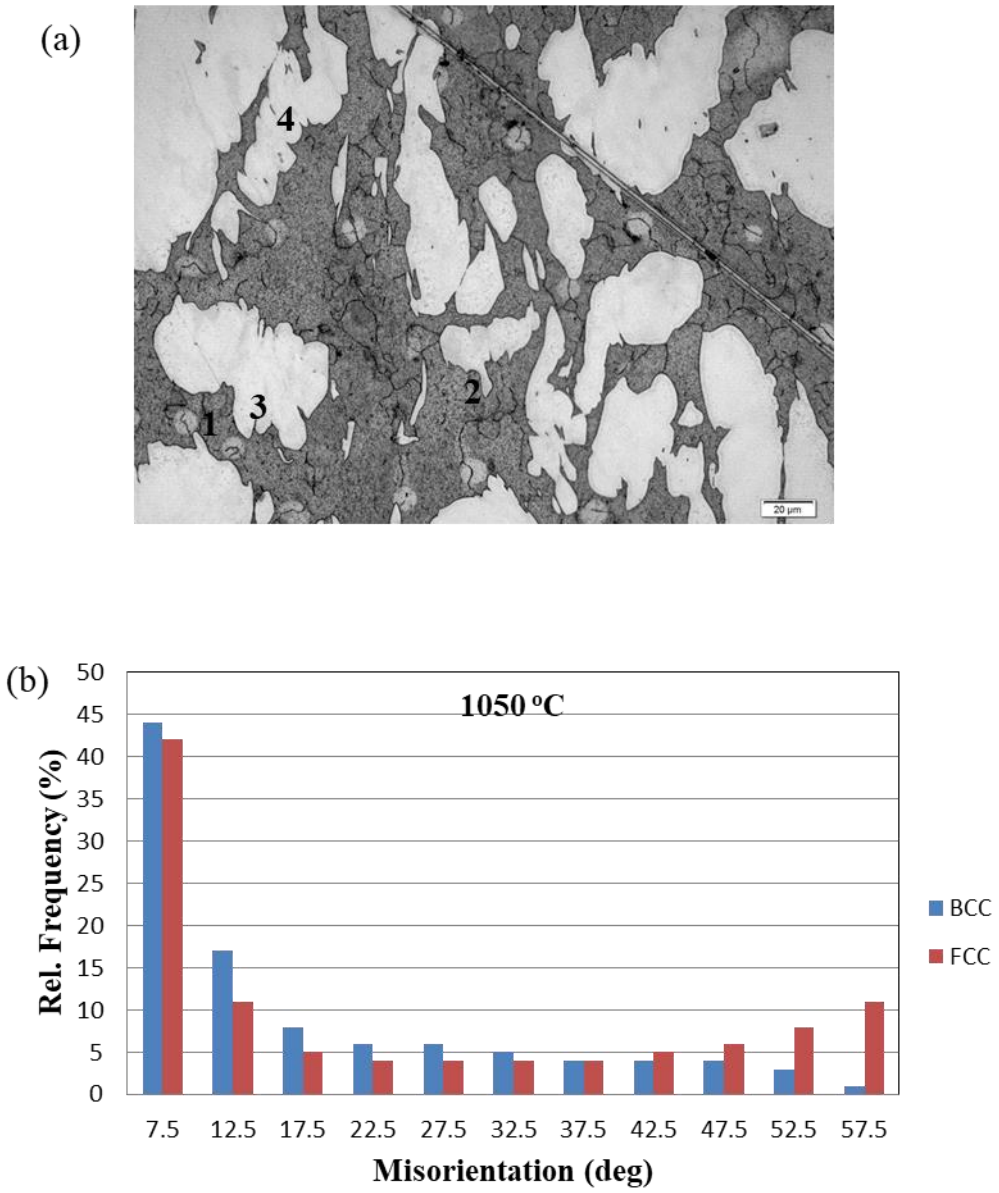

Figure 6.11: (a) Optical micrograph showing SIBM taking place during deformation at 1050 ^{o}C, and 5 s^{-1} strain rate. 1 and 2 show protrusions; 3 and 4 show serrations (b) Corresponding distribution of misorientation angles in ferrite and austenite.

6.3.2 Volume fraction changes during inter-pass time

The volume fraction of austenite was also observed to be independent of the interpass time. In order to assess the effect of the interpass time on the austenite volume fraction, the deformed sample was held at the deformation temperature for the target time before quenching. The volume fraction of austenite showed little or no variation with interpass time (Figure 6.12), indicating that during interpass times in hot rolling the austenite volume fraction will remain unaffected i.e. at quasi-equilibrium. From the results above, the driving

force DT was observed to be the stored energy due to different dynamic restoration processes in the respective two phases and in the interpass time, this energy would have been severely diminished due to DT and DRX. As DT and DRX occur almost concurrently during deformation, this results in the strain energy differnce between the two phases being significantly lowered after deformation.This, in turn diminishes SIBM and further DT, hence the observed “no further phase change” upon holding or annealing after deformation (which is equivalent to a lenthy interpass time).

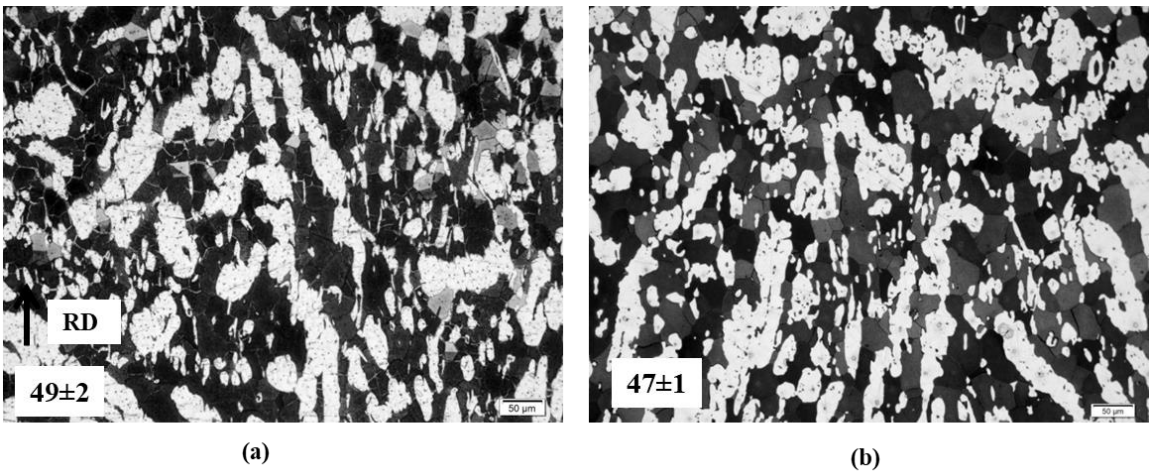

Figure 6.12: Variation of austenite volume fraction with interpass time (a) 15 s (b) 30 mins.

6.4 EBSD Analysis

6.4.1 Effect of temperature at low strain rate ($0.1s^{-1}$)

Figure 6.13 shows the boundary misorientation maps for the ferrite phase (dark) and austenite phase (light) obtained from EBSD data of the hot deformed duplex steel with a strain of 0.6 at two different temperatures but the same strain rate of 0.1 s^{-1}. Deformation of the steel at a lower and higher temperature of 850 ^{o}C and 1050 ^{o}C, respectively resulted in different microstructures. Low-angle grain boundaries (LAGBs) with misorientations of 2 – 15^{o} are shown by green and red lines in the ferrite and austenite phases, respectively and high-angle grain boundaries (HAGBs) with misorientation angles $\theta > 15^{o}$ are shown by black lines in both phases . Austenite is shown as the lighter phase while ferrite is indicated as a darker phase. At 850 ^{o}C, the ferrite microstructure contained a very high density of sub-grains and LAGBs. The austenite phase on the other hand, exhibited a microstructure with a lower amount of LAGBs when compared to the ferrite phase. The LAGBs in ferrite decreased substantially when deformation was carried out at a higher temperature of 1050 ^{o}C. The

amount of substructure in the ferrite decreased as less strained sub-grains and grains became more prominent. This can most likely be attributed to the higher temperature promoting more cross-slip and climb in ferrite, hence more DRV. The austenite microstructure at 1050 ^{o}C is characterized by a high fraction of LAGBs, indicating limited DRX as also confirmed by misorientation distribution plots, Figure 6.14. Misorientation distribution plots show a small change in the ferrite microstructure as the temperature is increased from 850 ^{o}C to 1050 ^{o}C for a low strain rate deformation, i.e. a small reduction in LAGBs and a small increase in HAGBs. However, for the austenite microstructure the change in the amount of LAGBs and HAGBs is significant as the temperature is increased from 850 ^{o}C to 1050 ^{o}C. The large fraction of LAGBs and small fraction of HAGBs at the higher temperature of 1050 ^{o}C and a contrary observation at the lower of 850 ^{o}C, indicated that at higher temperatures, DRX is limited in austenite. This can be attributed to high temperatures favouring DRV which ultimately reduces the driving force for DRX. At lower temperatures, DRV is limited and hence enough strain to trigger DRX is accumulated.

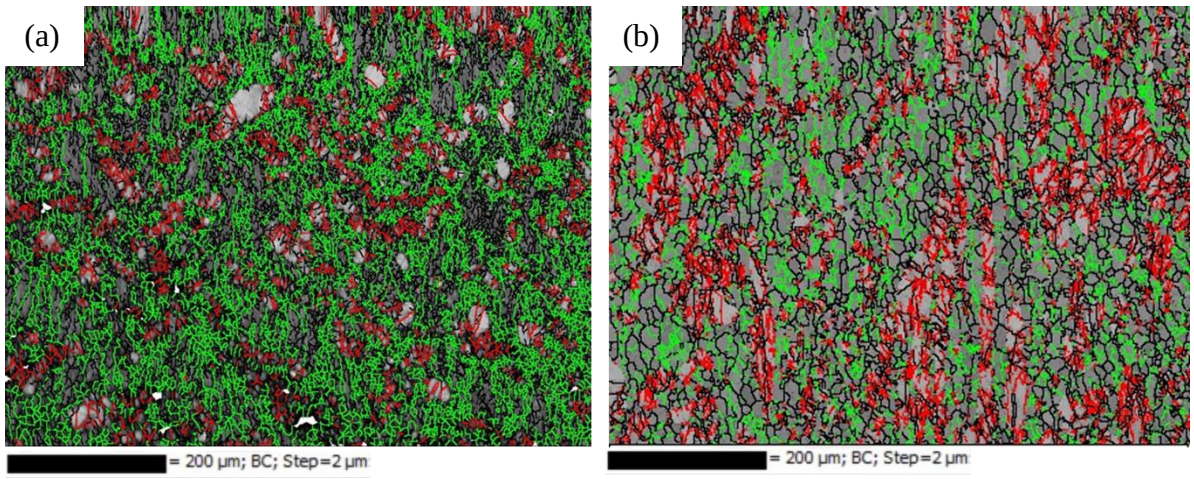

Figure 6.13: Subgrain and grain structures at 0.1 s^{-1}: (a) 850 ^{o}C (b) 1050 ^{o}C. Green and red represent low angle grain boundaries (LAGB) in ferrite (dark phase) and austenite (light phase) respectively. HAGB are shown by black colour in both phases.

Figure 6.14 reveals the distribution of misorientation angles between grains in both phases at the two temperatures of 850 ^{o}C and 1050 ^{o}C. The misorientation distribution showed no significant change in ferrite sub-grain and grain boundaries as the temperature increased from 850 to 1050 ^{o}C at a strain rate of 0.1 s^{-1}. As for austenite, the misorientation distribution plots show a clear decrease in the fraction of high-angle misorientation boundaries (with misorientation > 15^{o}) as the deformation temperature was increased from 850 to 1050 ^{o}C.

Conversely, the fraction of low-angle misorientation boundaries increased by approximately 20 % as the temperature increased from 850 to 1050 ^{o}C.

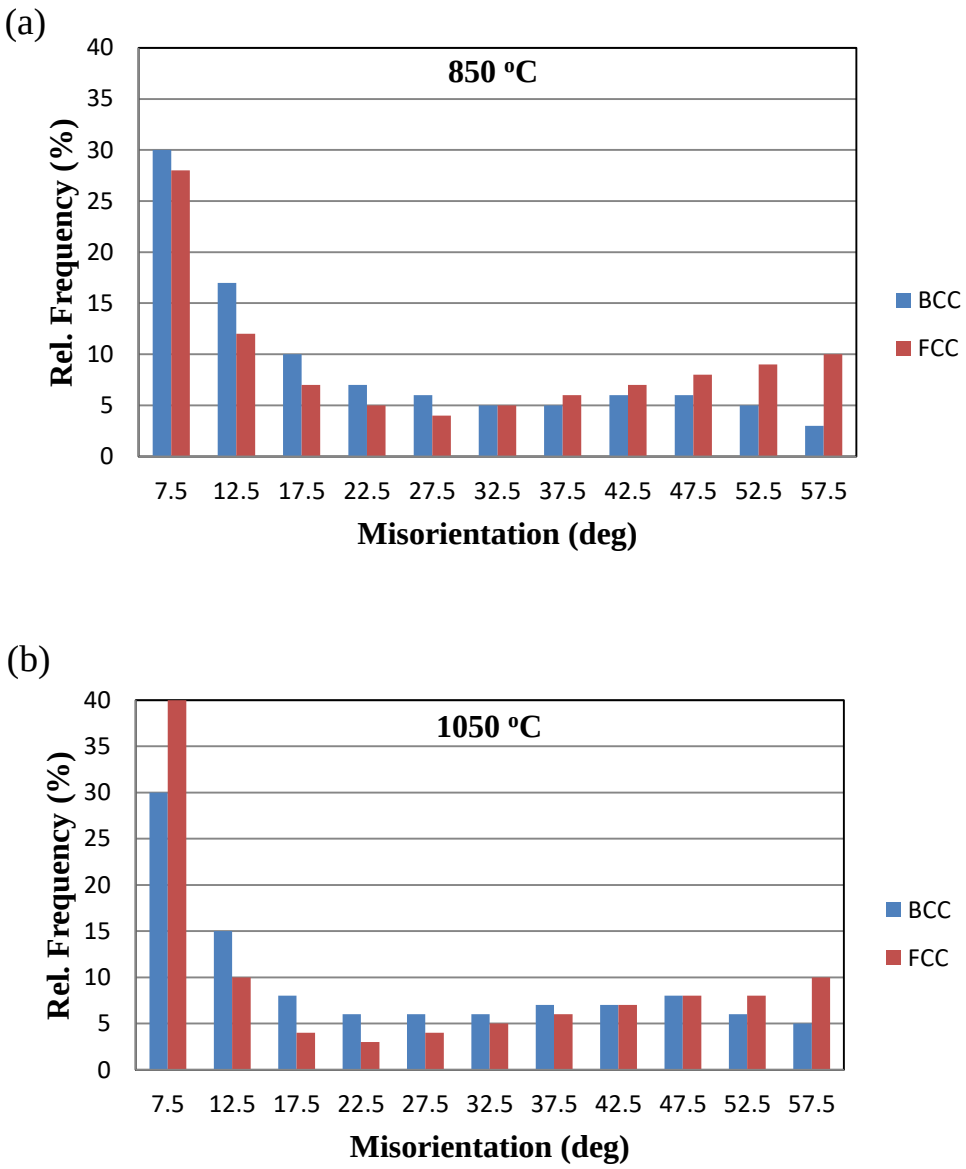

Figure 6.14: Distribution of misorientation angles in ferrite and austenite at: (a) 850 ^{o}C (b) 1050 ^{o}C deformed at a low strain rate of 0.1 s^{-1}.

6.4.2 Effect of temperature at a high strain rate (15 s^{-1})

Figure 6.15 shows the boundary misorientation maps for the ferrite phase (dark) and austenite phase (light) of the hot deformed duplex steel with a strain of 0.6 at two different temperatures and at a strain rate of 15 s^{-1}. Low-angle grain boundaries (LAGBs) with misorientations of 2 – 15^{o} are shown by green and red lines in ferrite and austenite phases, respectively and high-angle grain boundaries (HAGBs) with misorientation angles greater

than 15^{o} are shown by black lines in both phases. At 850 ^{o}C, both ferrite and austenite phases contained a very high density of LAGBs. Under these deformation conditions, even identifying substructures or sub-grains was virtually impractical as both phases showed a substantial amount of deformation. When deformation was carried out at a higher temperature of 1050 ^{o}C, very fine ferrite grains surrounded by high angle grain boundaries were observed. These were most likely formed from the fragmentation of the initial grains (Figure 6.15b). The very fine equiaxed grains were formed at high temperature where the possibility of these grains having been generated from DIFT can be ruled out. At 1050 ^{o}C, the austenite phase on the other hand, exhibited a substantial amount of LAGBs and sub-grains. A higher magnification EBSD image of Figure 6.15 is shown in Figure 6.16, which correlates well with the analysis of distribution of misorientation angles.

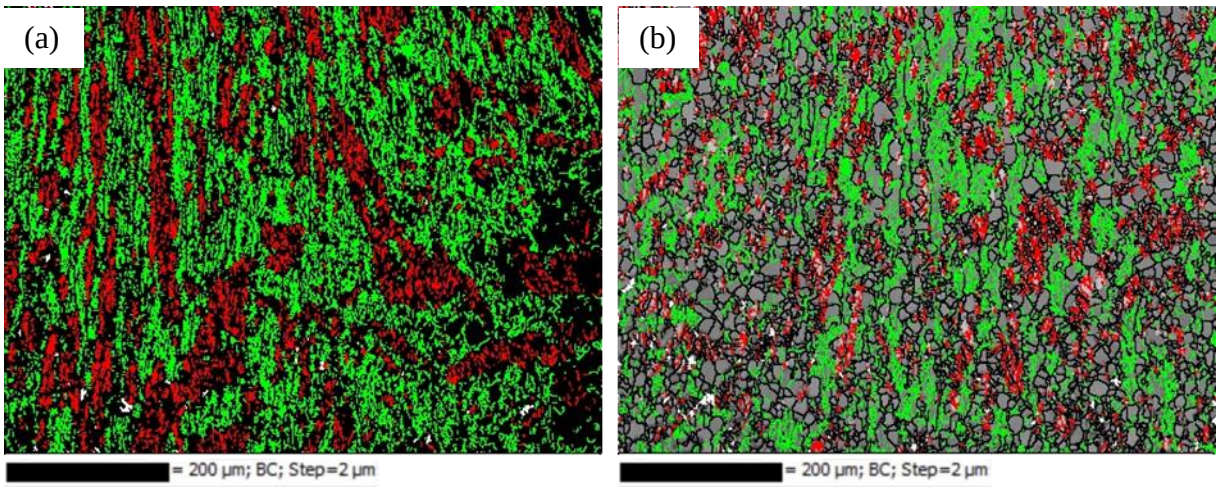

Figure 6.15: Subgrain and grain structures at a strain rate of 15 s^{-1}: (a) 850 ^{o}C (b) 1050 ^{o}C. Green and red represent low angle grain boundaries (LAGB) in ferrite and austenite respectively. HAGB are shown by black colour in both phases.

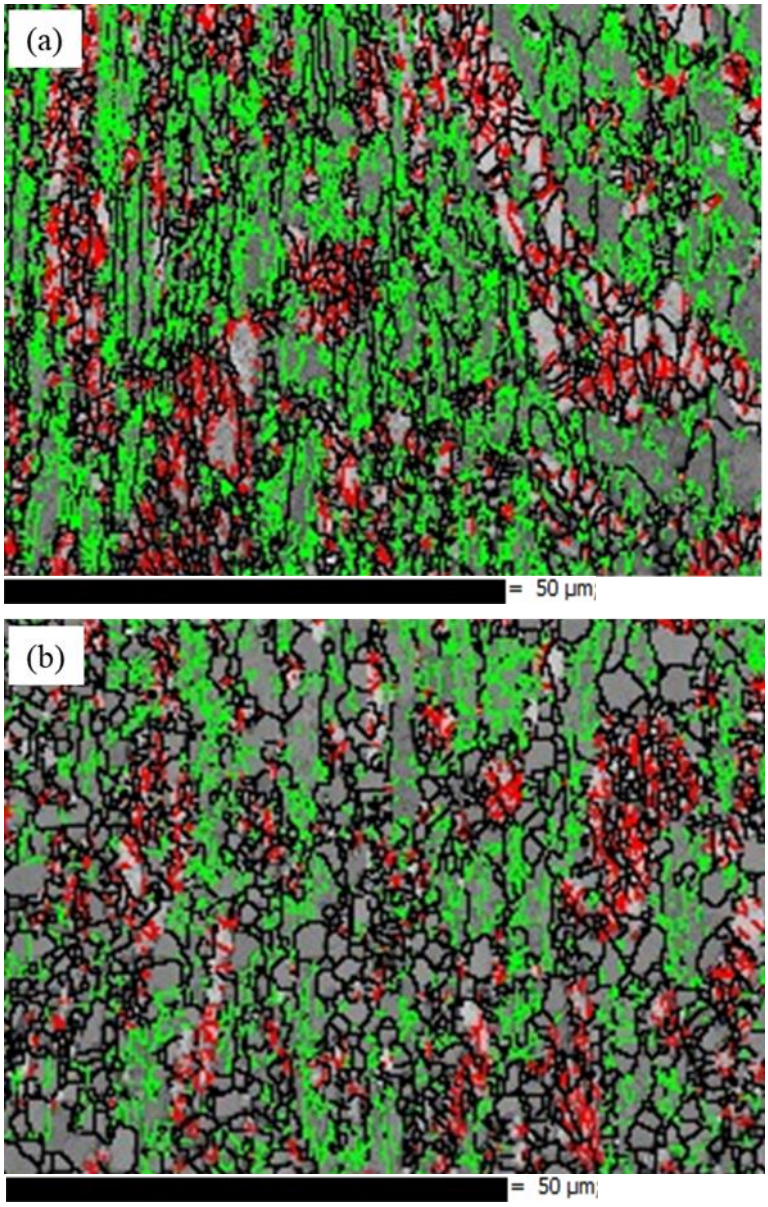

Figure 6.16: Subgrain and grain structures at 15 s^{-1}: (a) 850 ^{o}C (b) 1050 ^{o}C (Figure 6.12)). Green and red represent low angle grain boundaries (LAGB) in ferrite and austenite respectively. HAGB are shown by black colour in both phases.

Figure 6.17 shows the distribution of misorientation angles between grains in the two phases at the two temperatures of 850 ^{o}C and 1050 ^{o}C. The misorientation distribution plots (Figure 6.17a and 6.17b) indicate a very high fraction of LAGBs in both phases when the deformation is carried out at a lower temperature and a high strain rate (15 s^{-1}). The distribution of misorientation angles indicated that at 850 ^{o}C and a strain rate of 15 s^{-1}, LAGBs dominated in both phases with the total distribution as high as 73 % and 52 % in ferrite and austenite phases, respectively. The high strain rate used could be an explanation of why the fraction of HAGBs was so small, approximately 27 %. The high strain rate may have

limited the time available for LAGBs to shift to HAGBs through CDRX, hence the observations made [123], [183]. As for austenite, though the temperature favoured build-up of stored energy from strain hardening, dynamic recrystallization is a time-dependent process and high strain rates result in limited time for DRX and hence incomplete recrystallization.

For the ferrite phase, increasing the temperature to 1050 ^{o}C resulted in a significant drop in LAGBs from 73 % at 850 ^{o}C to 44 % at 1050 ^{o}C. This can be attributed to improved mobility of grains at this temperature resulting in more CDRX, revealed by the increase in HAGBs (as can also be seen in Figure 6.16b). The misorientation distribution plots showed little change in the fraction of both LAGBs and HAGBs in austenite as the temperature of deformation increased from 850 ^{o}C to 1050 ^{o}C (Figure 6.17a and 6.17b). This can be attributed to an increased dislocation climb at higher temperatures, improving the DRV process and thereby lowering the amount of dislocation substructures and at the same time the amount of stored energy available for DRX.

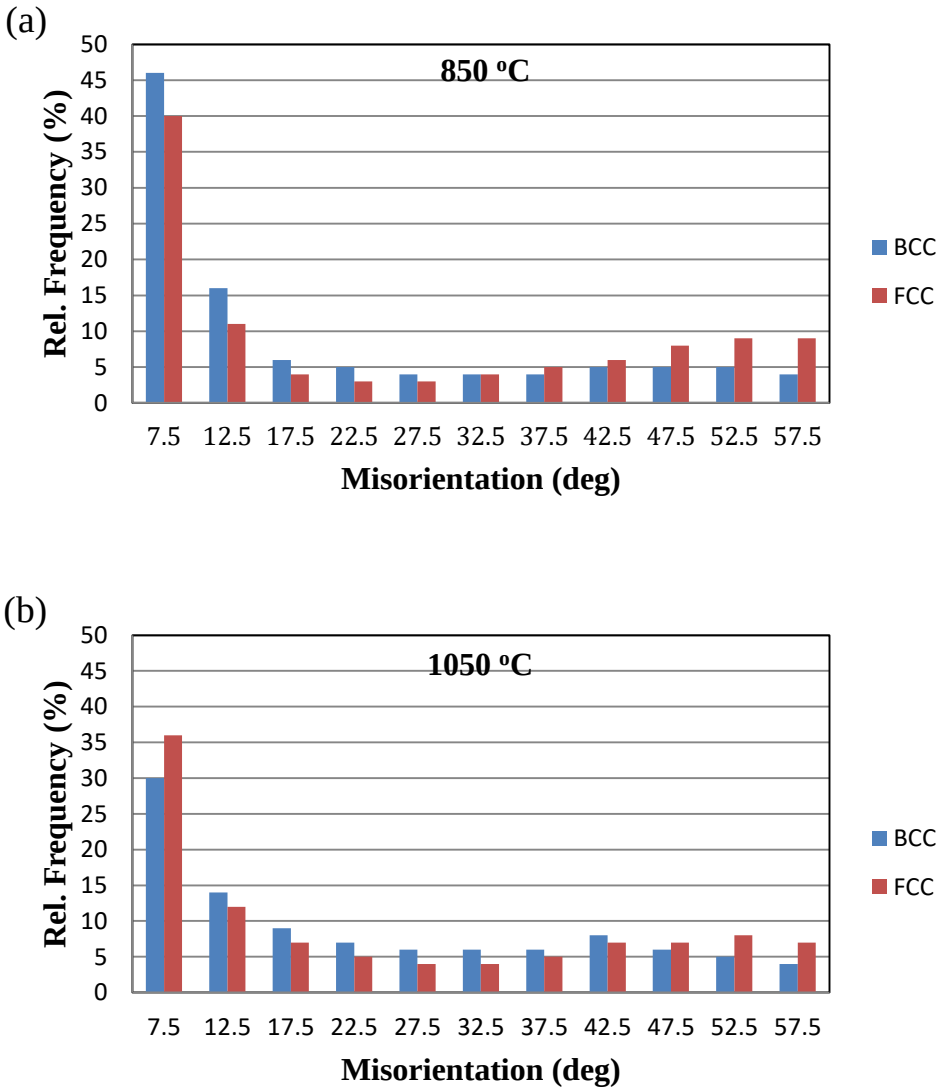

Figure 6.17: Distribution of misorientation angles in ferrite and austenite at: (a) 850 ^{o}C and (b) 1050 ^{o}C after being deformed at a high strain rate of 15 s^{-1}.

6.4.3 Effect of strain

The grain boundaries in ferrite are distinguished by green and black colours where green and black colours show low and high angle grain boundaries, respectively. Likewise, the low and high angle grain boundaries in austenite are indicated by red and black, respectively. The boundary misorientation maps in Figure 6.18 show an increase in the LAGB with strain in both phases. At very small strains (ε = 0.05), the boundary misorientation maps show very few low angle boundaries (LAGBs) and the grain boundaries are typical of an annealed material. Doubling the strain to 0.1 sees an increase in the LABs and diminishing of HAGBs in both phases. Further doubling the strain resulted in a rapid increase in LAGBs in ferrite

suggesting the presence of highly deformed substructures with minimum recovery having taken place. The same can be said for austenite, where recovery is also sluggish and DRX is triggered after attaining a critical strain.

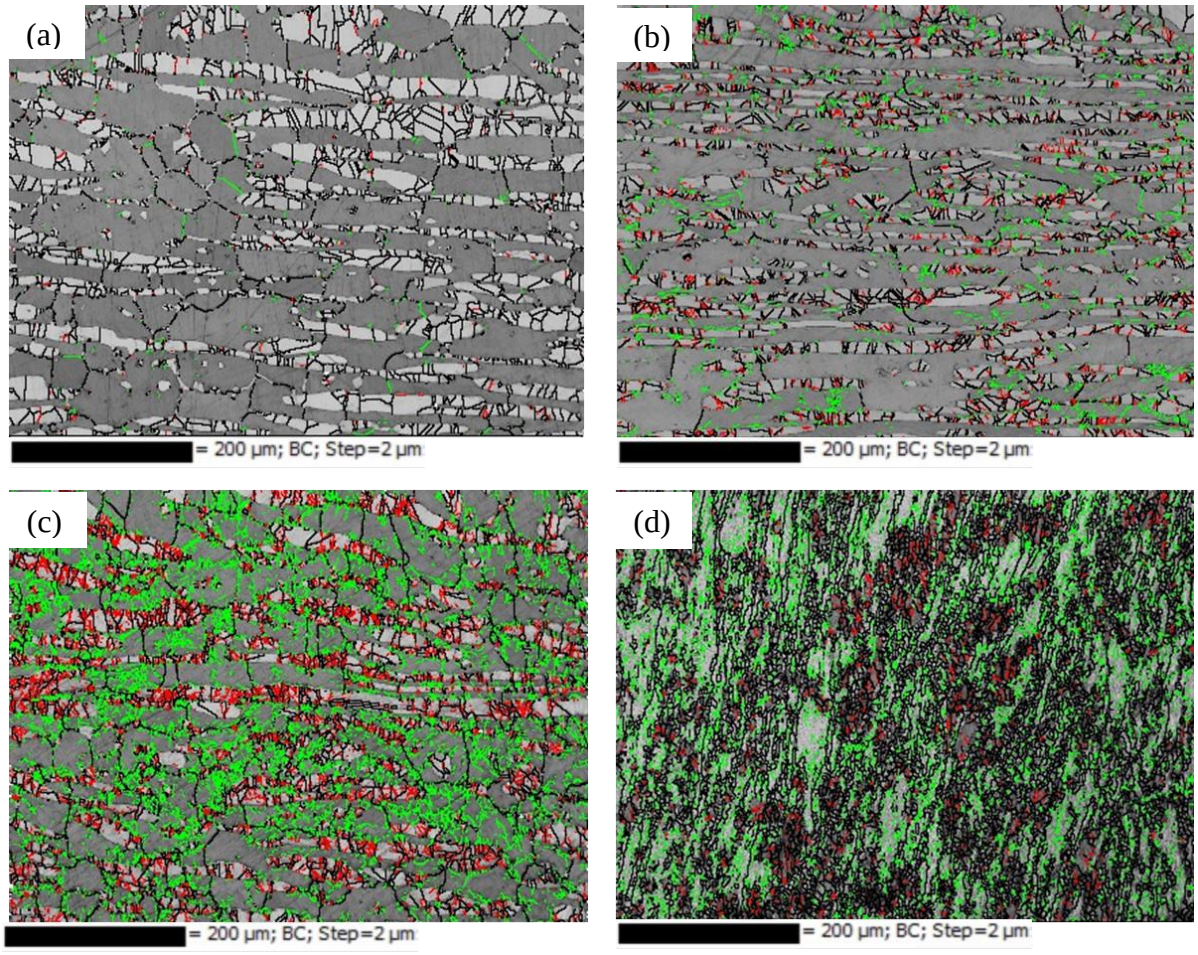

Figure 6.18: Subgrain and grain structures at 850 ^{o}C with a strain rate of 10 s^{-1} with strains of: (a) 0.05; (b) 0.1; (c) 0.2; (d) 0.8. Green and red represent low angle grain (LAGB) boundaries in ferrite and austenite respectively. HAGB are shown by black colour in both phases.

The boundary misorientation maps seem to suggest that at a strain of 0.1, the softer phase (ferrite) has accommodated more strain than the harder phase, which of course is attributed to the difference in their SFEs. The SFE for austenite reported to be about 20 mJ/m^2 [184] and estimated to effectively be in the range of 160-200 mJ/m^2 for ferrite [185]. The high SFE value of ferrite ensures that cross slipping of dislocations takes place with relative ease, prompting DRV and making the phase prone to deformation unlike in austenite where the softening mechanism through climbing of dislocations is significantly lower. The limited dislocation motion in austenite makes the phase more difficult to deform compared to ferrite,

which results in more strain being partitioned to ferrite at low strains. At a higher strain which in this case is 0.8, some very fine grains can be clearly seen with a reduced density of LABs (Figure 6.18d and Figure 6.19). Apart from HAGBs which can be clearly observed in austenite from DDRX, a small fraction of HAGBs can also be observed in ferrite, possibly evolving from LAGBs through extended recovery or CDRX [125], [186]. This form of ferrite grain refinement during warm (two-phase) deformation is well documented [132], [133], [136].

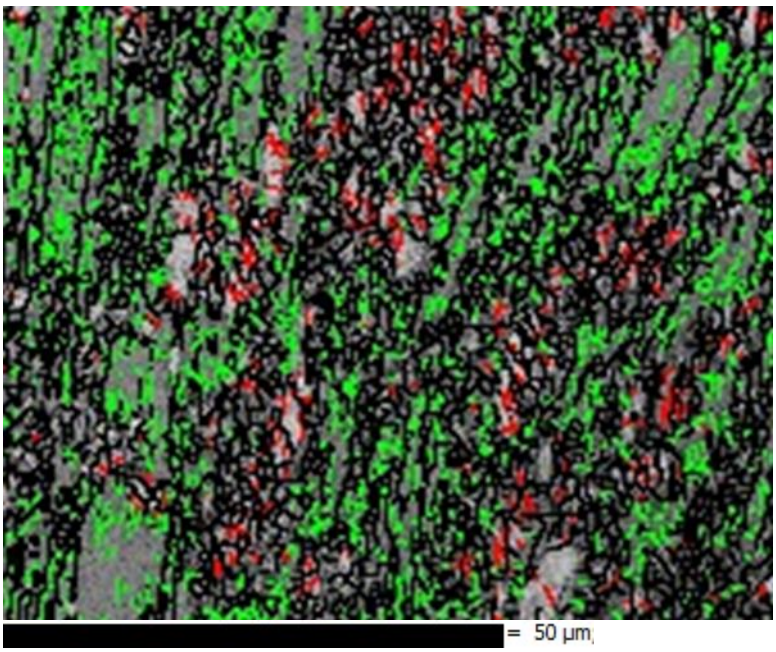

Figure 6.19: Subgrain and grain structures after deformation at 850 ^{o}C, a strain rate of 10 s^{-1} and a strain of 0.8. Green and red represent low angle grain (LAGB) boundaries in ferrite and austenite respectively. HAGB are shown by black colour in both phases.

Figure 6.20 shows the inverse pole figure (IPF) map corresponding to Figure 6.19. The IPF map verifies the limited CDRX and localized strain in ferrite due to significant colour variation within the grain. The more deformed grains show variation in colour across the grain, while the less deformed show less colour variation. Recrystallized grains do not show any colour variation. As for austenite, the grains do not show much colour variation and are also observed to be very fine which is indicate that the phase could have undergone DRX. The same principle was applied throughout the thesis in terms of use of inverse pole figure maps.

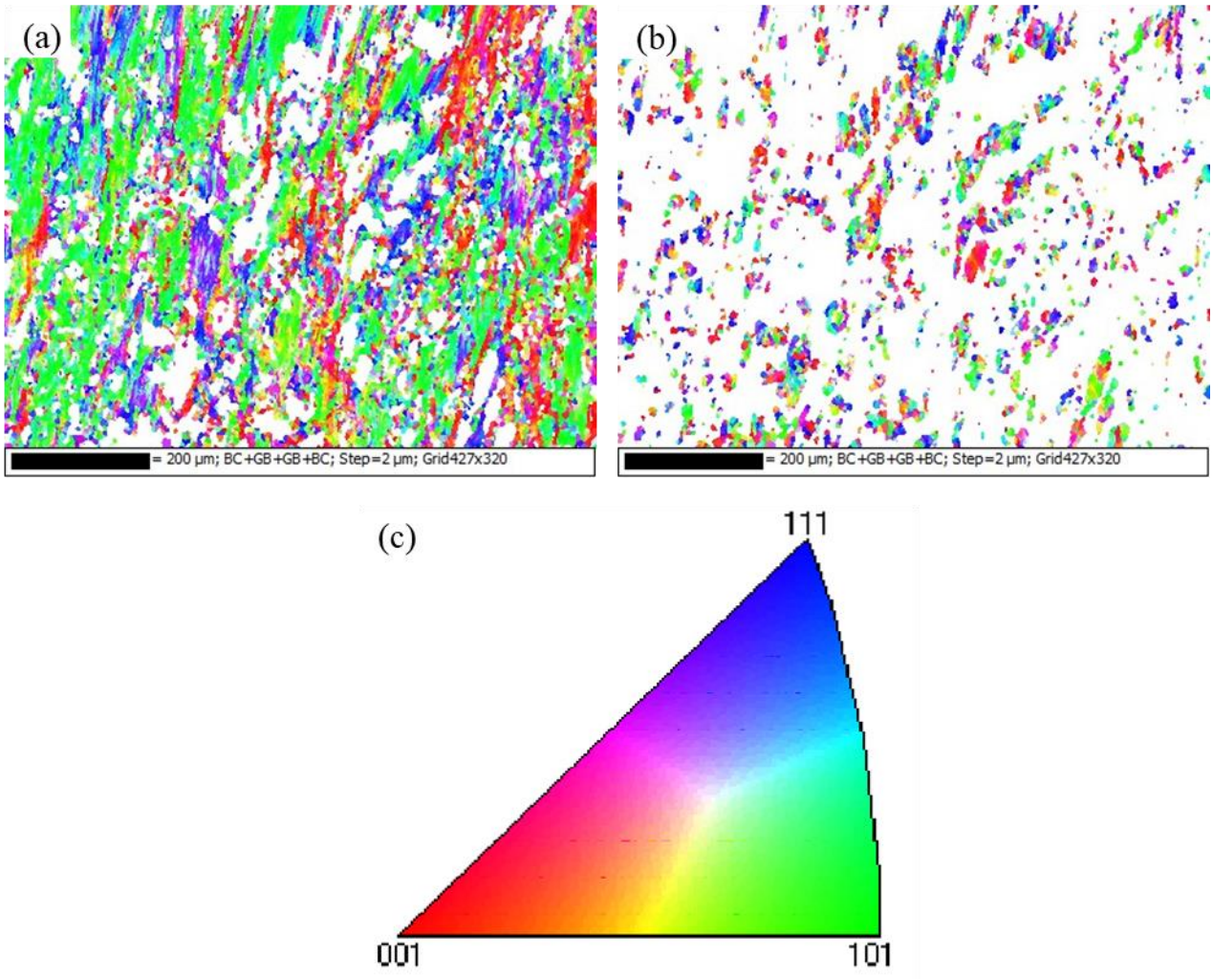

Figure 6.20: EBSD IPF Map for Ferrite (a) Austenite (b) and (c) IPF legend.

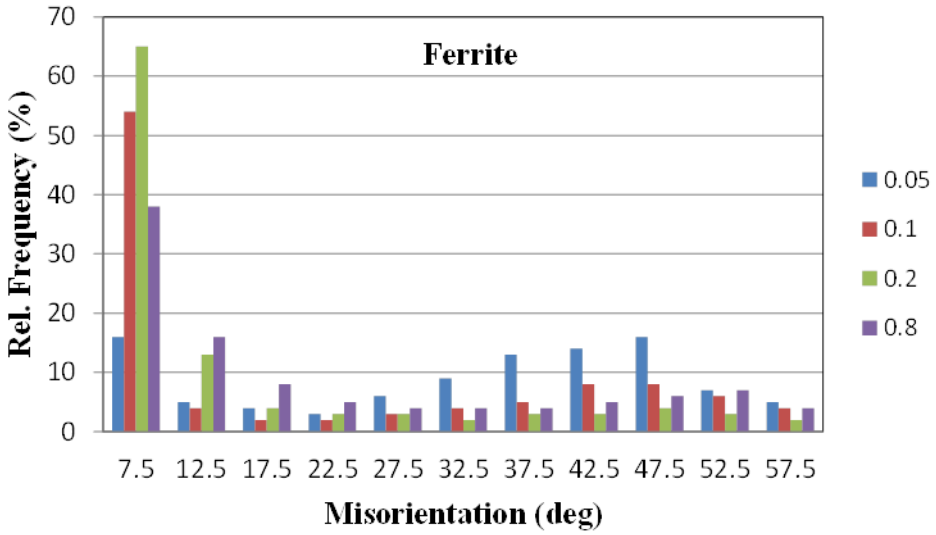

Figure 6.21: Distribution of misorientation angles in ferrite deformed to different strains of 0.05, 0.1, 0.2 and 0.8 at 850 ^{o}C at strain rate of 10 s^{-1}.

The distribution of misorientation angles calculated from EBSD (Figures 6.21 and 6.22) support the observations from the boundary misorientation maps. The distribution of misorientation angles in ferrite at a strain of 0.05 shows a low fraction of LAGB and a very high fraction of HAGBs, typical of an annealed material. The presence of a greater fraction of HAGBs and less LAGBs is as expected at the strain of 0.05 due to minimal deformation and dislocations being generated. As the strain increases from 0.05 to 0.2, the LAGBs increase from 21% to 78% and conversely the HAGBs decrease from 79% to 22%. At a strain of 0.8, the fraction of LAGBs is reduced to 54 % while the HAGBs increased to 46 %. The reduction in LAGBs and increase in HAGBs at higher strains can be attributed to CDRX of ferrite and migration of the recrystallized austenite front into ferrite. For the austenite phase the LAGBs increase less significantly from 4% to 44 % for a strain increase in strain from 0.05 to 0.2 while the fraction of the HAGBs remains high, i.e. at 56% at a strain of 0.2. The observation confirms that at low strains the greater part of the strain is partitioned to ferrite during deformation of this steel. Hence, there is a very minimal deformation of the austenite phase. It would be expected at large strains that there will be a very high fraction of LAGBs and a very low fraction of HAGBs, but interestingly the fraction of LAGBs and HAGBs in austenite at 0.8 is equal to that at a strain of 0.2. This confirms the observation that at this strain steady state has been attained.

The microstructure appeared homogeneous, seemingly suggesting possible occurrence of DRX, which in this case would be CDRX in ferrite [125], [186]. The observations from the distribution of misorientation angles in austenite are not any different from those from ferrite. The only difference could possibly be the manner in which LAGBs evolved to HAGBs, which in low SFE materials would be through DDRX or SIBM [63]. The flow softening accompanying the increase in strain, suggests that DRX is indeed taking place in austenite. If it were not so, the observed flow softening would not have been possible (Figure 6.8).

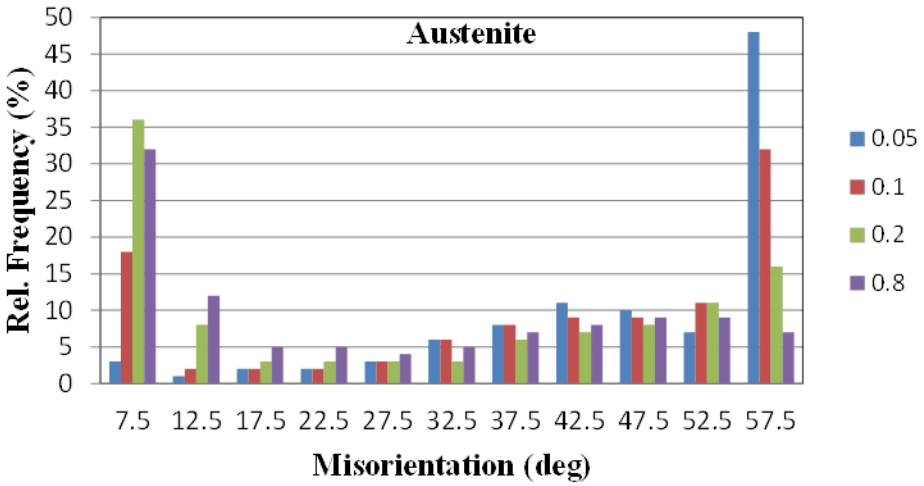

Figure 6.22: Distribution of misorientation angles in austenite deformed to different of strains of 0.05, 0.1, 0.2 and 0.8 at 850 ^{o}C at a strain rate of 10 s^{-1}.

The distribution of LAGBs and HAGBS after deformation to a strain of 0.6, strain rate and temperature of 10 s^{-1} and 850 ^{o}C, respectively is shown in Figure 6.23. Comparing the Figures 6.16 and 6.18, which are both high magnification images, CDRX can be approximated to have been initiated at strains beyond 0.6. This is where the DT is observed to slow down due to the reduced dislocation density difference between the two phases (Figure 6.8).

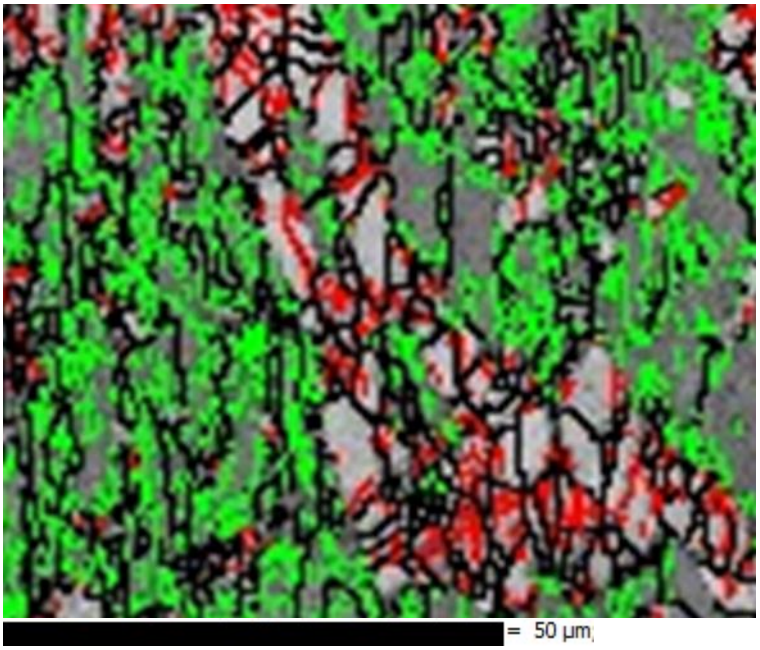

Figure 6.23: Subgrain and grain structures at 850 ^{o}C at a strain rate of 10 s^{-1} deformed to 0.6. Green and red represent low angle grain (LAGB) boundaries in ferrite and austenite respectively. HAGB are shown by black colour in both phases.

In Figure 6.24, a decrease in the LAGBSs with an increase in strain from 0.6 to 0.8, is observed in both phases. The changes however do not indicate that any additional driving force can result from an increase in strain from 0.6 to 0.8, hence the observed flattening of the flow stress curve typical of quasi-steady state having being attained. This is also confirmed by the absence of any volume fraction changes with an increase in strain in this range. The distribution of misorientation angles confirm that the DRX observed through increased density of HAGBs observed in EBSD maps as the strain increased from 0.6 to 0.8. Evolution of LAGBS to HAGBs through CDRX in ferrite also ensures that the driving force for SIBM that existed before CDRX, is diminished.

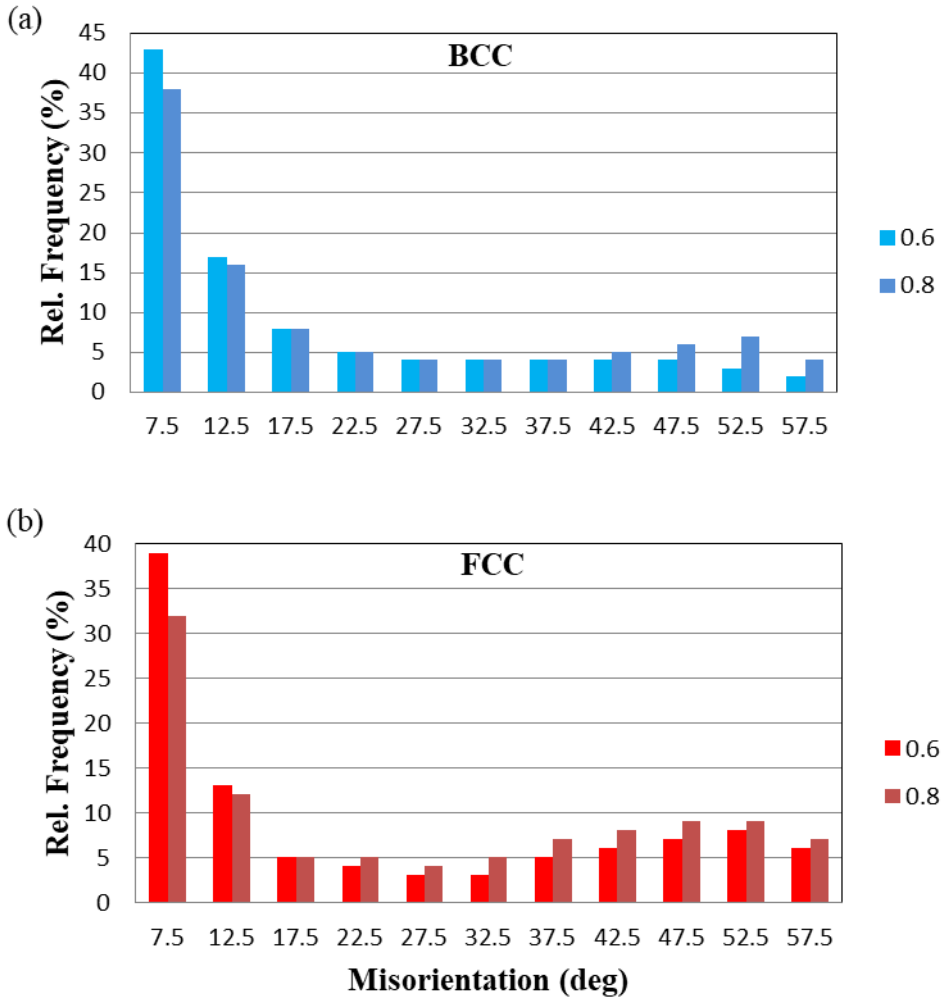

Figure 6.24: Distribution of misorientation angles in (a) ferrite (b) austenite at strains of 0.6 and 0.8.

6.4.4 Effect of inter-pass time

Figure 6.25 shows the differentiation in the typical microstructure of the sample quenched soon after deformation in Figure 6.24 (a) and the one held at the deformation temperature of 1050 ^{o}C, for a duration of 20 s which is equivalent to a typical industrial rolling inter-pass time, Figure 6.25 (b). A significant reduction in the LAGB in both ferrite and austenite is observed. Refined equiaxed grains in both phases with high angle boundaries, are also observed. This change in microstructure could possibly be due to MDRX resulting from the stored energy acquired from deformation. The lack of DRX at this strain rate and temperature in Figure 6.25 (a), can be envisaged to be two way. Firstly, this shows that at this particular strain rate (0.1 s^{-1}), MDRX could not have taken place due to no interpass times (0s) or

secondly, the driving force was not enough for DRX to take place, hence the observed grain structures with LAGBs in both phases.

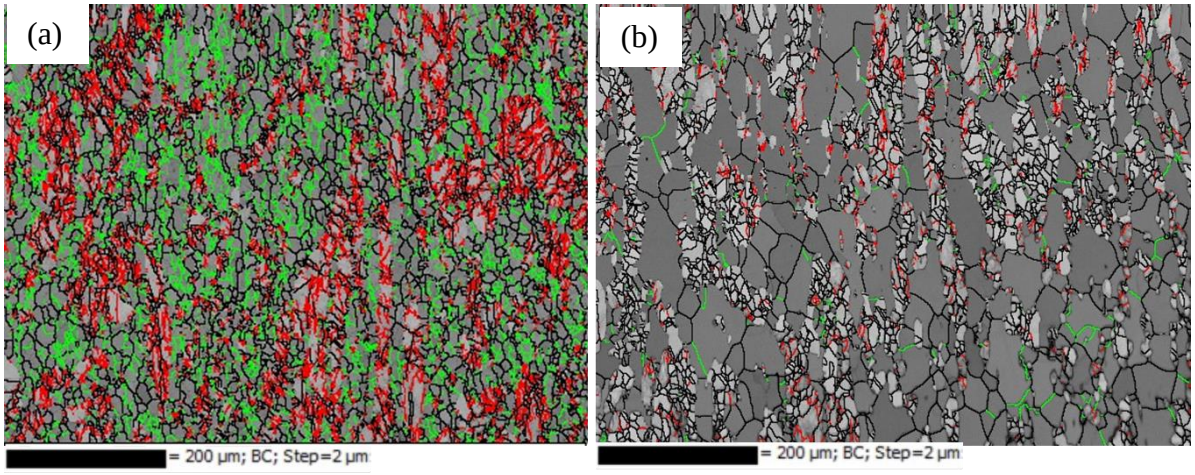

Figure 6.25: Evolution of LAGBs ($7 < \theta \leq 15^o$, green lines) and HAGBs ($15^o < \theta$, dark lines) of ferrite (dark phase) and LAGBs ($7 < \theta \leq 15^o$, red lines) and HAGBs ($15^o < \theta$, dark lines) of austenite (light phase) with interpass time of: (a) 0 s and (b) 20 s.

6.5 Modelling the saturation stress flow behaviour

6.5.1 Hyperbolic sinh equation

According to these findings, it can be concluded that the main mechanism in operation before the peak is DRV, hence at the point where $d\sigma/d\varepsilon = 0$, a saturation stress is attained and this will continue to be so (steady state) for no DRX that results in flow softening after the peak. Though DRX is initiated before the peak, its effects on the flow behaviour can be considered to be negligible and the peak stress is estimated to be approximately equal to the saturation stress. With this assumption in place, the sinh hyperbolic type equation proposed by Sellars and Tegart [187] for steady state stress was used to predict the saturation stress, given the momentary $d\sigma/d\varepsilon = 0$, close to the peak stress. This condition can therefore be exploited in predicting the saturation stress assuming no softening occurs, and the peak stress is used. In order to find the constant α for this material, equations [5-22] and [5-23] are used to make plots of ln σ against ln ἑ and σ against ln ἑ, to find the values of η and β, respectively (Figure 6.26). The values of η and β were found to be 9.2 and 0.0573 MPa^{-1}, respectively. The value of $\alpha = \beta/\eta$ is found to be 0.00623 MPa^{-1} while n and Q are determined from plots of ln $[\sinh(\alpha\sigma_p)]$ against ln **(**strain rate**)** and ln $[\sinh(\alpha\sigma_p)]$ against 1/T, respectively (Figure 6.27). The apparent activation energy Q is thus considered to be apparent activation energy where dynamic recrystallization effects can be considered to be minimal.

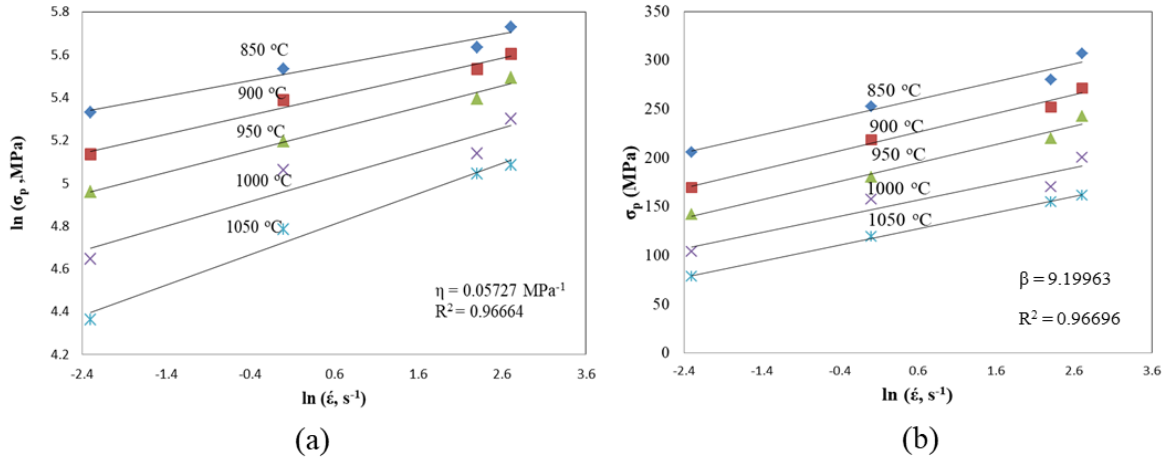

Figure 6.26: Plot of (a) ln σ_p vs ln $\dot{\varepsilon}$ (b) σ vs ln $\dot{\varepsilon}$ for the determination of α at σ_p.

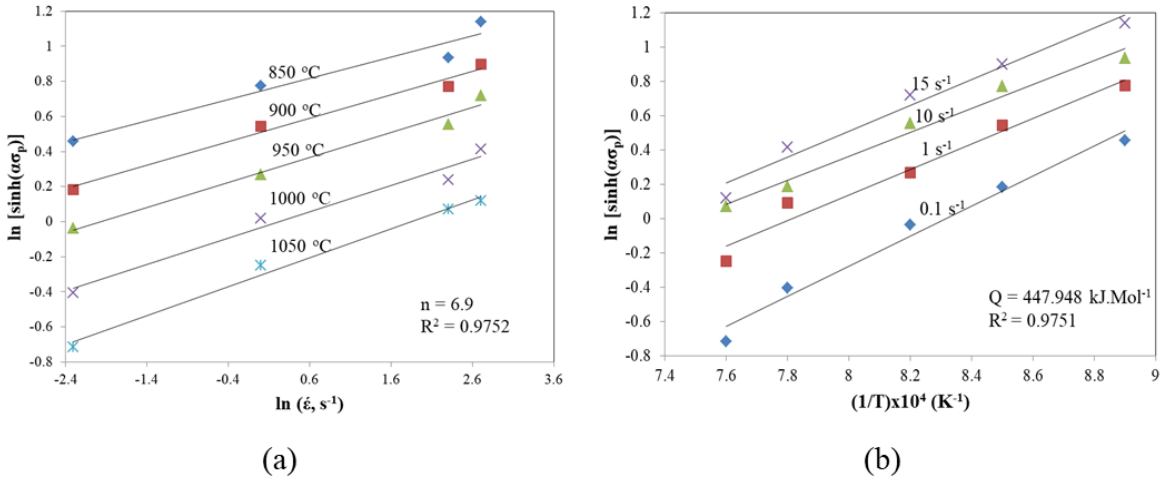

Figure 6.27: Plot of ln [sinh($\alpha\sigma_p$)] against (a) ln (strain rate) (b) 1/T, for the for the determination of n and Q, respectively.

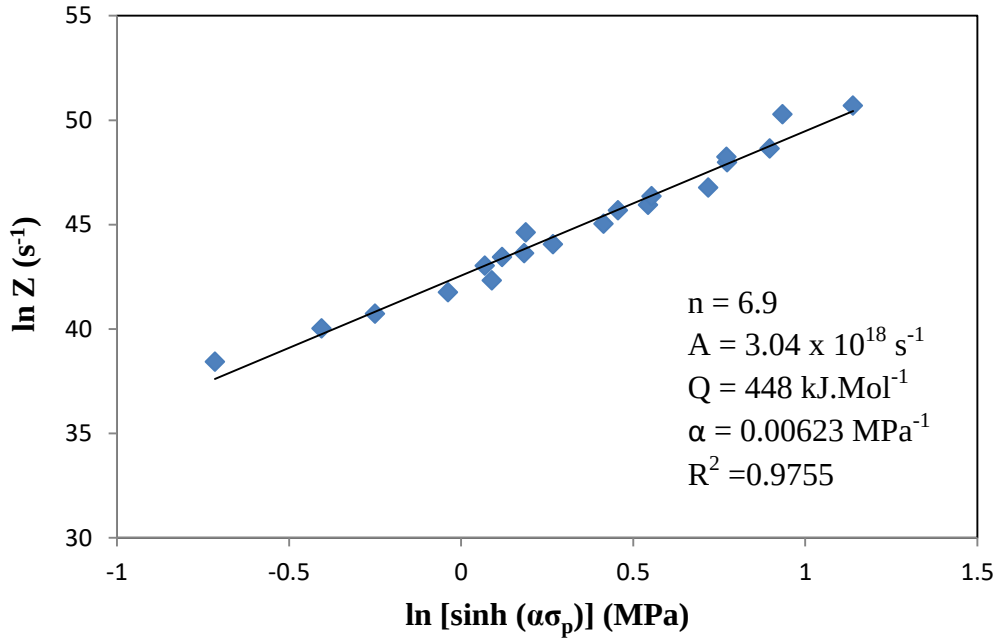

Figure 6.28: Regression analysis of the relationship between peak stress and the Z parameter according to the hyperbolic sine function for α = 0.00623 MPa^{-1}.

According to the hyperbolic-sinh equation the saturation stress σ_{sat} ($d\sigma/d\varepsilon = 0$) is given by [188]:

$$\sigma_{sat} = \frac{1}{0.00623} ln\left\{\left(\frac{Z}{3.04\ X10^{18}}\right)^{1/6.9} + \left[\left(\frac{Z}{3.04\ X10^{18}}\right)^{2/6.9} + 1\right]^{1/2}\right\}$$

6.6.2 Processing Maps

The processing maps obtained in the work hardening region of hot working (i.e. $\varepsilon < \varepsilon_p = 0.3$), are shown in Figure 6.29. Thus the two processing maps are for strains of 0.1 and 0.2, respectively. The efficiency of power dissipation is indicated by the contour numbers and the instability domains (where values $\xi(\dot{\varepsilon}) < 0$) are indicated by shaded regions. A change in strain does not have much effect on the peak efficiency of the power dissipation (η). Two domains having equal peak efficiencies were observed at each strain; 43% and 42% for 0.1 and 0.2 strains, respectively. High efficiency of power dissipation is usually associated with microstructural changes beneficial to hot deformation such as DRV and DRX [189]. On the other hand, a high efficiency of power dissipation could alternatively be a result of unstable flow which can be manifested as cracks and/or deformation bands [165], [190]. Thus, analysis of the processing maps is done in combination with the microstructural observations.

Microstructural observations from EBSD, Figure 6.16, show an increase in low angle grain boundaries (LAGB) with strain and no change in phase fraction in this region. Hence the peak efficiencies observed at temperatures of approximately 900 ^{o}C and 1000 ^{o}C, and strain rates of 2 -3 s^{-1} at both strains (0.1 and 0.2), are attributed to DRV. At high strain rates ($\dot{\varepsilon} > 5$ s^{-1}), low and negative efficiency values are observed, in addition to flow instability (shaded areas) and this can be attributed to the rate at which the dislocations are generated surpassing the DRV rate and hence the build-up of deformation energy.

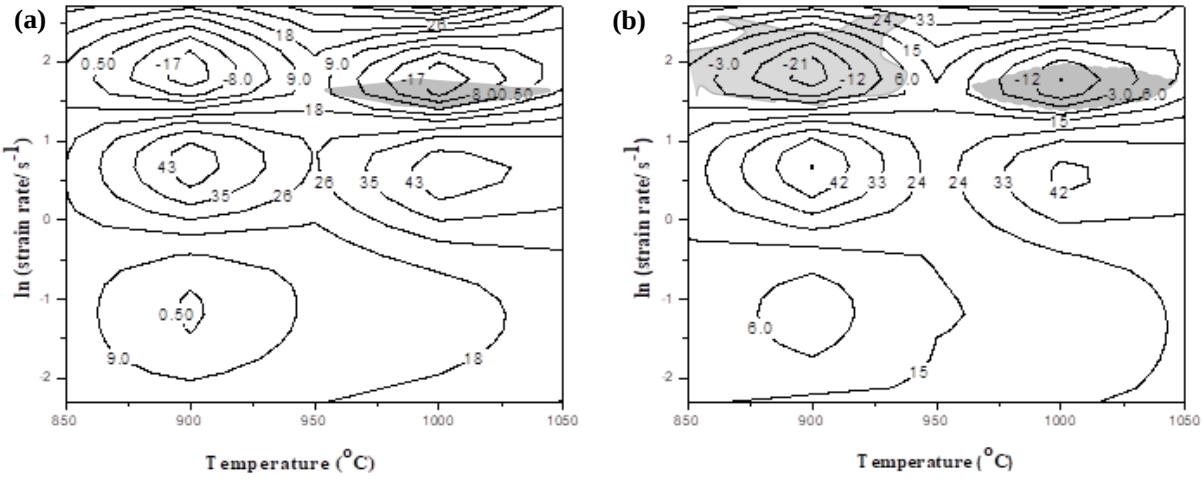

Figure 6.29: Processing maps for 2304 LDSS at a true strain value of: (a) 0.1 and (b) 0.2.

Figures 6.29 (a) – (d) show the processing maps for the 2304 LDSS deformed at the strain of 0.3, 0.4, 0.5 and 0.6, respectively. The strain of 0.3 is considered as the peak (approximately). The peak efficiency in the two domains A and B, in the work hardening region up to the peak strain show a slight change indicating that the power dissipation mechanism is most likely still DRV. The regions of instability are still the same.

At a strain of 0.4 and 0.5 peak efficiencies are still comparable to those of strains below the peak strain (ε =0.3) for domain A. The peak efficiency however increases sharply to 51 % at a strain of 0.6 when compared to lower strains where it is approximately 43 %, throughout. For domain B, the peak efficiency however continues to vary. The regions of where the efficiency of power dissipation is negative are invariant with strain and constantly coincide with regions of unstable flow. Though negative values of efficiency are observed at a strain of 0.5, the absence of the region of unstable flow ($\xi(\varepsilon) < 0$) at this strain is intriguing. According to microstructural observations, dynamic transformation was observed at strains close to the peak strain and above and confirmed by EBSD analysis as shown in Figure 6.16.

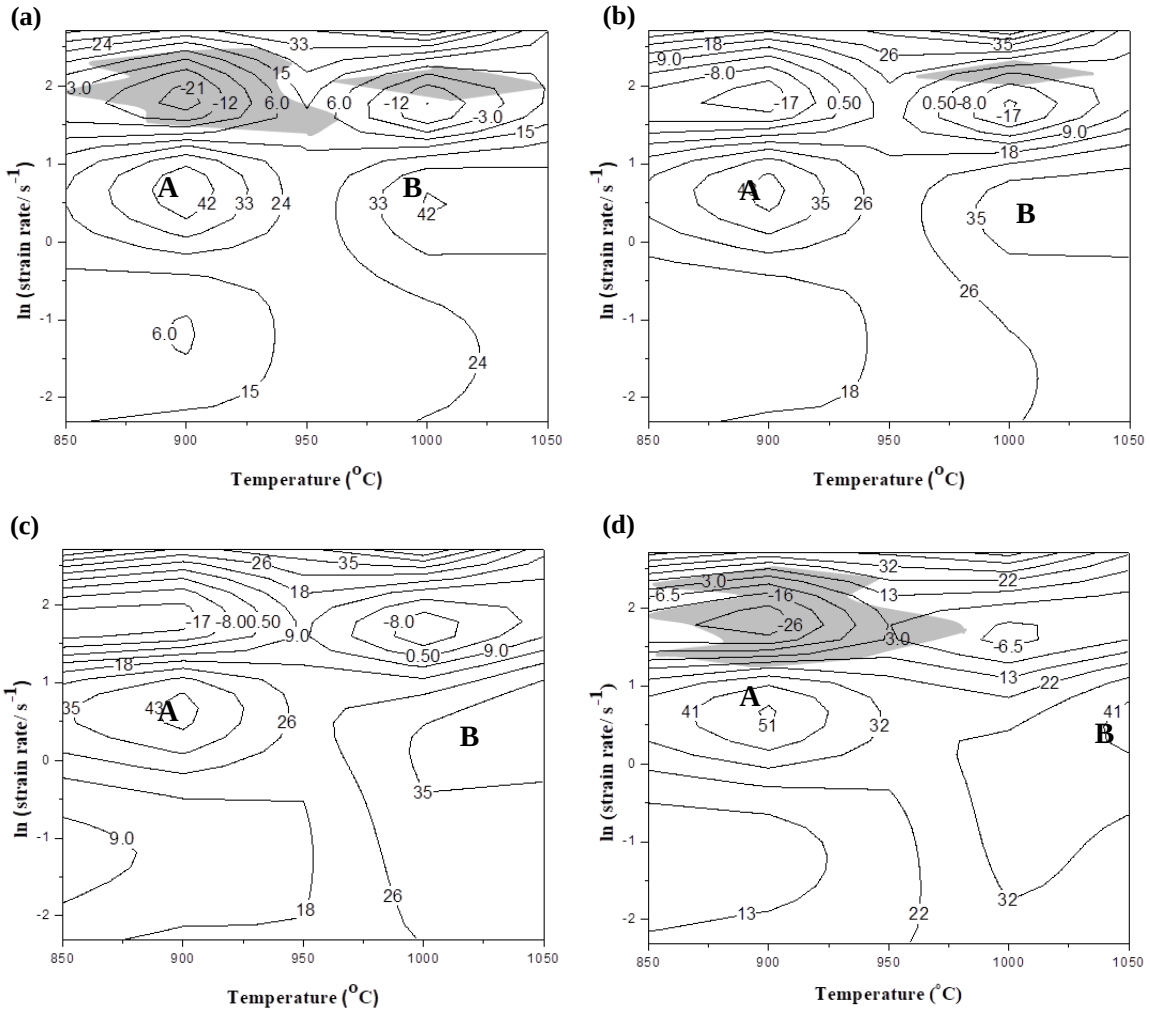

Figure 6.30: Processing maps for 2304 LDSS at true strain values of: (a) 0.3 (b) 0.4 (c) 0.5 (d) 0.6.

The industrial strain rates and strains ranges in the Steckel rolling mill are between 11 and 35 s^{-1} and 0.1- 0.3, respectively. Considering the processing maps in Figures 6.29 and 6.30, the minimum strain rate value is given by the natural logarithmic strain value of approximately 2.4, and the rolling temperatures are in the range of 900 and 1000 ^{o}C, as indicated in the mill logs (Appendix 6). According to the process maps, the ideal hot rolling temperature window for the Steckel mill was found to be between 950 and 1000 ^{o}C. This is the temperature region where high strain rates can be applied without the risk of flow instability. The peak efficiency in this region was found to be reasonably high, *i.e.* around 33 %, which means good restoration mechanisms are still at play.

Chapter 7

7.1 Discussion

The flow curves showed two distinct regions: region I and region II. Region I is characterized by two competing processes, i.e. work hardening (WH) and dynamic recovery (DRV) until a momentary balance is achieved where $d\sigma/d\varepsilon = 0$. In this case it is assumed to coincide with the peak. Region II is characterized by softening which can be observed as a drop in stress and microstructural analysis shows an increase in the austenite phase fraction in this region. The increase in the austenite phase fraction takes place in a strain-induced boundary migration (SIBM) manner, where the lesser strained (low dislocation density) austenite moves over the interface into more strained (high dislocation density) ferrite. In other words, the dislocation density difference between the two phases acts as the driving force for the migration of the austenite phase boundary into ferrite, thereby lowering the free energy of the system and consequently increasing the austenite phase fraction. This concept is further elaborated in Appendix A5.1.

7.1.1 Region I: Strain Hardening Modelling

Modelling the flow behaviour is done by considering the two competing processes in this region and employing the relevant equation. The Bergstrom model and the rule of mixtures could have been ideally adopted in this region, however due to not having single phase equivalent steels of the given composition as in DSS, the Bergstrom model [82] was rendered invalid. The Estrin-Mecking model equation [3-18] (already covered in the literature) was thus adopted. The constants to be determined are σ_{sat} and B. These were determined from the plot of $\sigma\theta$ against σ^2 as demonstrated in Appendix 4. The value of B was determined to be 5.3 and σ_{sat} as given in table 7.1. Using the Estrin-Mecking model, the flow behaviour in the work hardening and dynamic recovery regime was reasonably predicted as shown in Figure 7.1. The model was extended to beyond the peak strain showing its limitations beyond the region mentioned. In the WH region (region I) in which the Estrin-Mecking model is applied, no dynamic transformation was taken into account since no phase fraction changes were observed from microstructural analysis. This is true for all strains below the peak strain. The only change taking place at that moment being the amount of the dislocations being introduced into the material (Figure 6.15). As the dislocation density evolves so does the work hardening behaviour of the material, hence the Estrin-Mecking model can be applied up to a peak strain with good prediction. The better fit of the E-M model at lower temperatures

than at higher temperatures is interesting. This is evidence that the work hardening is indeed strongly dependent on i.e. higher temperature promotes more dislocation annihilation or restoration thereby lowering the accumulated strain. This enables deformation to take place at lower stress, and the opposite being true at a lower temperature.

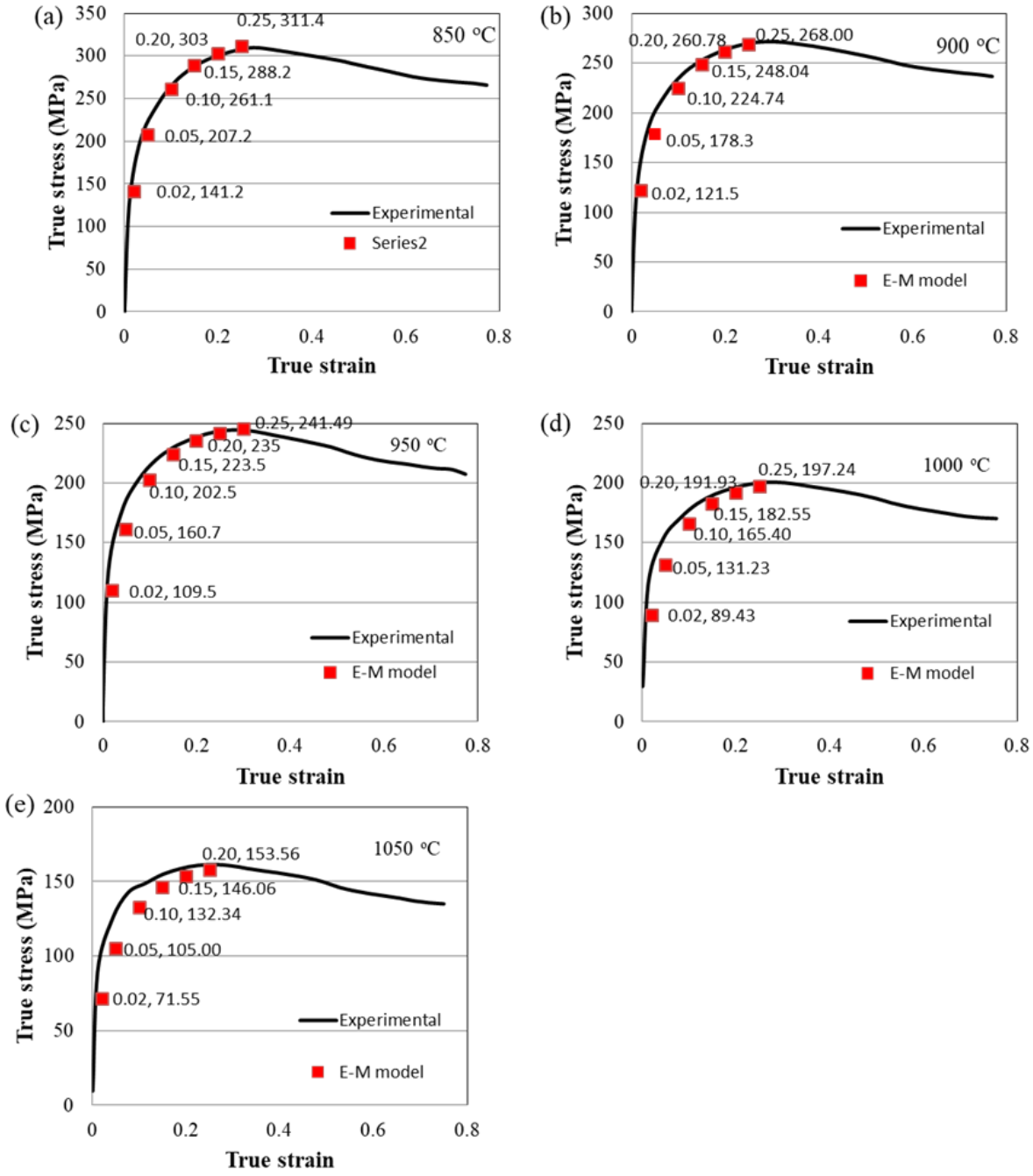

Figure 7.1: Comparison of flow stress curves plotted using the Estring-Mecking (E-M) model and the experimental data.

Table 7.1 below, shows the saturation stress σ_{sat} values obtained from the hyperbolic sinh equation (SH), the Kock-Mecking (KM) and Estrin-Mecking (EM) approach for deformation at a strain rate of 15 s^{-1}. The SH and KM approaches show fairly close values of saturation stress for the given conditions, except at 950 ^{o}C, where the discrepancy is significant. While the sine-hyperbolic function approach assumes that the structural factor "A" is constant, the other two take into account the dislocation storage and annihilation [95], [151], [188]. The SH and the KM approaches showed close saturation stress (σ_{sat}) values while those from the EM model were slightly higher than the two.

Table 7.1: Comparison of the σ_{sat} values from the hyperbolic-sine (SH) function, Kocks-Mecking (KM) and Estrin-Mecking (EM)) approach at different temperatures and a strain rate of 15 s^{-1}

Temp (^{o}C)	σ_{sat} (SH)	σ_{sat} (KM)	σ_{sat} (EM)
850	315	310	323
900	269	268	278
950	228	244	251
1000	193	199	205
1050	162	161	164

7.1.2 Region II: Flow softening

This region is characterized by a drop in stress with an increase in strain, and starts after the peak strain. Since recovery in the high SFE phase (ferrite) does not cause softening, the observed fractional softening was attributed to recrystallization in the low SFE phase (austenite). That is to say, the fractional softening and the recrystallized fraction can be assumed to be numerically the same [191]. Thus instead of physically quantifying the recrystallized fraction through microstructural analysis to find the fractional softening, the flow curves where steady state was attained were used instead by employing equation [3-20]. The dynamic fractional softening in this region was determined by the Avrami type equation (equation [3-21]) where the values of r_c and q were found to be 8.9 and 1.7, respectively, Figure A5.1 in Appendix 5.

Modelling the softening region beyond the peak using the Avrami equation, was successful despite the dynamic transformation taking place. It has previously been shown that as the dual phase material is further strained, strain localization takes place, with more strain being transferred to austenite with an increase in strain. The diffusion coefficient of ferrite is higher than that of austenite making dislocation movement easier in ferrite than in austenite. The high dislocation mobility in ferrite makes recovery easy. On the contrary, the low dislocation mobility in austenite ensures strain accumulates until DRX is triggered. Ferrite will either have recovered or remains still work hardened at the moment while austenite undergoes DRX. As the dislocation density in the ferrite will be higher than in the austenite where recrystallization has taken place, the difference in the dislocation density across the ferrite-austenite boundary results in the austenite phase front advancing into ferrite through strain induced boundary migration (SIBM). This lowers the strain energy (dislocation density) of ferrite, thus softening it and at the same time results in an increase of the austenite phase fraction. In support of this theorem, is the work by Wang *et al.* [131] which showed that when a dual phase material is deformed at a higher strain rate, the extent of the strength increase of ferrite is much greater than that of austenite. The study [131] attributed this to the strain rate sensitivity of ferrite being more than that of austenite, resulting in a higher strength increase in ferrite than in austenite. It can thus be concluded that at an inter-critical (two-phase) deformation at a high strain rate, a harder ferrite and softer austenite coexist. Hence, the observed flow softening as the austenite advances into the ferrite and the austenite volume fraction increases.

7.1.3 Coupling the E-M model to the Avrami model

Equations [3-18], for $\varepsilon < \varepsilon_p$ and [3-23] , for $\varepsilon > \varepsilon_p$ describe the flow behaviour for the WH+DRV regime (from the E-M model) and for the flow softening after the peak (from the Avrami model) respectively. These two models were coupled to represent their respective regimes.

In the flow stress above the peak strain (ε_p), the corresponding value of stress at a strain without softening $\sigma^{E\text{-}M}$ was used instead of σ^{sat} as it was observed that the saturation stress was not instantaneously attained at a strain beyond the peak strain but gradually approached the latter. Coupling equations [3-18] and [3-23] the overall flow behaviour of the steel

deformed at 15 s^{-1} for the temperature range of 850 ^{o}C to 1050 ^{o}C was modelled with reasonable accuracy as shown in Figure 7.2.

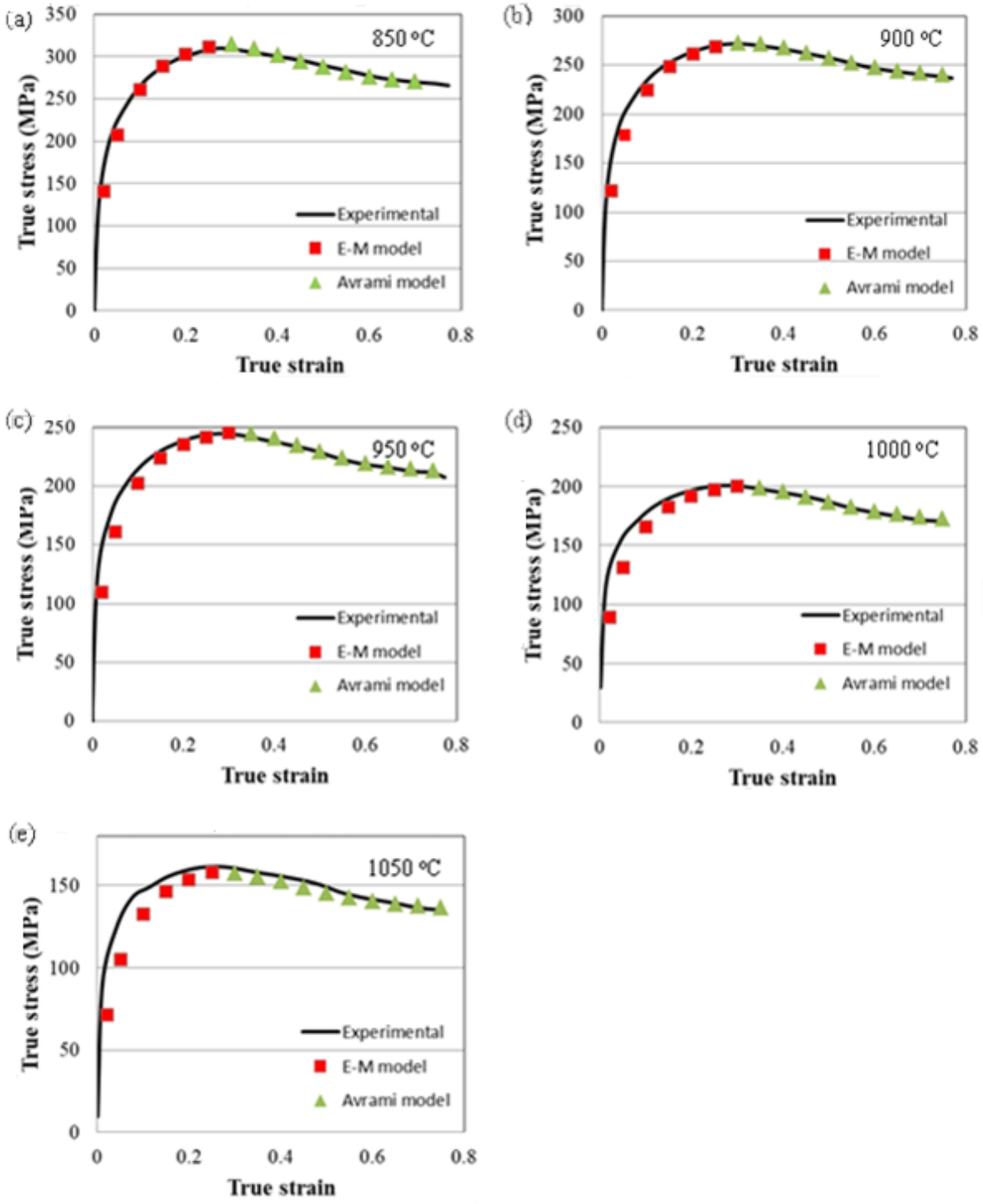

Figure 7.2: Coupled Estrin-Mecking model and Avrami model for flow stress modelling at a 15 s^{-1} strain rate.

For the temperature range investigated (850 – 1050 ^{o}C), the strain rate and strain were limiting factors. Beyond a strain of 0.6 up to 0.8, no significant change in volume fraction of austenite was observed. It can be said that at strains of 0.6 and beyond, the volume fraction tends to be constant. This can be attributed to the lowering of the dislocation density between austenite and ferrite as softening in austenite approaches the steady state (due to completion of DRX). The other reason is that the LAGBs in ferrite would likely have evolved into HAGBs at such high strains, giving rise to CDRX in ferrite which also reduces the $\Delta\sigma$ dislocation density, hence minimizing the driving force and ceasing of further transformation. Likewise, at strain rates of 10 s^{-1} and above, the volume fraction remained fairly constant.

Substantial softening was observed during deformation of the steel, and according to a number of authors [9], [11], [54], is a result of DRX of the austenitic phase. EBSD results do confirm that the austenitic phase did undergo DRX, with some grains in austenite showing bulging or a finger-like structure characteristic of DRX [115], [116], [117], [118], [192].

7.1.4 Implications of these findings on in-plant Steckel Mill operations

Figure 7.3 shows the comparison of MFS from the plant calculated using the Sims equation versus predicted MFS from the current work (Appendix 6) for the WH only or WH+DRV *i.e.* up to peak strain which is typical for in-plant Steckel mill strains of up to about 0.3. As may be seen, there is a good agreement between them and both the MFS increase with an increase in the Zenner-Hollomon parameter. This also indicates that the apparent activation energy of Q = 448kJ/mol which was determined from the current study, is representative of the actual activation energy of the hot working process of this steel although slight adjustments might be needed in 1st and 2nd passes where the in-plant MFS is slightly lower than the predicted MFS. No retained strain was taken into account in this work and, therefore, the good agreement between the predicted and plant MFS can only be attributed to the fact that the reverse rolling Steckel mill experiences relatively longer interpass times during which recovery takes place.

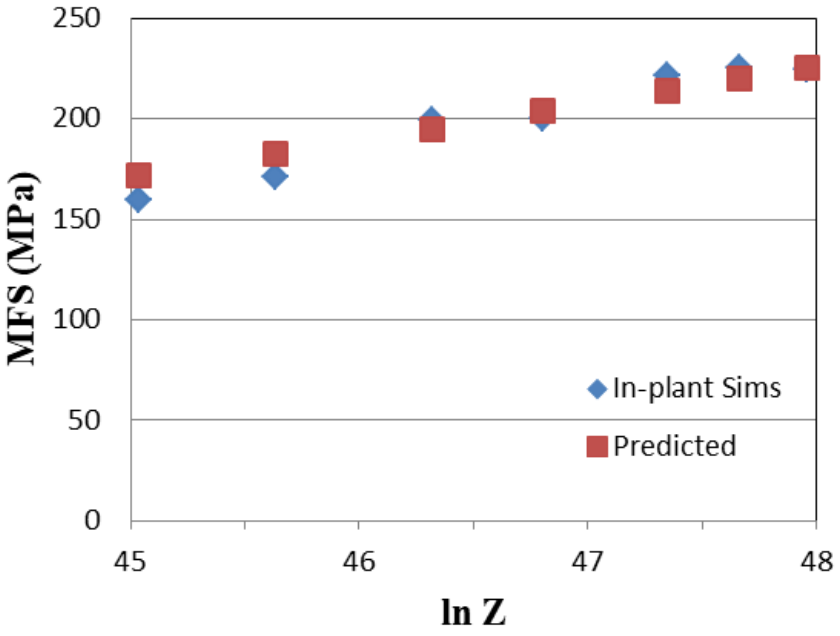

Figure 7.3: Variation of MFS with ln Z in-plant and predicted up to peak strain, i.e. up to a strain of 0.3.

Chapter 8

8.1 Conclusions

The influence of the process parameters on the hot deformation behaviour of 2304 LD stainless steel was successfully studied in this work and the following conclusions are made:

1. Increasing the strain rate and lowering the temperature, increases the dislocation density difference between the austenite and ferrite. Though this condition may increase DRX in austenite due to more stored energy, DRV in ferrite becomes less efficient leading to dislocation density difference that causes dynamic transformation of austenite through SIBM. Hence the observed increase in the volume fraction of austenite beyond the peak strain is attributed to SIBM of an austenite front into ferrite.
2. The mean flow stress (MFS) values of the in-plant rolling calculated using the Sims equation agree with those predicted using the Estrin-Mecking model coupled with the Avrami model. This implies that the various constants determined in this study can be relied upon for dual phase stainless steel of similar composition
3. Strain accumulation has the possibility of increasing the austenite volume fraction in-plant, however the long interpass times and average high temperatures in the Steckel mill may annul strain accumulation and hence possible increase in austenite volume fraction.
4. The temperature of 950 ^{o}C and above is proposed for the hot rolling of the 2304 LD stainless steel at high strain rates typically used in the Steckel mill without any flow instabilities arising.

8.2 Recommendations for future work

1. SIBM and hence the phase transformation in the current study has been attributed to the strain energy difference resulting from different dislocation densities in the two phases (austenite and ferrite). A comprehensive study using transmission electron microscopy (TEM) is highly recommended in order to have an in-depth knowledge on how dislocations evolve during deformation and can be correlated to the phase transformation in the studied material.
2. The volume fraction change with strain was analysed for one temperature and strain rate. Future work can also evaluate changes in the volume fraction with strain at other temperatures and strain rates. The analysis can be used to build-up a model correlating the change in austenite volume fraction with strain, strain rate and temperature.

3. Changes in the equilibrium volume fraction of austenite with temperature were not as high as predicted by Thermocalc. The equilibrium austenite volume fraction predicted by Thermocalc was equivalent to that obtained after substantial dynamic transformation had taken place during deformation. Thus equilibrium phase fraction measurements using Thermocalc showed that the phase fractions in this steel are affected by other constituents within the material that are not covered by Thermocalc.

References

[1] TMR. Stainless, “Practical guidelines for the fabriacation of duplex stainless steel,” International Molybdenum Association, London, UK, 2014.

[2] M. Maalekian, “The effects of alloying elements on steels (I),” *Christian Doppler Laboratory for Early Stages of Precipitation,* pp. 1-31, October 2007.

[3] R.W.K. Honeycombe and H.D.K.H. Bhadeshia, Steel microstructure and properties, London: Butterworth-Heinemann, 1995, p. 336.

[4] A.C.T.M. Van Zwieten and J.H. Bulloch, “Some considerations on the toughness properties of ferritic stainless steels - A brief review,” *Journal of Pressure Vessels and Piping,* vol. 56, pp. 1-31, 1993.

[5] I. Alvarez-Armas, “Duplex stainless steels : brief history and some recent alloys,” *Recent Patents on Mechanical Engineering 1,* pp. 51-57, 2008.

[6] J. Olsson and M. Snis, “Duplex- a new generation of stainless steels for desalination,” *Desalination,* vol. 205, pp. 104-113, 2005.

[7] G. Martin, “Hot workability of duplex stainless steels,” PhD Thesis , 2011.

[8] H. Farnoush, A. Momeni, K. Dehghani, A.-M. J and H. Keshmiri, “Hot deformation characteristics of 2205 duplex stainless steel based on the behavior of constituent phases,” *Materials and Design 31,* pp. 220-226, 2010.

[9] T. Chandra, B. D. and D. Dunne, “Hot working of a duplex stainless steel,” in *Proceeding ICSMA 6,* Melbourne, Australia, 1982.

[10] A. Paul, J.L. Martos and R. Sanchez, “Innovation stainless steel, AIM,” Italy, 1993.

[11] M. Barteri, E. Evangelista and M. Niewwezas, “Innovation stainless steel, AIM,” Florence, Italy, 1993.

[12] H. Unkel, “The relationship between the mechanical properties and the structure of two-phase alloys,” *Metallurgical Technology,* vol. 5, pp. 146-150, 1951.

[13] S. Ankem and H. Margolin, “A rationalization of stress-strain behaviour of two-ductile phase alloys,” *Metallurgical Transactions,* vol. 17A, pp. 2209-2226, 1986.

[14] S. Ankem and H. Margolin, “Finite element method (FEM) calculations of stress-strain behaviour of alpha-beta Ti-Mn alloys: Part II. Stress and strain distribution,”

Metallurgical Transactions 13A, pp. 592-605, 1982.

[15] S. Ankerm and H. Margolin, "Modeling deformation in two-phase alloys," *Journals of Metals* , pp. 25-29, 1986.

[16] D. Smith, Interviewee, *Personal Communication.* [Interview]. 2013.

[17] J.C. De Lacerda, L.C. Candido and L.B. Godefroid, " Effect of volume fraction of phases and precipitates on the mechanical behaviour of UNS S31803 duplex stainless steel," *International Journal of Fatigue 74* , pp. 81-87, 2015.

[18] G.E. Dieter, H.A. Kuhn and S.L. Semiathin, Handbook of workability and process design, Ohio: The Materials Information Society, 2003, p. 414.

[19] C. Devadas and J.V. Samarasekera and E.B. Hawbolt, "The thermal and metallurgical state of steel strip during hot rolling: Part III. Microstructural evolution," *Metallurgical Transactions,* vol. 22A, pp. 335-349, 1991.

[20] S. Bayoumil, "A kinematic analytical approach to predict roll force, rolling torque and forward slip in thin hot strip continuous rolling," *Iron and Steelmaking,* vol. 34, pp. 444-448, 2007.

[21] P. Biswas and N.R. Mandal, "Simulation of thermo-mechanical deformation in high speed rolling of long steel products," Worcester, 2003.

[22] S.Z. Chen, D.H. Zhang, J. Sun, J.S. Wang and J. Song, "Online calculation model of rolling force for cold rolling mill based on numerical integration," in *Proceeding of the Control and Decision Conference,* Taiyuan, 2012.

[23] H. Ford and J.M. Alexander, "Simplified hot rolling calculations," *Journal of Institute of Metals* , vol. 92, pp. 397-404, 1964.

[24] M.S. Joun and S.M. Hwang, "An approximate analysis of hot strip-strip rolling - A new approach," *International Journal of Mechanical Sciences,* vol. 34, pp. 985-998, 1992.

[25] A. Said, J.G. Lenard, A.R. Ragab and M.A. Elkhier, "The temperature, roll force and roll torque during hot bar rolling," *Journal of Materials Processing Technology,* vol. 88, pp. 147-153, 1999.

[26] R.B. Sims, "The calculation of roll force and torque in hot rolling mills," in *Proceedings of the Institution of Mechanical Engineers*, 1954.

[27] J. Yanagimoto, T. Morimoto, R. Kurahashi and I. Chikushi, "Mathematical modelling for rolling force and microstructure evolution and microstructure controlling with

heavy reduction in tandem hot strip rolling," *Steel Research,* vol. 73, pp. 56-62, 2002.

[28] J.G. Lenard, Metal forming science and practice, Oxford: Elsivier, 2002.

[29] C.M. Sellars, "The physical metallurgy of hot working," in *Proceedings of International Conference on Hot Working and Forming Processes*, London, 1980.

[30] J.H. Beynon, P.R. Brown, S.I. Mizban, A.R.S. Ponter and C.M. Sellars, "Inclusion of metallurgical developments in modelling of industrial hot rolling of metals," in *Proceeding of NUMIFORM Conference ,* Gothenburg, 1986.

[31] C.M. Sellars and J.A. Whiteman, "Recrystallization and grain growth in hot rolling," *Metallurgical Science,* pp. 187-194, 1979.

[32] C.M. Sellars, "Computer modelling of microstructural evolution during hot rolling," in *International Conference on Physical Metallurgy of Thermomechanical Processing of Steels and Other Metals, THERMEC 88*, Tokyo, 1988.

[33] H. Yada, "Prediction of microstructural changes and mechanical properties in hot strip rolling," in *Proceedings of International Syposium on Accelerated Cooling of Rolled Steel, Conference of Metallurgists,* Winnipeg, 1988.

[34] T. Senuma and H. Yada, "Annealing processes, recovery, recrystallization and grain growth," in *Proceedings of the 7th Riso International Symposium on Metallurgy and Materials Science ,* Roshilde, 1986.

[35] M. Suehiro, K. Sato, Y. Tsukano, H. Yada, T. Senuma and Y. Matsumura, "Computer modelling of microstructural change and strength of low carbon steel in hot strip rolling," *Iron and Steel Institute of Japan,* vol. 27, pp. 439-445, 1987.

[36] Y. Saito, T. Enami and T. Tanaka, "The mathematical model of hot deformation resistance with reference to microstructural changes during rolling in plate mill," *Trans. Iron and Steel Institute of Japan,* vol. 25, pp. 1146-1155, 1985.

[37] C. Perdrix, "Characteristic of plastic deformation of metals during hot working," Saint Germainen-Laye, 1987.

[38] M. Bagheripoor and H. Bisadi, "An investigation on the roll force and torque fluctuations during hot strip rolling process," *Production and Manufacturing Research,* vol. 2, pp. 1218-141, 2014.

[39] M.J. Luton and C.M. Sellars, "Dynamic recrystallization in nickel and nickel-iron alloys during high temperature deformation," *Acta Metallurgica,* vol. 17, pp. 1033-1041, 1969.

[40] H.J. McQueen and S. Bergerson, “Dynamic recrystallization of copper during recrystallization,” *Metals Science,* vol. 6, pp. 25-29, 1972.

[41] L. Backe, “Modelling the microstructural evolution during hot deforamtion of microalloyed steels,” 2009.

[42] J. Pittner and M. Simaan, “Controller for improving the quality of the tandem rolling of hot rolled metal strip,” in *American Control Conference,* Baltimore, 2010.

[43] L. Collins, “Processing of Niobium containg steels by steckel mill rolling,” IPSCO Internal report, 2002.

[44] W.J. Cobo and W.M., “Factors affecting development of oxide scales on austenite steels during hot rolling in steckel mills,” *Metallurgical and Materials Transactions,* vol. 39A, pp. 1-9, 2008.

[45] C.G. Rhodes and A.W. Thompson, “The composition dependence of stacking fault energy in austenitic stainless steels,” *Metallurgical Transactions,* vol. 8A, pp. 1901-1906, 1977.

[46] R.E. Schramm and R.P. Reed, “Stacking fault energies of austenitic stainless steels,” *Metallurgical Transactions,* vol. 6A, pp. 1345-1351, 1975.

[47] C.C. Bamptyon, I.P. Jones and M.H. Loretto, “Stacking fault measurements in some austenitic stainless steels,” *Acta Metallurgica,* pp. 39-51, 1978.

[48] F. Siciliano Jr and J.J. Jonas, “Mathematical modeling of the hot strip rolling of microalloyed Nb, multiplyalloyed Cr-Mo, and plain C-Mn steels,” *Metallurgical and Materials Transactions,* vol. 31A, pp. 511-529, 2000.

[49] A.D. Freed, S.V. Raj and K.P. Walker, “Stress versus temperature dependent activation energies in creep,” in *3rd International Conference on Constitutive Laws for Engineering Materials: Theory and Applications and Workshop on Innovative Use of Materials in Industrial and Infrastructure Design and Manufacturing*, Arizona, 1991.

[50] H.J. McQueen and J.J. Jonas, “Recent advances in hot working fundamental dynamic softening mechanisms,” *Journal of Applied Metal Working,* vol. 3, pp. 233-241, 1984.

[51] A. Iza-Mendia, A. Pinol-Juez, J.J. Urcola and I. Gutierrez, “Microstructural and mechanical behavior of a duplex stainless steel under hot working conditions,” *Metallurgical and Materials Transactions A,* pp. 2975-2985, 1998.

[52] P.L. Mao, K. Yang and G.Y. Su, “Hot deformation behaviour of an as-cast duplex stainless steel,” *Journal of Materials Science and Technology 19,* pp. 379-381, 2003.

[53] E. Evangelista, H.J. McQueen, M. Niewczas and M. Cabibbo, “Hot workability of 2304 and 2205 duplex stainless steels,” *Canada Metallurgical Quarterly: The Canadian Journal of Metallurgy and Materials Science 43,* pp. 339-353, 2004.

[54] P. Cizek and B. Wynne, “A mechanism of ferrite softening in a duplex stainless steel deformed in hot torsion,” *Materials Science and Engineering,* vol. 230A, pp. 88-94, 1997.

[55] A. Mohamadizadeh, A. Zarei-Hanzaki and S. Mehtonen, “Correlation of strain accommodation factor with the state of microsctructural components in a multiphase steel,” *Iron and Steel Institute of Japan International,* vol. 55, pp. 2406-2415, 2015.

[56] M.R. Barnett and J.J. Jonas, “Distinctive aspects of the physical metallurgy of warm rolling,” *ISIJ International 39,* pp. 856-873, 1999.

[57] J.P. Hirth and J. Lothe, Theory of dislocations, Florida: Krieger Piblishing Company, 1982, p. 857.

[58] R. Sandstrom and R. Lagneborg, “A model for hot working occuring by recrystallization,” *Acta Metallurgica,* vol. 23, pp. 387-398, 1975.

[59] R. Abbaschian, L. Abbaschian and R. Reed-Hill, Physical Metallurgy Principles 4th Edition, Cengage Learning , 2009, p. 769.

[60] E. Denstova, “Understanding of edge and screw dislocations in nanostructures by modeling simulations,” PhD Thesis , 2013.

[61] H.J. Frost and M.F. Ashby, Deformation-mechanism maps: the plasticity and creep of metals and ceramics, Oxford: Pergamon Press, 1982.

[62] S. Mehtonen, “The behaviour of stabilized high-ghromium ferritic stainless steels in hot deformation,” PhD Thesis, 2014.

[63] F.J. Humphreys and M. Hatherly, Recrystallization and related annealing phenomena, Elsevier Ltd, 2004, p. 605.

[64] H.D. Solomon and T.M. Devine Jr, Duplex Stainless Steels – A tale of two phases, ASM, Metals Park, OH, 1982, pp. pp. 693-756.

[65] J.O. Nilsson, “Super duplex stainless steels,” *Materials Science and Technology 8* , pp. 685-700, 1992.

[66] J. Johannson and M. Oden, “Load sharing between austeniute and ferrite in duplex stainless steel during cyclic loading,” *Metallurgical and Materials Transactions 31A,*

pp. 1557-1570, 2000.

[67] W.O. Balancin, A.M. Hoffman and J.J. Jonas, "Influence of microstructure on the flow behaviour of duplex stainless steels at high temperatures," *Metallurgical and Materials Transactions 31A,* pp. 1353-1364, 2000.

[68] J. Duprez, B.C. De Cooman and N. Akdut, "Flow stress and ductility of duplex stainless steel during high-temperature torsion deformation," *Metallurgical and Materials Transactions A,* vol. 33, pp. 1931-1937, 2002.

[69] A. Momeni, K. Dehghani and G. Ebrahimi, "Modelling the initiation of dynamic recrystallization using dynamic recovery model," *Journal of Alloys and Compounds,* vol. 509, pp. 9387-9393, 2011.

[70] A. Momeni, K. Deghani, G.R. Ebrahimi and S. Kazemi, "Developing the processing maps using the hyperbolic sine constitutive equation," *Metallurgical and Materials Transactions A,* pp. 1-10, 2013.

[71] A. Momeni, S. Kazemi and A. Bahran, "Hot deformation behaviour of microstructural constituents in a duplex stainless steel during high-temperature straining," *International Journal of Minerals, Metallurgy and Materials 20,* pp. 953-960, 2013.

[72] S. Neti, M.N. Vijayshanka and S. Ankem, "Finite element method modeling of deformation behaviour of two-phase materials part I: stress-strain relations," *Materials Science and Engineering,* vol. 145A, pp. 47-54, 1991.

[73] K. Cho and J. Gurland, "The law of mixtures applied to the plastic deformation of two-phase alloys of coarse microstructures," *Metallurgical Transactions,* vol. 19A, pp. 2027-2040, 1988.

[74] I. Tamura, Y. Tomota and H. Ozawa, "Proceedings of the 3rd international conferennce on strength of metals and alloys," in *Institute of Metals and Iron and Steel Institute,* London, 1973.

[75] H. Fischmeister and B. Karlsson, "Plastizitatseigenschaften grob-zweiphasiger Werkstoffe., 68," *Zeitschrift für Metallkunde,* vol. 68, pp. 311-327, 1977.

[76] A. Dehghan-Manshadi and R.J. Dippenaar, "Strain-induced phase transformation during thermo-mechanical processing of titanium alloys," *Materials Science and Engineering,* vol. 552, pp. 451-456, 2012.

[77] H. Dong and X. Sun, "Deformation induced ferrite transformation in low carbon steels," *Current Opinion in Solid State and Materials Science 9,* pp. 269-276, 2005.

[78] L.E. Murr, K.P. Staudhammer and S.S. Hecker, “Effects of strain state and strain rate on deformation-induced transformation in 304 stainless steel: Part II. Microstructural study.,” *Metallurgical Transactions,* vol. 13A, pp. 627-635, 1982.

[79] E. Nes, “Modelling of work hardening and stress saturation in FCC metals,” *Progress in Materials Science 41,* pp. 129-193, 1998.

[80] A. Laasraoui and J.J. Jonas, “Prediction of steel flow stresses at high temperatures and strain rates,” *Metallurgical Transactions ,* vol. 22A, pp. 1545-1557, 1991.

[81] J.M. Cabrera, A. Mateo, L. Llanes, J.M. Prado and M. Anglada, “Hot deformation of duplex stainless steels,” *Journal of Materials Processing Technology 143-144,* pp. 321-325, 2003.

[82] Y. Bergstrom and B. Aronsson, “The application of a dislocation model to the strain and temperature dependence of the strain hardening exponent n in the Ludwik-Hollomon relation between stress and strain in mild steels,” *Metallurgical Transactions 3A,* pp. 1951-1957, 1972.

[83] Y. Estrin and H. Mecking, “A unified phenomenological description of work hardening and creep based on one-parameter models,” *Acta Metallurgica 32A ,* pp. 57-70, 1984.

[84] A.M. Jorge Jr and O. Balancin, “Prediction of steel flow stresses under hot working conditions,” *Materials Research 8,* pp. 309-315, 2005.

[85] H.J. McQueen and D.L. Bourell, Formability and metallurgical structure, TMS, Warrendale, 1986, p. 383.

[86] C. Huang, “Flow stress, restoration and precipitation behaviour and modelling for two Ti-Nb stabilized IF steels in the ferrite region,” 1999.

[87] H.J. McQueen, N.D. Ryan, E. Evangelista and X. Xia, “Flow stress, grain and subgrain structures developed by hot working in as-cast 409 stainless steel, Proceedings of the 34th Mechanical Working Steel Processing Conference,” 1993.

[88] G.S. Reis, A.M. Jorge Jr and O. Balancin, “Influence of the microstructure of duplex stainless steels on their faailure characteristics during hot deformation,” *Materials Research 3,* pp. 31-35, 2000.

[89] F. Tehovnik, B. Arzensek, B. Arh, D. Skobir, B. Pirnar and B. Zuzek, “Microstructure evolution in SAF 2507 super duplex stainless steel,” *Materials and Technology 45,* pp. 339-345, 2011.

[90] X. Quelennec, N. Bozzolo, J.J. Jonas and R.E. Loge, “A new approach to modelling the flow curve of hot deformed austenite,” *Iron and Steel Institute of Japan International,*

vol. 51, pp. 945-950, 2011.

[91] J.J. Jonas, X. Quelennec, L. Jiang and E. Martin, "The Avrami kinetics of dynamic recrystallization," *Acta Materialia,* vol. 57, pp. 2748-2756, 2009.

[92] S.M. Byon, S.I. Kim and Y. Lee, "Predictions of roll force under heavy reduction hot rolling using a large-deformation constitutive model," *Journal of Engineering Manufacture B,* pp. 1-12, 2004.

[93] Y. Bergström, "The plastic deformation of metal. A dislocation model and its applicability," PhD Thesis, Stockholm, 1982.

[94] Y. Bergström, "A dislocation model for the stress-strain behaviour of polycrystalline α-Fe with special emphasis on the variation of the densities of mobile and immobile dislocations," *Materials Science and Engineering,* vol. 5, no. 4, pp. 193-200, 1970.

[95] U.F. Kocks, "Laws for work-hardening and low temperature creep," *Journal of Engineering and Materials Technology,* vol. 98, pp. 76-85, 1976.

[96] R. Ding and Z.X. Guo, "Coupled quantitative simulation of microstructural evolution and plastic flow during dynamic recrystallization," *Acta Materialia,* vol. 49, pp. 3163-3175, 2001.

[97] H.S. Zurob, C.R. Hutchinson, Y. Brechet and G. Purdy, "Modeling recrystallization of microalloyed austenite: effect of coupling recovery, precipitation and recrystallization," *Acta Materialia,* vol. 50, pp. 3075-3092, 2002.

[98] Y.B. He, Q. Pan, Q. Chen, Z.Y. Zhang, X. Liu and W. Li, "Modeling of strain hardening and dynamic recryallization of ZK60 magnesium alloy during hot deformation," *Transactions of Nonferrous Metals Society of China,* vol. 22, pp. 246-256, 2012.

[99] Z. Gronostajski, "New method of static softening kinetics determination," *Journal of Materials Processing Technology ,* Vols. 157-158, pp. 165-170, 2004.

[100] A. Oudin, R. Barnett and P. Hodgson, "Grain size effect of warm deformation behaviour of Ti-IF steel," *Journal of Materials and Engineering A,* vol. 367, pp. 282-294, 2004.

[101] S. Bellier and R. Doherty, "Structure of deformed aluminum and its recrystallization: investigation with transmission Kossel diffraction," *Acta Metallurgica et Materialia 25,* pp. 521-538, 1977.

[102] J.C.M. Li, "Possibility of subgrain rotation during recrystallization," *Journal of Applied*

Physics, vol. 33, pp. 2958-2965, 1962.

[103] M.R. Drury and F.J. Humphreys, "The development of microstructure in Al-5%Mg during high temperature deformation," *Acta Metallurgica,* vol. 34, pp. 2259-2271, 1986.

[104] D. Hardwick, C.M. Sellars and W.J. Tegart, "Structural changes during the deformation of copper, aluminium and nickel at high temperatures and high strain rates," *Journal of the Institute of Metals,* vol. 90, pp. 17-22, 1961.

[105] H.J. McQueen and J.J. Jonas, "Recovery and recrystallization during high temperature deformation," in *Plastic Deformation of Metals,* New York, Academic Press, 1975, p. 393.

[106] J.J. Jonas, C.M. Sellars and W.J. Tegart, "Strength and structure under hot-working conditions," *Metallurgical Review,* vol. 14, pp. 1-24, 1969.

[107] C.M. Sellars, "Recrystallization of metals during hot deformation," *Philosophical Transactions of the Royal Society,* vol. 288A, pp. 147-158, 1968.

[108] T. Sakai, "Dynamic recrystallization microstructures under hot working conditions," *Journal of Materials Processing Technology,* vol. 53, pp. 349-361, 1995.

[109] C. Zhang, "Mechanism of ferrite grain refinement in the ($\gamma + \alpha$) region of weathering steel Cu-P-Cr-Ni-Mo," *Journal of Materials Research,* vol. 30, pp. 2508-2515, 2015.

[110] T. Sakai, A. Belyakov, R. Kaibyshev, H. Miura and J. Jonas, "Dynamic and post-dynamic recrystallization under hot, cold and severe plastic deformation conditions," *Progress in Materials Science 60,* pp. 130-207, 2014.

[111] E.I. Poliak and J.J. Jonas, "Critical strain for dynamic recrystallization in variable strain rate hot deformation," *ISIJ International 43,* vol. 43, pp. 692-700, 2003.

[112] J. Jonas, C. Ghosh, X. Quelennec and V. Basabe, "The critical strain for dynamic transformation in hot deformed austenite," *ISIJ International 53,* vol. 53, pp. 141-151, 2013.

[113] A. Dehghan-Manshadi, H. Beladi, M.R. Barnett and P.D. Hodgson, "Recrystallization in AISI 304 austenitic stainless steel during and after hot deformation," *Materials Science and Engineering A,* vol. 485, pp. 664-672, 2008.

[114] N.A. Abbaspour and K. Farmenesh, "Recrystallization in AISI 304 austenitic stainless steel using hot torsion test," *Engineering and Technology 14, Global Journal of Science,* pp. 125-131, 2013.

[115] A. Dehghan-Manshadi, H. Beladi, M. Barnett and P. Hodgson, "Recrystallization in 304 austenitic stainless steel," *Materials Science Forum* , Vols. 467-470, pp. 1163-1168, 2004.

[116] A. Belyakov, H. Miura and T. Sakai, "Dynamic recrystallization under warm deformation of a 304 type austenitic stainless steel," *Materials Science and Engineering A,* vol. 255, pp. 139-147, 1998.

[117] W. Roberts and B. Ahlblom, "A nucleation criterion for dynamic recrystallization during hot working," *Acta Metallurgica,* vol. 26, pp. 801-813, 1978.

[118] E. Brunger, X. Wang and G. Gottsein, "Nucleation mechanisms of dynamic recrystallization in austenic steel alloy 800H," *Scripta Materialia,* vol. 38, 1998.

[119] L. Chen, X.C. Ma, X. Liu and L.M. Wang, "Processing map for hot working characteristics of wrought 2205 duplex stainless steel," *Materials Design,* vol. 32, pp. 1292-1297, 2011.

[120] W. Rizhi and T.C. Lei, "Substructural evolution of ferrite in a low carbon steel during hot derformation in (F + A) two-phase range," *Scripta Metallurgica et Materialia,* vol. 28, pp. 629-632, 1993.

[121] L. Briottet, J.J. Jonas and F. Montheillet, "A mechanical interpretation of the activation energy of high gtemperature deformation in two phase materials," *Acta Materialia,* vol. 44, pp. 1665-1672, 1996.

[122] F. Gao, Y. Xu, B. Song and K. Xia, "Substructural changes during hot deformation of an Fe-26Cr ferritic stainless steel," *Metallurgical and Materials Transactions,* vol. 31A, pp. 21-27, 2000.

[123] G. Glover and C.M. Sellars, "Recovery and recrystallization during high temperature deformation of α-iron," *Metallurgical Transactions,* vol. 4A, pp. 765-775, 1973.

[124] T. Maki, S. Okaguch and I. Tamura, "Dynamic recrystallization in ferritic stainless steel," in *Proceedings of the International conference on strength of metals and alloys (ICSMA 6)* , 1982.

[125] A. Najafi-zadeh, J.J. Jonas and S. Yue, "Grain refinement by dynamic recrystallization during the simulated warm-rolling of interstitial free steels," *Metallurgical Transactions A,* vol. 23, pp. 2607-2617, 1992.

[126] R. Pandi and S. Yue, "Dynamic transformation of austenite to ferrite in low carbon steel," *Iron and Steel Institute of Japan International,* vol. 34, pp. 270-279, 1994.

[127] A. Dehghan-Manshadi, M.R. Barnett and P.D. Hodgson, “Microstructural evolution during hot deformation of duplex stainless steel,” *Materials Science and Technology 23,* pp. 1478-1484, 2007.

[128] E. Simielli, S. Yue and J. Jonas, “Recrystallization of microalloyed steel deformed in the intercritical region,” *Metallurgical Transactions,* vol. 23A, pp. 597-608, 1992.

[129] J. Sas, T. Kvackaj, O. Milkovic and M. Zenko, “Influence of plastic deformation in γ and (γ + α) area on structure and mechanical properties of High-strength Low-alloy (HSLA) steels,” *Materials 9,* vol. 971, pp. 1-8, 2016.

[130] P.J. Hurley and P.D. Hodgson, “Formation of ultra-fine ferrite in hot rolled strip; potential mechanisms for grain refinement,” *Materials Science Engineering,* vol. 302A, pp. 206-214, 2001.

[131] R.Z. Wang and T.C. Lei, “Dynamic recrystallization of ferrite in a low carbon steel during hot rolling in the the (F + A) two-phase range,” *Scripta Metallurgica et Materialia,* vol. 28, pp. 1193-1196, 1994.

[132] H. Beladi, K. G.L., A. Shokouhi and P.D. Hodgson, “The evolution of ultrafine ferrite formation through dynamic strain-induced transformation,” *Materials Science Engineering,* vol. 371A, pp. 343-352, 2004.

[133] R. Song, D. Ponge, D. Rabbe and R. Kaspar, “Microstructure and crystallographic texture of an ultrafine grained C-Mn steel and their evolution during warm deformation and annealing,” *Acta Materialia,* vol. 53, pp. 845-858, 2005.

[134] D.B. Santos, R.K. Bruzszek and P.C.M.Rodrigues and E.V. Pereloma, “Formation of ultra-fine ferrite microstructure in warm rolled and annealed C-Mn steel,” *Materials Science Engineering A,* vol. 346 , pp. 189-195, 2003.

[135] N. Tsugi, Y. Matsubara and Y. Saito, “Dynamic recrystallization of ferrite in interstitial free steel,” *Scripta Materialia,* vol. 37, pp. 477-484, 1997.

[136] S. Gourdet and F. Montheillet, “A model of continuous dynamic recrystallization,” *Acta Materialia,* vol. 51, pp. 2685-2699, 2003.

[137] Y.C. Lin, M.S. Chen and J. Zhong, “Constitutive modelling for elevated temperature flow behaviour of 42CrMo steel,” *Computational Materials Sciences 42,* pp. 470-477, 2008.

[138] H. Dong and X. Sun, “Deformation induced ferrite transformation in low crabon steels,” *Current Opinion in Solid State and Materials Science,* vol. 9, pp. 269-276, 2005.

[139] Y. Matsumura and H. Yada, “Evolution of ultrafine-grained ferrite in hot deformation,” *Journal of Iron and Steel Institute of Japan,* vol. 27, pp. 492-498, 1987.

[140] H. Beladi, G.L. Kelly and P.D. Hodgson, “Ultrafine grained structure formation in steels using dynamic strain induced transformation processing,” *International Materials Review,* vol. 52, pp. 14-28, 2007.

[141] J.K. Choi, D.H. Seo, J.S. Lee, K.K. Um and W.Y. Choo, “Formation of ultrafine ferrite by strain-induced dynamic transformation in plain low carbon steel,” *Iron and Steel Institute of Japan International,* vol. 43, pp. 746-754, 2003.

[142] H. Yada, Y. Matsumura and T. Senuma, “Massive type transformation induced by hot deformation in low carbon steels,” in *Proceedings of the International Conference on Martensic Transformation,* Sendai, Japan, 1986.

[143] T. Sakai and J.J. Jonas, “Dynamic recrystallization: Mechanical and microstructural consideration,” *Acta Metallurgica,* vol. 32, pp. 189-209, 1984.

[144] E.P. Busso, “A continuum theory for dynamic recrystallization with microstructure-related length scales,” *International Journal of Plasticity,* vol. 14, pp. 319-353, 1998.

[145] E.I. Poliak and J.J. Jonas, “Initiation of dynamic recrystallization in constant strain rate hot deformation,” *ISIJ International 43,* pp. 684-691, 2003.

[146] N. Ryan and H. McQueen, “Dynamic softening mechanisms in 304 austenitic stainless steel,” *Canada Metallurgical Quarterly,* vol. 29, pp. 147-162, 1990.

[147] N.D. Ryan and H.J. McQueen, “Flow stress, dynamic restoration, strain hardening and ductility in hot working of 316 steel,” *Journal of Materials Processing Technology,* vol. 8, pp. 177-199, 1990.

[148] S.B. Davenport, N.J. Silk, C.N. Sparks and C.M. Sellars, “Development of constitutive equations for modelling of hot rolling,” *Materials Science and Technology 16,* vol. 16, pp. 539-546, 2000.

[149] Q. Guo-Zheng, “Characterization for dynamic recrystallization kinetics based on stress-strain curves,” InTech, 2013.

[150] A. Najafizadeh and J. Jonas, “Predicting the critical stress for initiation of dynamic recrystallization,” *ISIJ International 46,* vol. 46, pp. 1679-1684, 2006.

[151] H. Mecking and U. Kocks, “Kinetics of flow and strain hardening,” *Acta Metallurgica,* vol. 29, pp. 1865-1875, 1981.

[152] H. Mecking and U. Kocks, “Kinetics of flow hardening,” *Acta Metallurgica,* vol. 29, pp. 1865-1875, 1981.

[153] H. Yada, Y. Matsumura and T. Senuma, “A new thermomechanical heat treatment for grain refining in low carbon steels,” in *Proceedings 1st Conference on Physical Metallurgy of Thermomechanical Processing of steels and other metals (Thermec-88),* Tokyo, 1988.

[154] X. Sun, H. Luo, H. Dong, Q. Liu and Y. Weng, “Microstructural evolution and kinetics for post-dynamic transformation in a plain low carbon steel,” *Iron and Steel Institute of Japan International,* vol. 48, pp. 994-1000, 2008.

[155] J.J. Jonas, C. Ghosh, X. Quelennec and V.W. Baabe, “Predicting the occurrence of dynamic transformation and rolling mill loads drops by hot torsion and compression testing,” *International Journal of Metallurgical Engineering 2,* vol. 2, pp. 1-9, 2013.

[156] C. Zener and J.H. Hollomon, “Effect of strain-rate upon the plastic flow of steel,” *Journal of Applied Physics,* vol. 15, pp. 22-27, 1944.

[157] D.N. Zou, K. Wu, Y. Han, W.. Zhang, B. Cheng and G.J. Qiao, “Deformation characteristic and prediction of flow stress for as-cast 21Cr economical duplex stainless steel under hot compression,” *Materials and Design 51,* vol. 51, pp. 975-982, 2013.

[158] Y. Han, D. Zou, Z. Chen, G. Fan and W. Zhang, “Investigation on hot deformation behaviour of 00Cr23Ni4N duplex stainless steel under medium-high strain rates,” *Materials Characterization 62,* vol. 62, pp. 198-203, 2011.

[159] J.T. Liu, H.B. Chang, R.H. Wu, T.Y. Hsu and X.Y. Ruan, “Investigation on hot deformation behaviour of AISI T1 high-steel,” *Materials Characterization,* vol. 45, pp. 175-186, 2000.

[160] I. Alvarez-Armas and S. Degallaix-Moreuil, Duplex stainless steels, New Jersey: John Wiley and Sons, Inc., 2009, p. 448.

[161] Y.L. Fang, Z.Y. Liu and G.D. Wang, “Crack properties of lean duplex stainless steel 2101 in hot forming processes,” *Journal of Iron and Steel Research International,* vol. 18, pp. 58-62, 2011.

[162] A. Momeni and K. Dehghani, “Hot working behavior of 2205 austenite-ferrite duplex stainless steel characterized by constitutive equations and processing maps,” *Materials Science and Engineering A,* vol. 528, pp. 1448-1454, 2011.

[163] Y.V.R.K. Prasad and T. Seshacharyulu, “Processing maps for hot working of titanium alloys,” *Materials Science and Engineering,* vol. 243A, pp. 832-88, 1998.

[164] S.V.S. Narayana Murty, M.S. Sarma and B. Nageswara Rao, “On the evaluation of efficiency paramater in processing maps,” *Metallurgical Materials Transactions,* vol. 28A, pp. 1581-1582, 1997.

[165] Y.V.R.K. Prasad, K. Rao and S. Sasidhara, Hot working guide: A compendium of processing maps, Ohio: ASM International, 2015, p. 636.

[166] S.V.S. Narayana Murty, B. Nageswara Rao and B. Kashyap, “Development and validation of a processing map for AFNOR 7020 aluminium alloy,” *Materials Science Technology,* vol. 20, pp. 772-782, 2004.

[167] A. Airod, R. Petrov, R. Colaz and Y. Houbaert, “Comparison of axissymmetric compression to flat rolling of 5083 and 6082 aluminum alloys,” *Materials Forum,* vol. 28, pp. 293-298, 2004.

[168] L.M. Rothleutnev, “Iinfluence of reheat temperature and holding time on interaction of V, Al, and N, in air-cooled forging steels,” Advanced Steel Processing and Products Research Center, 2012.

[169] Dynamic Systems Inc, Gleeble® systems application note: Axisymmetric uniaxial compression testing using ISO-TTM anvils on Gleeble Systems, New York, 2003.

[170] J.L. McCall and J.H. Steele Jr, “Practical applications of quantitative metallography: A symposium,” Philadelphia, 1982.

[171] G.K. Tirumalasetty, M.A. van Huis, C. Kwakernaak, J. Sietsma, W.G. Sloof and H.W. Zandbergen, “Deformation-induced austenite grain rotation and transformation in TRIP-assisted steel,” *Acta Materialia,* vol. 60, pp. 1311-1321, 2012.

[172] A. Ramazani, A. Schwedt, A. Aretz, U. Prahl and W. Bleck, “Characterization and modelling of failure iniation in DP steel,” *Computational Materials Science,* vol. 75, pp. 35-44, 2013.

[173] A. Ramazani, Z. Ebrahimi and U. Prahl, “Study the effect of martensite banding on the failure initiation in dual-phase steel,” *Computational Materials Science,* vol. 87, pp. 241-247, 2014.

[174] E. Erisir and O. Bilir, “Study of martensitic-ferritic dual phase steels produced by hot stamping,” in *IOP Conference Series: Materials Science and Engineering*, 2017.

[175] M. Mittal, T. Nanda, B.R. Kumar and V. Singh, “Effect of inter-critical annealing parameters on ferrite recrystallization and austenite formation in DP 590 steel,” *Materials and Manufactring Processes,* vol. 32, pp. 1231-1238, 2017.

[176] H.S. Zurob, C.R. Hutchinson, A. Beche, G.R. Purdy and Y.J.M. Brechet, “A transition from local equilibrium to paraequilibrium kinetics for ferrite growth in Fe-C-Mn: A possible role of interfdacial segregation,” *Acta Materialia,* vol. 56, pp. 2203-2211, 2008.

[177] C. Qiu, H.S. Zurob, D. Panahi, Y. Brechet, G.R. Purdy and C.R. Hutchinson, “Quantifying the solute drag effect on ferrite growth in Fe-C-X alloys using controlled decarburization experiments,” *Materials Science and Engineering,* vol. 44, pp. 3472-3483, 2013.

[178] J.W. Cahn, “The impurity-drag effect in grain boundary motion,” *Acta Materialia,* vol. 10, pp. 789-798, 1962.

[179] M. Hillert, “Solute drag in grain boundary migration and phase transformations,” *Acta Materialia,* vol. 52, pp. 5289-5293, 2004.

[180] M. Hillert and B. Sundman, “The treatment of solute drag on moving grain boundaries and phase interfaces in binary alloys,” *Acta Metallurgica,* vol. 24, pp. 731-743, 1976.

[181] H. Luo, J. Sietsm and S. Van Der Zwaag, “A novel observation of strain-induced ferrite to austenite retransformation after intercritical deformation of C-Mn steel,” *Metallurgical and Materials Transactions A,* vol. 35, pp. 2789-2797, 2004.

[182] J.H. Chung, J.K. Park, T.H. Kim, K.H. Kim and S.Y. Ok, “Study of deformation-induced phase transformation in plain low carbon steel at low strain rate,” *Materials Science and Engineering,* vol. 527, pp. 5072-5077, 2010.

[183] M.R. Barnett, G.L. Kelly and P.D. Hodgson, “Inferring dynamic recrystallization in ferrite using the kinetics of static recrystallization,” *Metallurgical and Materials Transactions,* vol. 33A, pp. 1893-1900, 2002.

[184] Y.N. Dastur and W.C. Leslie, “Mechanism of work hardening in Hadfield manganese steel,” *Metallurgical Transactions,* vol. 12A, 1981.

[185] L.E. Murr, Interfacial phenomena in metals and alloys, New Jersey: Addison-Wesley Publishing Company, 1975, p. 376.

[186] Y.D. Huang and L. Froyen, “Important factors to obtain homogeneous and ultrafine ferrite-pearlite microstructure in low carbon steel,” *Journal of Materials Processing Technology,* vol. 2002, pp. 216-226, 2002.

[187] C.M. Sellars and W.C. Tegart, “On the mechanism of hot deformation,” *Acta Metallurgica,* vol. 14, pp. 1136-1138, 1966.

[188] N. Haghdadi, D. Martin and P. Hodgson, “Physically-based constitutive modelling of hot deformation behaviour in a LDX 2101 duplex stainless steel,” *Materials and Design,* vol. 106, pp. 420-427, 2016.

[189] R.W. Evans and P.J. Scharning, “Axisymmetric compression test and hot working properties of alloys,” *Materials Science and Technology,* vol. 17, pp. 995-1004, 2001.

[190] Y.V.R.K. Prasad and K.P. Rao, “Processing maps and rate controlling mechanisms of hot deformation of electrolytic tough pitch copper in temperature range 300-950 ^{o}C,” *Materials Science and Engineering A,* vol. 39, pp. 141-150, 2005.

[191] F. Siciliano, “Mathematical modeling of hot strip rolling of Nb microalloyed steels,” PhD Thesis, 1999.

[192] T. Al-Samman and G. Gottsein, “Dynamic recrystallization during high temperature deformation of magnesium,” *Materials Science and Engineering,* vol. 490A, pp. 411-420, 2008.

[193] P.D. Southwick and R.W.K. Honeycombe, “Decomposition of ferrite to austenite in 26%Cr-5%Ni stainless steel,” *Materials Science,* vol. 14, pp. 253-261, 1980.

[194] A.T. Ciuffini, S. Barolla, C. Di Cecc, A. Gruttadauria, C. Mapelli and D. Mombelli, “Isothermal austenite-ferrite phase transformations and microstructural evolution during annealing in super duplex stainless steels,” *Metals,* vol. 7, pp. 1-16, 2017.

[195] K.N. Tu, J.W. Mayer and L.C. Feldman, Electronic thin film science for electrical engineers and materials scientists, New York: Macmillian Publishing Company, 1992, p. 445.

APPENDIX

APPENDIX 1: Experimental test parameters

A1: Table showing number of tests carried out together with the parameters used for each test

Test number	**Temperature (^{o}C)**	**Strain**	**Strain rate (s^{-1})**	**Deformation time (s)**
1	1050	0.6	0.1	6
2			1	0.6
3			5	0.12
4			10	0.06
5	1000	0.6	0.1	6
6			1	0.6
7			5	0.12
8			10	0.06
9	950	0.6	0.1	6
10			1	0.6
11			5	0.12
12			10	0.06
13	900	0.6	0.1	6
14			1	0.6
15			5	0.12
16			10	0.06
17	850	0.6	0.1	6
18			1	0.6
19			5	0.12
20			10	0.06
21	1050	0.8	0.1	8
22			1	0.8
23			5	0.16
24			10	0.08
25			15	0.05
26	1000	0.8	15	0.05
27	950			
28	900			
29	850			
30	850	0.015	10	0.0015
31		0.05		0.005
32		0.1		0.01
33		0.2		0.02
34		0.25		0.025
35		0.8		0.08

APPENDIX 2: Variation of peak stress, peak strain and austenite volume fraction with strain rate at 850 ^{o}C

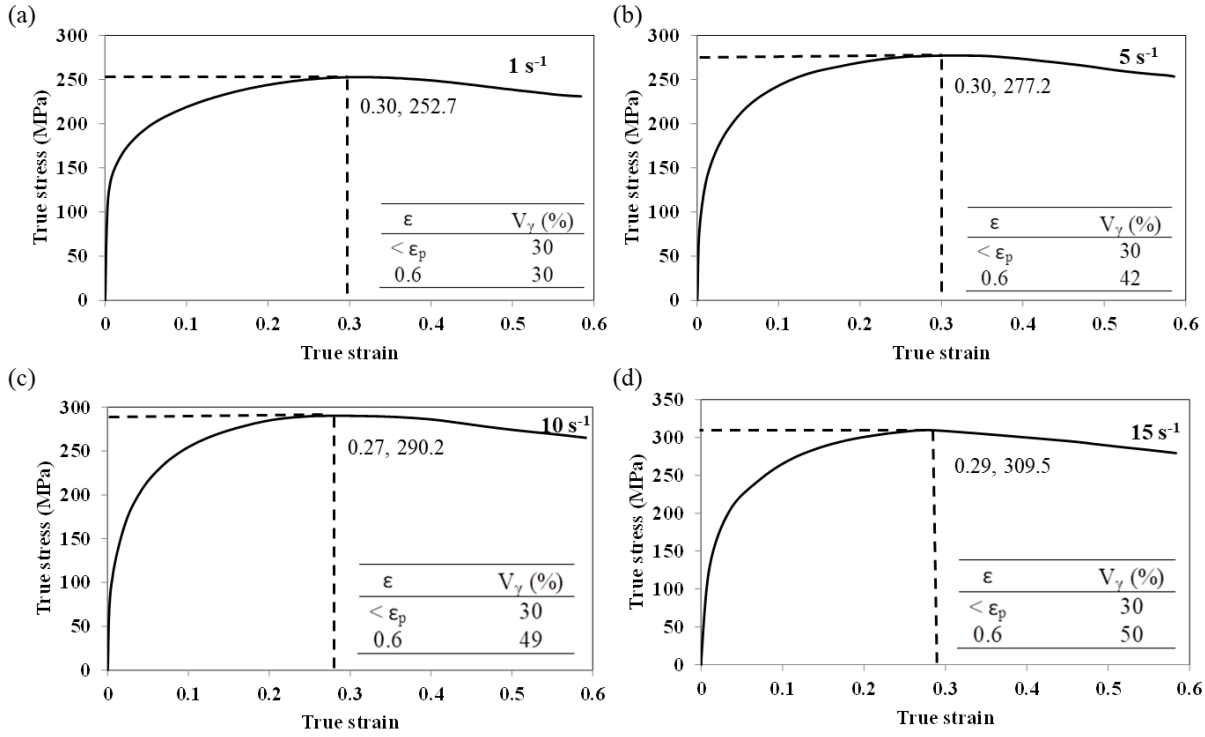

Figure A2.1: Variation of peak stress, peak strain and austenite volume fraction with strain rate. The stress and strain of the peak are estimated on each figure.

APPENDIX 3: Austenite volume fraction at 10 s^{-1}

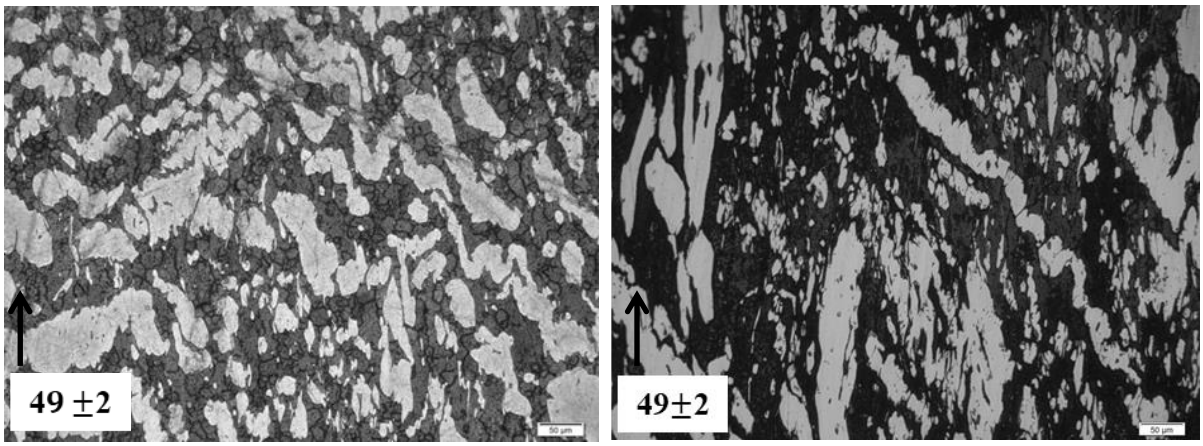

Figure A3.1: Austenite volume fraction at 850 ^{o}C, ε = 0.8, $\dot{\varepsilon}$ = 10 s^{-1}: (a) single pass (b) multipass.

APPENDIX 4: Derivation of the W.H. Relations

According to the modified representation of the Estrin-Mecking model:

$$\theta\sigma = A - B\sigma^2 \qquad 4.1$$

The constants in the above equation 4.1 can be determined from the plot of product of the work hardening rate and stress, θσ against the square of the stress, σ^2. From this plot A is the y-intercept and B the gradient from part of the plot, which is above the positive x-axis (Figure A4.1). Figure A3.1 is derived from the unmodified plot of θσ against σ^2 (Figure A4.2).

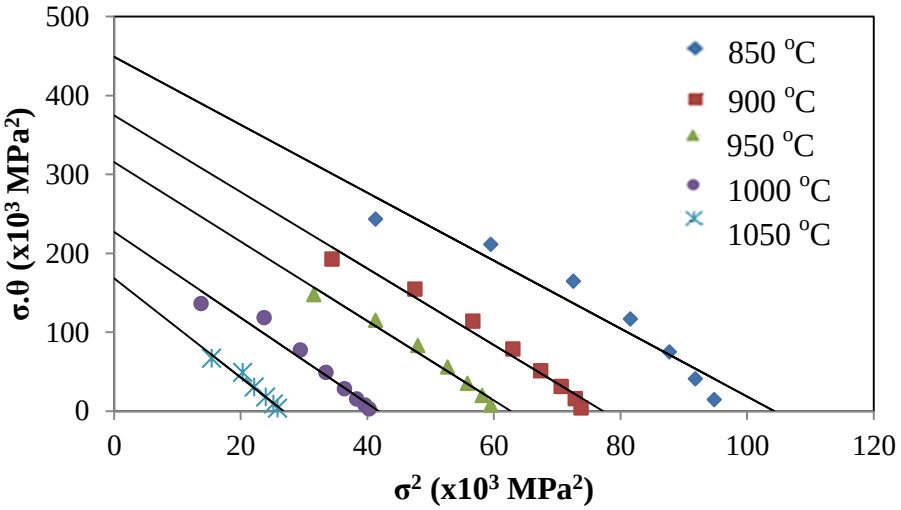

Figure A4.1: Plot of σθ against σ^2 to determine the values of A and B at a strain rate of 15 s^{-1}.

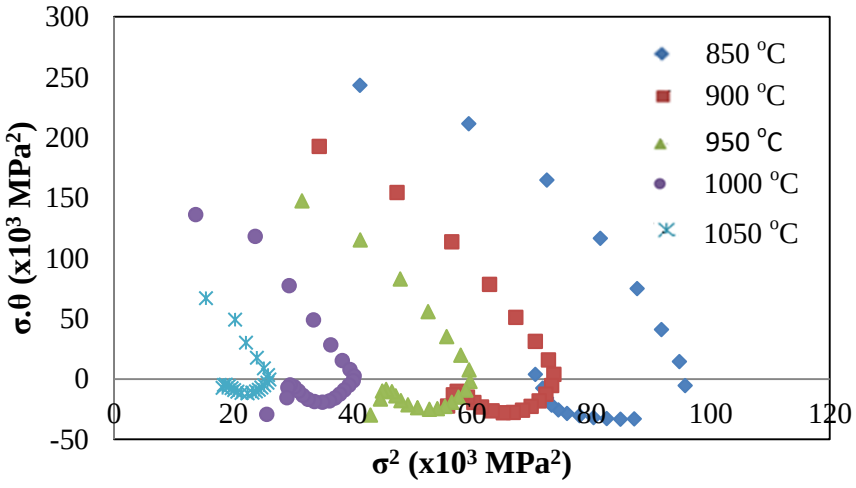

Figure A4.2: Unmodified plot of σθ against σ^2 to determine the values of A and B at a strain rate of 15 s^{-1}.

APPENDIX 5: Derivation of the constants in the Avrami softening model

According to the Avrami model the fractional softening due to DRX is given by:

$$X = 1 - \exp\left[-r\left(\frac{\varepsilon}{\varepsilon_p}\right)^q\right] \qquad 5.1$$

where the fractional softening X is determined as shown in equation [3-21] in literature review.

Equation 5.1 can be rewritten as follows:

$$1 - X = \exp\left[-r\left(\frac{\varepsilon}{\varepsilon_p}\right)^q\right]$$

$$\ln(1 - X) = -r\left(\frac{\varepsilon}{\varepsilon_p}\right)^q$$

$$-\ln(1 - X) = r\left(\frac{\varepsilon}{\varepsilon_p}\right)^q$$

$$\ln(-\ln(1 - X)) = \ln\ r + q\ \ln\left(\varepsilon - \varepsilon_p\right)$$

Thus the values of the constants r and q will be obtained from the plot of ln(-ln(1-X)) against ln(ε-ε_p) where ln r is the y-intercept and q is the gradient. From the graph ln r = 2.1875 and hence r = 8.9 and q = 1.7.

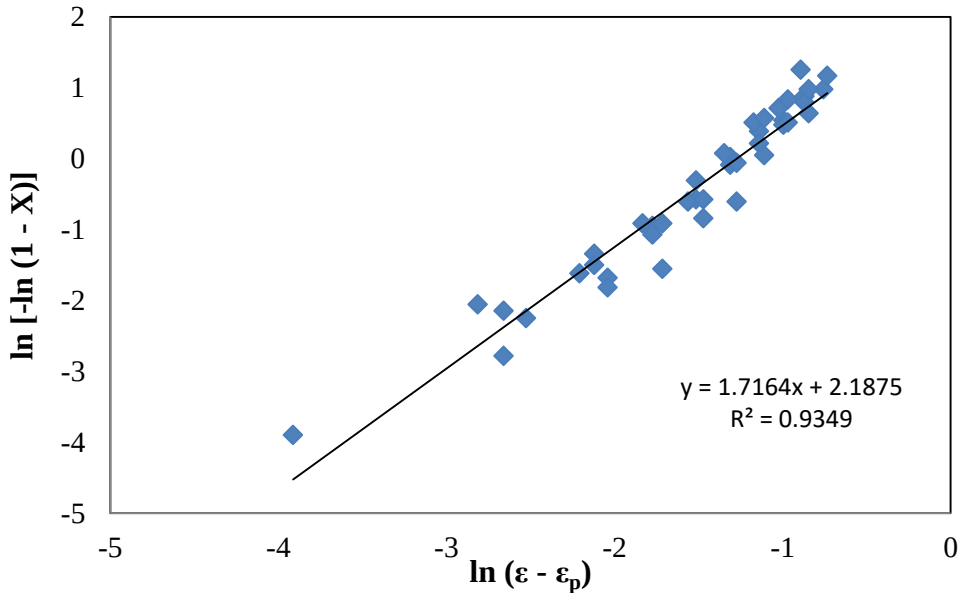

Figure A5.1: Plot of ln(-ln(1-X)) against ln(ε-ε_p) to determine the values of r and q at a strain of 0.8, a strain rate of 15 s-1 and a temperature range of 850 – 1050 ^oC.

APPENDIX 6: Rolling parameters used in the plant Steckel rolling mill

Rolling parameters in the plant Steckel mill							
Process input data	**F1**	**F2**	**F3**	**F4**	**F5**	**F6**	**F7**
Initial height (mm)	27.72	21.02	15.92	11.59	9.16	7.67	6.69
Final height (mm)	21.02	15.92	11.59	9.16	7.67	6.69	6.09
Temperature (^{o}C)	991	986	978	969	955	939	933
Roll separating force (kN)	18.8	19.0	22.9	17.6	15.4	12.7	9.5
Roll circumferential speed (m/s)	2.80	3.49	4.42	5.38	6.01	6.55	3.87
Process output data	**F1**	**F2**	**F3**	**F4**	**F5**	**F6**	**F7**
Strain per pass	0.28	0.28	0.32	0.24	0.18	0.14	0.09
Strain rate per pass (s^{-1})	11.09	16.69	25.77	30.54	32.06	33.21	19.78
Zener-Hollomon (s^{-1})	3.26 E+17	9.82 E+17	1.00 E+18	2.97 E+18	3.05 E+18	1.68 E+19	6.48 E+18
ln $Z_{in\text{-}plant}$	40.2	41.3	41.4	42.3	42.2	43.4	42.5
ln $Z_{corrected}$	45.0	45.6	46.3	46.8	47.3	48.0	47.7
MFS $(MPa)_{in\text{-}plant}$ Sims	159.23	171.82	198.97	200.29	221.61	224.69	225.24
MFS $(MPa)_{predicted}$	171.53	182.40	195.03	203.84	213.78	224.99	219.57

APPENDIX 7: Strain induced boundary migration leading to DT

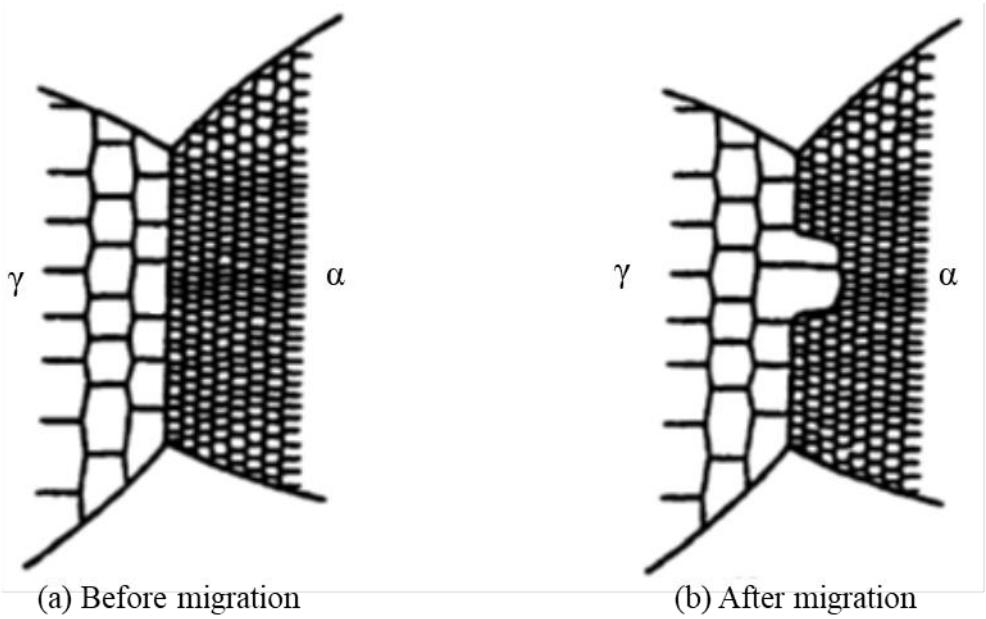

Figure A7.1: Model schematic on strain induced boundary migration leading to DT.

.

APPENDIX 8: Gibbs free energy model for deformation induced α – γ phase transformation during hot working

The effect of dislocations from plastic deformation is an internal energy E which is the resultant of the heat supplied to the system Q and the work done on the system W i.e.:

$$E = Q + W \quad (8.1)$$

The Gibbs free energy of a system is however, given by:

$$H = E + PV \quad (8.2)$$

$$\Delta G = \Delta H - T\Delta S = \Delta E + P\Delta V + V\,\Delta P - T\Delta S \quad (8.3)$$

In hot working processes, however, PΔV and VΔP are usually negligible and, therefore:

$$\Delta G \approx \Delta E - T\Delta S \quad (8.4)$$

In dislocations also, ΔS is usually very small which makes ΔG≈ ΔE. Thus, ΔG and ΔE, can be used interchangeably, as is the case in some parts of this work.

The free energy change of any phase transformation between austenite and ferrite without deformation is given by:

$$\Delta G = -V\Delta G_{chem} + A\sigma_{\gamma/\alpha} + V\Delta G_s \quad (8.5)$$

When the material is deformed, the equation can be rewritten as:

$$\Delta G = -V\Delta G_{chem} + A\sigma_{\gamma/\alpha} + V\Delta G_s - V\Delta G_D \quad (8.6)$$

where ΔG_{chem} is the chemical driving force, ΔG_D is the deformation stored energy, ΔG_s is the volume strain energy, and $\sigma_{\alpha/\gamma}$ is the α/γ boundary energy.

The equations above assume single phase deformation. In the case where deformation is carried out in the two phase region, it is imperative that both phases are deformed and the stored energy from deformation in each phase is a function of the SFE of the phase. According to the observations from the current study, a model is proposed. The model is based on the schematic in Figure A8.1.

The model considers a dual phase structure with austenitic phase in the vicinity of the ferritic phase but separated by a metastable intermediate structure (MIS). The MIS plays a crucial role of a buffer between the ferrite and austenite since the two phases by themselves have pronounced lattice mismatch and different atomic arrangements, hence will not match each other at the interface. The MIS overcomes these challenges and retains structural similarities to both phases and extends a few atomic orders in each phase. It is also noteworthy to recognise that phase transformations between the two phases do not involve the entire bulk phase, but a small part of the moving interface. The model presented is considered at three different strains:

1. Below the peak strain ($\varepsilon < \varepsilon_p$) - a higher dislocation density or stored energy is present in austenite compared to ferrite due to its low SFE and sluggish DRV. Due to strain being below the critical strain, no DRX is considered in austenite, hence the term for stored energy from deformation remains.
2. Above the peak strain ($\varepsilon_1 > \varepsilon_p$) – ferrite is still undergoing DRV and due to being in the vicinity of austenite, the deformation energy continues to increase. By this time the critical strain for DRX has been surpassed and hence DRX has already started in austenite, reducing the stored deformation energy in the phase. This leaves the ferrite phase with a higher deformation than the austenite phase and the progression of the MIS (interface) or austenite front into the ferrite to lower the system energy, takes place at the same time increasing the austenite fraction.
3. $\varepsilon_2 > \varepsilon_{1,}$ the situation is similar as in (2) except more DRX has taken place in austenite while the more deformed dislocation density is introduced in the ferrite. This results in a further progression of the austenite front into the high energy deformed ferritic structure in a SIBM-manner, resulting in more ferrite to austenite transformation.

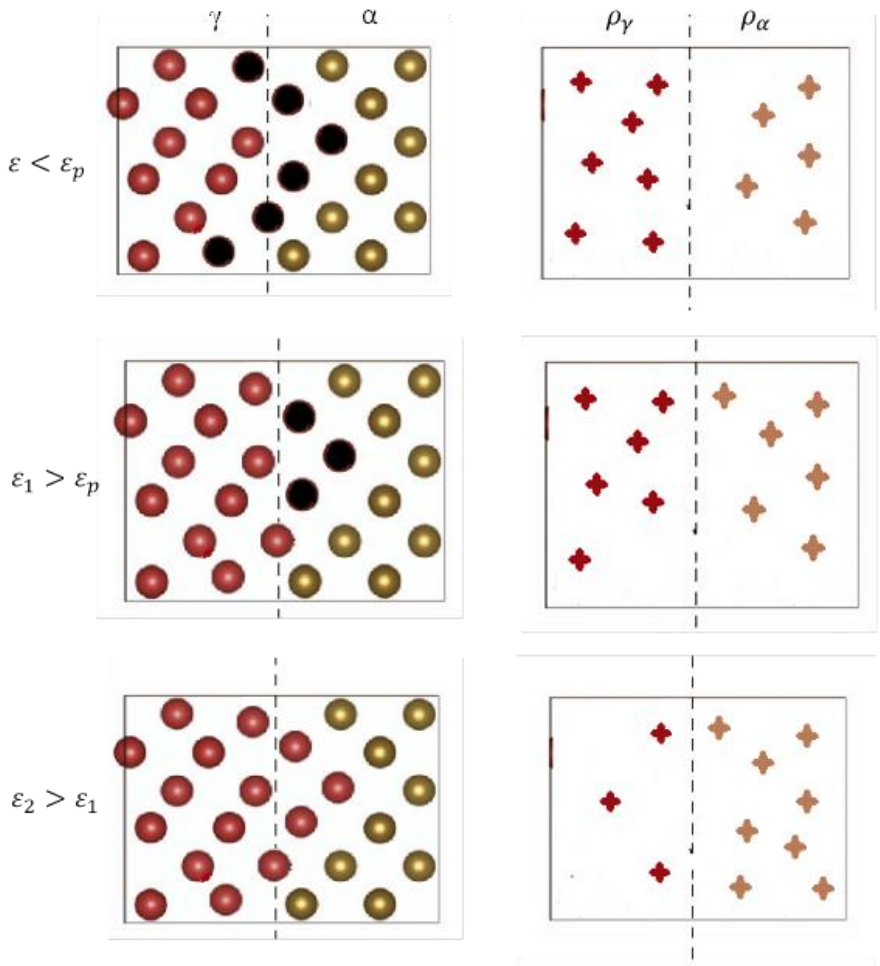

Figure A8.1: Model schematic on how ferrite to austenite phase transformation takes place during deformation.

The Gibbs free energy change for ferrite-to-austenite transformation can be calculated for the condition where the two phases are experiencing different stresses due to DRV in ferrite and DRX after the peak, i.e. σ_{DRV}^{α} and σ_{DRX}^{γ} respectively as:

$$\Delta G_m^{\alpha\to\gamma}(\Delta\sigma) = G_m^{\gamma}\left(\sigma_{DRX}^{\gamma}\right) - G_m^{\alpha}(\sigma_{DRV}^{\alpha}) \qquad 8.7$$

Rearranging equation 8.7:

$$\Delta G_m^{\alpha\to\gamma}(\Delta\sigma) = \Delta G_m^{\alpha\to\gamma}(\sigma) + \Delta G_m^{\alpha}(\Delta\sigma) \qquad 8.8$$

Where,

$$\Delta G_m^{\alpha\to\gamma}(\sigma) = G_m^{\gamma}\left(\sigma_{DRX}^{\gamma}\right) - G_m^{\alpha}\left(\sigma_{DRX}^{\gamma}\right) \qquad 8.9$$

And,

$$\Delta G_m^{\alpha}(\Delta\sigma) = G_m^{\alpha}\left(\sigma_{DRX}^{\gamma}\right) - G_m^{\alpha}(\sigma_{DRV}^{\alpha}) \qquad 8.10$$

The term $\Delta G_m^{\alpha\to\gamma}(\sigma)$ in Eq. 8.8 refers to the free energy change of ferrite-to-austenite transformation under constant stress (i.e. dislocation density in the two phases is the same and there is no Δσ: $\sigma_{DRX}^{\gamma} = \sigma_{DRV}^{\alpha}$).

According to a previous study [193] the precipitation of austenite in the stainless steel is equivalent to its decomposition in low alloy steels and by so-doing, the direction of the fcc↔bcc is immaterial [194]. Hence this value is thus approximated from that of γ-to-α transformation [182] and thus the first term in equation 8.9 can be assumed to be equal to the free energy change in the given transformation without any effect of stress, implying:

$$\Delta G_m^{\alpha\to\gamma}(\sigma) \approx \Delta G_m^{\alpha\to\gamma}(0) \qquad 8.11$$

Considering equation 8.8, the second term indicates the free energy change associated with the stress difference in the ferrite phase, given by equation 8.10. Using the same approach used by Tu *et al*. [195], the term in equation 8.10 can be calculated from the chemical potential change in stressed ferrite through applying the same approach used for a pure element in creep.

The chemical potential difference as a result of stress difference can thus be expressed as [182]:

$$\Delta\mu(\Delta\sigma) = \frac{d\left(F(\Delta\sigma)\right)}{dN^*} = \Delta\sigma^{\alpha}\Omega^* \qquad 8.12$$

$$\text{where, } \Delta\sigma^{\alpha} = \sigma_{DRX}^{\gamma} - \sigma_{DRV}^{\alpha} \qquad 8.13$$

The molar Gibbs free energy change due to the stress difference in the ferrite phase after neglecting the Helmholtz and Gibbs free energies can be found from [182]:

$$\Delta G_m^{\alpha}(\Delta\sigma) = \Delta\sigma^{\alpha}V_m^* \qquad 8.14$$

where, V_m^* is the molar volume of the hypothetical pure element of ferrite. Thus by combining equations 8.11 and 8.114, the Gibbs free energy change for the α-to-γ transformation, in a case where austenite and ferrite are experiencing different stresses

because ferrite has undergone recovery and austenite recrystallization, can thus be expressed as [182]:

$$\Delta G_m^{\alpha\rightarrow\gamma}(\sigma) = \Delta G_m^{\alpha\rightarrow\gamma}(0) + \Delta\sigma^{\alpha} V_m^{*} \qquad 8.15$$

From equation 8.15 it can be seen that the equilibrium can be shifted during hot deformation due to the Gibbs free energy change (second term) if two phases are experiencing different stresses because one is undergoing recrystallization and the other recovery, as in the postulated theory of Figure A8.1. This then becomes the driving force for DT of the ferrite to austenite through the migration of the austenite front into ferrite.

APPENDIX 9: Austenite volume fraction at high strain rate (30 s^{-1})

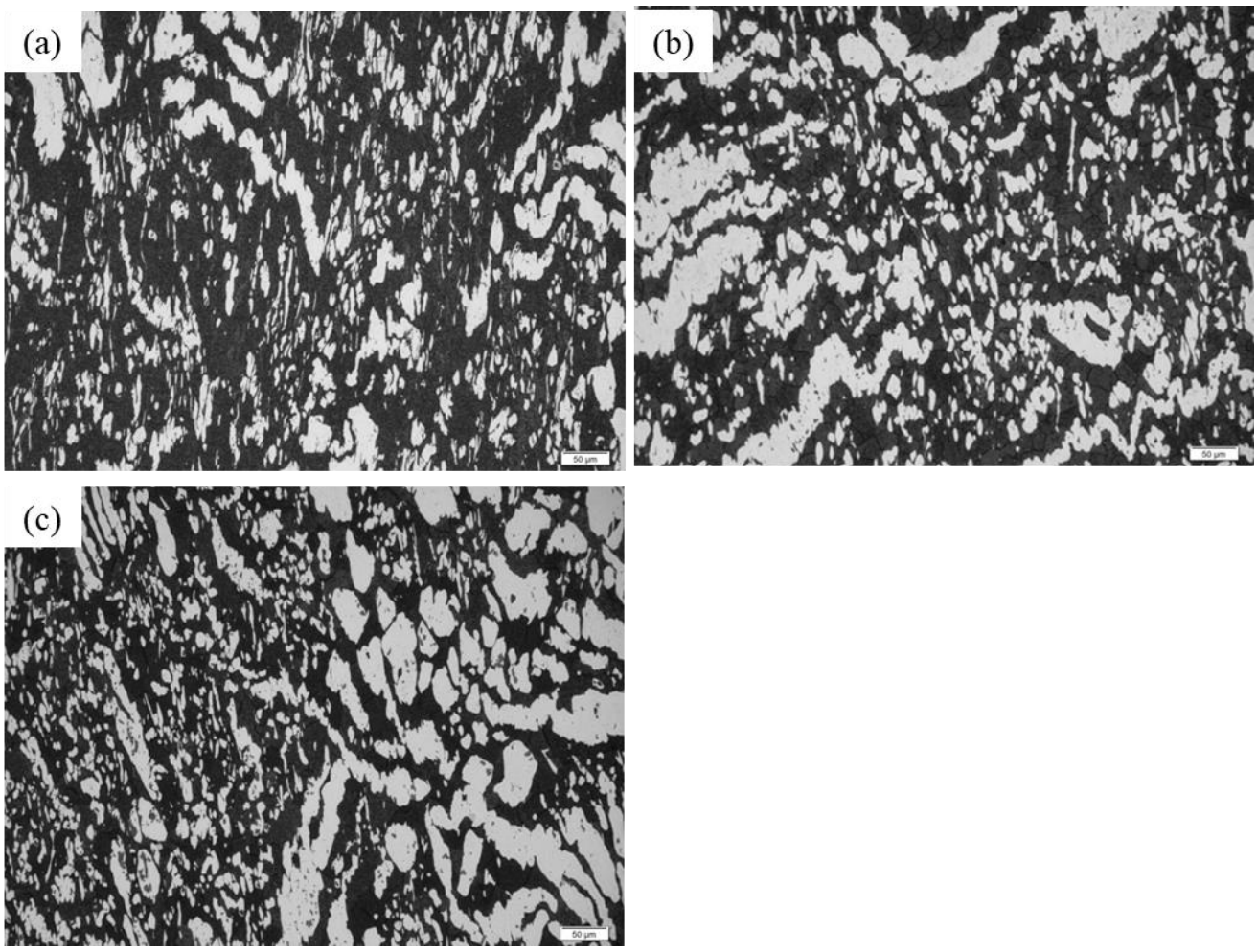

Figure A9: (a) Single-pass at 850 ^{o}C (b) Single-pass at 1050 ^{o}C (c) Multipass (3) with 20s interpass time at 1050 ^{o}C at 30 s^{-1} and strain of 0.8.%.